21GRD02 BIOSPHERE

21GRD02 BIOSPHERE

D3: Report on the identification and quantification of correlations between PCR and solar UV radiation on the ground, and their dependence on anthropogenic gas emissions based on the generation of a documented metrological method from field measurement campaigns conducted using the instrumentation from D1.

Organisation name of the lead participant for the deliverable: **PTB**

Due date of the deliverable: **September 2025** (M36)

Actual submission date of the deliverable: 30 September 2025

Confidentiality Status: PU - Public, fully open

Deliverable Cover Sheet

Funded by the European Union. Views and opinions expressed are however those of the author(s) only and do not necessarily reflect those of the European Union or EURAMET. Neither the European Union nor the granting authority can be held responsible for them.

European Partnership Co-funded by the European Union

METROLOGY PARTNERSHIP EURAMET

The project has received funding from the European Partnership on Metrology, co-financed from the European Union's Horizon Europe Research and Innovation Programme and by the Participating States.

Glossary

Acronym	Definition
ADV	ADVACAM, Prague, Czech Rep
AOD	Aerosol Optical Depth
BfS	Bundesamt für Strahlenschutz
BIRA-IASB	Royal Belgian Institute for Space Aeronomy
BRFAA	Biomedical Research Foundation of the Academy of Athens
CAS	Czech Academy of Sciences, Prague, Czech Republic
CCM	Charge Comparison Method
CFD	Constant Fraction Discrimination
CIE	Commission Internationale de l'Eclairage
CSR	Center for Space Radiation
DPP	Digital Pulse Processing
DU	Dobson Units
DWD	Deutscher Wetterdienst (German Meteorological Service)
EOLE	AErosol and Ozone Lidar systEm
EPT	Energetic Particle Telescope
FWHM	Full Width at Half Maximum
GAW	Global Atmosphere Watch
GCOS	Global Climate Observing System
GHI	Global Horizontal Irradiance
GHO	Gigahertz Optik, Türkenfeld bei München
GRUAN	GCOS Reference Upper Air Network
HCP	Heavy charged particle
HETP	High-energy transfer particle
HES	High Energy Section
IAF (aka UFA)	Institute of Atmospheric Physics of the CAS
INRSTES	Institute of Nuclear & Radiological Sciences & Technology, Energy & Safety
IOS	International Ozone Service Inc
IRM-KMI (aka RMI)	Institut Royal Météorologique de Belgique - Koninklijk Meteorologisch Instituut van België

LCP	Light charged particle
LETP	Low-energy transfer particle
LET	Linear-energy-transfer
LEO	Low Earth Orbit
LES	Low Energy Section
LIDAR	Light Detection and Ranging
MBE	Mean Bias Error
MOL-RAO	Meteorological Observatory Lindenberg – Richard-Aßmann-Observatory
NCSR-DEM	National Centre of Scientific Research – Demokritos
NIR	Near Infrared Radiation
NPI (aka UJF)	Nuclear Physics Institute of the CAS
NTUA	National Technical University of Athens
PCR	Primary cosmic rays
PMOD/WRC	Physikalisch-Meteorologisches Observatorium Davos / World Radiation Centre
PMT	Photo Multiplier Tube
PMT	Photomultiplier tube
PSD	Pulse Shape Discrimination
PTB	Physikalisch-Technische Bundesanstalt
SAA	Solar Azimuth Angle
SCR	Secondary Cosmic Rays
SEVAN	Space Environmental Viewing and Analysis Network
SiPM	Silicon photomultiplier
SMZ	Strahlungsmesszentrale: Radiation laboratory building of MOL-RAO
SPE	Solar Particle Event
STD	Standard Deviation
SZA	Solar Zenith Angle
TPX	Timepix
TOC	Total Ozone Column, in Dobson Units (DU)
UBA	Umweltbundesamt (German government environmental agency)

UFA (aka IAF)	Ústav fyziky atmosféry. AV ČR (Institute of Atmospheric Physics CAS)
UJF (aka NPI)	Ústav jaderné fyziky AV ČR (Nuclear Physics Institute CAS)
UV	Ultraviolet
UVE	UV Erythemal
UVI	UV Index
WCC-UV	World Calibration Center for UV
WMO	World Meteorological Organization (United Nations

TABLE OF CONTENTS

1 Summary

The BIOSPHERE project aims to develop metrological methodologies to establish the correlations between primary and secondary cosmic rays (PCR and SCR), solar UV radiation and ozone layer thickness, and to assess their mutual impact on the Earth's biosphere. The primary focus is on understanding how cosmic rays and solar UV radiation penetrate the atmosphere and influence atmospheric processes.
Variations in solar activity can lead to changes in atmospheric ionization (Kalakoski *et al.*, 2023; Winant *et al.*, 2023), which may affect ozone chemistry. Since ozone depletion increases the level of biologically active solar UV radiation reaching the surface, this project seeks to assess possible correlations between variations in cosmic ray (CR) flux, ozone abundance, Solar Particle Events (SPEs), and ground-level solar UV irradiance.

Deliverable 3 (D3) contributes to this effort by providing a comprehensive report on the identification and quantification of correlations between cosmic radiation and solar UV radiation on the ground, including their dependence on anthropogenic emissions such as ozone, NO_x, and aerosols. The deliverable is based on the generation of a documented and traceable metrological methodology, derived from multi-parameter observations collected during four coordinated field measurement campaigns conducted across four different sites in Europe. These campaigns were carried out at sites chosen to represent a range of altitudes, latitudes, and emission environments: the semi-urban NTUA/NCSR-DEM site in Athens (Greece), the urban SpacePole site in Brussels (Belgium), the mid-altitude Milešovka observatory in Czechia, and the well-equipped DWD Meteorological Observatory in Lindenberg in the North-East of Germany. Each site provided unique insights into the atmospheric, radiation, and pollution conditions relevant to the project's objectives.
In addition to characterising continuous background radiation fields, these campaigns also captured key solar particle events, whose impact on ground-level cosmic ray fluxes and UV irradiance is examined. The methodologies applied include traceable measurements of ground-level muon and neutron fluxes (SCR), solar UV irradiance, and Total Ozone Column (TOC), complemented by satellite observations and atmospheric profiling using advanced LIDAR, photometers, and gas analysers.

This report is structured as follows:
Section 2 provides an overview of the instruments used across all campaigns,
Section 3 describes the measurement campaigns in Athens, Brussels, Milešovka, and Lindenberg, along with site-specific data and initial observations.
Section 4 highlights major solar particle events recorded during the measurement period.
Section 5 presents the core analysis of correlations between CR, UV radiation, TOC and SPEs.
Section 6 presents a laboratory study of the penetration of V(UV) radiation though anthropogenic gas columns
Section 7 provides conclusions and outlines recommendations for future metrological efforts.
Section 8 lists all references and data sources used throughout the report.

2 On the Ground Instrumentation Overview

To achieve the project objectives, a complete set of ground-based instruments was deployed. These include detectors for SCR, produced by the interaction of PCR with the atmosphere, as well as instruments for monitoring solar UV radiation and deriving the UV Index. In addition, remote sensing systems were used to retrieve the TOC in Dobson Units (DU). These instrument groups are described in more detail in the following sections.

2.1 Secondary Cosmic Radiation instruments

2.1.1 Muon Monitor

To monitor the muon component of the SCR, PTB developed and deployed a portable, position-sensitive muon detector system DECOS2. This detector was used in the field campaigns in Athens, Brussels, Milešovka, and Lindenberg operating in coincidence mode and designed for mobility and flexible orientation.

Table 2.1: Overview of the mobile muon detector provided by the Physikalisch-Technische Bundesanstalt (PTB).

Complete Name	DEtector for COSmic ray, version 2 (DECOS2)
Manufacturer	Physikalisch-Technische Bundesanstalt (PTB)
Instrumental description:	See description below
Provided by:	PTB
Use in campaigns:	
NCSR-DEM Athens (GR)	Involved
Space Pole Brussels (BE)	Involved
UFA (IAF) Observatory Milešovka (CZ)	Involved
DWD Lindenberg (DE)	Involved

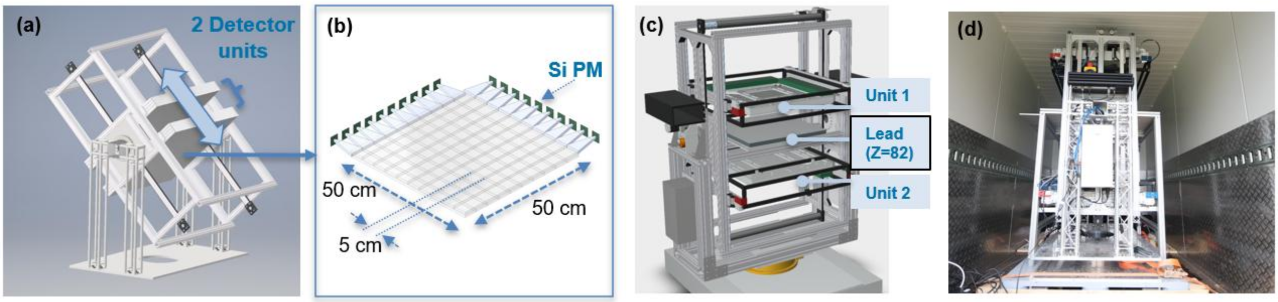

Figure 2.1: *Schematic drawings and a photo of PTB's position-sensitive muon detector DECOS2. (a) Schematic drawing of the aluminium frame with the two detector units. (b) Schematic drawing of one detector unit (top view). (c) Technical drawing of DECOS2 with 2.5 cm lead (Z=82) between the two detector units. (d) Photo of DECOS2 in a cooled trailer as it was used during all measurement campaigns.*

DECOS2 consists of two detection units mounted on a rotatable and tiltable aluminium frame, which allows the adjustment of both the angle (0°–90°) and azimuthal direction (0°–360°), as well as the distance between the units (ranging from 15 cm to 100 cm), enabling precise field-of-view (FOV) control, as illustrated in Figure 2.1.

Each detection unit contains 20 plastic scintillator paddles (Eljen EJ-200), coupled via light guides to silicon photomultipliers (SiPMs). The paddles are arranged in two orthogonal layers of 10 paddles each, with a pixel resolution of 5 × 5 cm². The perpendicular configuration of the layers enables the detector to identify the hit position of incoming muons and to resolve their trajectory in space, providing position-sensitive coincidence detection. Depending on the chosen separation between the layers, the angular field of view of the detector ranges from 0.79 sr/2π to 0.18 sr/2π.

During the measurements a 2.5 cm thick lead absorber (Z = 82) was inserted between the two units to discriminate between different particle energies and improve directionality. The entire setup was installed in a temperature-controlled trailer, which ensured stable operation in varying environmental conditions.

The detector was calibrated prior to deployment and regularly tested during the campaigns to ensure stability, energy resolution, and geometric alignment, providing reliable and traceable measurements of ground-level muon fluxes over extended periods.

Measurement Uncertainties

The characterization of the DECOS2 detector was performed in PTB's underground laboratory, located 430 m below ground, where the cosmic ray muon flux is reduced by more than three orders of magnitude. The exceptionally low background conditions (ambient dose equivalent rate $\dot{H}^*(10)$ = (1.5 ± 0.2) nSv/h) were achieved due to the low activity of the rock salt environment, low radon concentration (<10 Bq/m³), and the use of radiopure construction materials (<2 Bq/kg).

Calibration with reference ^60Co gamma fields showed that the relative uncertainty strongly depends on integration time, with values of ~4% for 1-minute acquisitions and <2% for 10-minute acquisitions, which corresponds to the standard operation mode. The measured reference ambient dose equivalent rates at three positions are summarized in Table 2.1.

Table 2.2: Reference ambient dose equivalent rate $\dot{H}^*(10)$ at different reference positions of DECOS2.

Reference distance / m	$\dot{H}^*(10)$ / (nSv/h)
0.7	993.5 ± 15.0
2	121.7 ± 1.9
3	54.1 ± 0.9

2.1.2 Neutron Monitors

The neutron component of the secondary cosmic rays was monitored using three complementary systems: a liquid scintillator neutron detector developed by the Nuclear Physics Institute of the Czech Academy of Sciences (UJF CAS) (Sommer, 2022), a customized high-resolution pixel particle telescope based on Timepix3 technology (Granja *et al.*, 2018), and Cosmic Neutron Detector which is a portable environmental neutron detector system developed by BFKH. These systems were deployed during the BIOSPHERE field campaigns to provide traceable, high-precision neutron measurements across a broad energy range, with capabilities for particle identification, spectral analysis, and directional tracking.

Table 2.3 : Overview of the neutron detector provided by the Nuclear Physics Institute CAS (UJF).

Complete Name	Neutron detector
Manufacturer	Nuclear Physics Institute CAS
Instrumental description:	See description below
Provided by:	NPI (ÚJF)
Use in campaigns:	
NCSR-DEM Athens (GR)	Involved
Space Pole Brussels (BE)	Involved
UFA (IAF) Observatory Milešovka (CZ)	Involved
DWD Lindenberg (DE)	Involved

The liquid scintillator neutron detector Figure 2.2 is based on two EJ-309B2.5 scintillators with a ^10B content of 2.5%, designed for Pulse Shape Discrimination (PSD) between neutrons and photons. The detector comprises a small 2×2″ unit (PMT 9214B, 51 mm) and a large 5×5″ unit (PMT 9390B, 130 mm), both coupled to photomultiplier tubes (PMTs) and read out by a CAEN DT5730S digitizer with DPP-PSD firmware. This portable system can measure neutrons from thermal energies up to several tens of MeV. The PSD algorithm enables reliable neutron/gamma separation by analyzing the shape of scintillation pulses. Processing steps include baseline subtraction, trigger timing via Constant Fraction Discrimination (CFD), calculation of deposited energy (whole pulse integration), and short/long gate charge comparison (CCM) for neutron identification. These features make the EJ-309 system particularly well suited for mobile field campaigns, combining robustness with high discrimination accuracy.

Figure 2.2: *Neutron detector – large scintillator 5x5" (left), small scintillator 2x2" (center), and box with all components (right).*

Measurement Uncertainties

The neutron detector was characterized in reference photon (^137Cs, ^60Co, X-rays 40–300 kVp) and neutron (AmBe, Cf, thermal neutrons) fields at the Czech Metrology Institute (CMI). The associated uncertainty estimations were considered throughout the characterization and calibration process, including energy calibration, neutron–photon discrimination, and efficiency determination in reference fields, with subsequent validation by Monte Carlo simulations. Energy calibration was performed using Compton edges from photon sources and proton recoils for fast neutrons, while the identification of thermal neutrons was based on the ^10B reaction. The energy resolution of the scintillators was derived from combined measurements with ^60Co and ^137Cs and Monte Carlo simulations, demonstrating a clear energy dependence of the FWHM. Detection efficiency was determined experimentally and by Monte Carlo simulations, with the corresponding values summarized in Table 2.2.

Table 2.4: Tabulated values of neutron relative detection efficiency and count rate per unit fluence of 2x2" and 5x5" scintillators derived by Monte Carlo calculations.

	Detection efficiency (%) 2x2" | 5x5"	K ((counts/s) / ($cm^{-2}s^{-1}$)) 2x2" | 5x5"
^{252}Cf - fast neutrons	25.3 | 37.5 (1)	5.1 | 47.5
AmBe - fast neutrons	27.9 | 44.8 (1)	5.7 | 56.7
Prism - thermal neutrons	78.5 | 84.8 (2)	20.4 | 143.0

1. For neutrons with E > 1 MeV via recoiled protons;
2. For thermal neutrons via neutron absorption on ^{10}B.

BFKH ^{3}He neutron detector

BFKH developed a portable environmental neutron detector system (see Figure 2.3) which was also used during the measurements campaign in Athens and Brussels.

Table 2.5: Overview of the neutron detector provided by the Budapest Főváros Kormányhivatala (BFKH).

Complete Name	Cosmic Neutron Detector
Manufacturer	MGP, Titon Bt.
Instrumental description:	See description below
Provided by:	BFKH
Use in campaigns:	
NCSR-DEM Athens (GR)	Involved
Space Pole Brussels (BE)	Involved
UFA (IAF) Observatory Milešovka (CZ)	Not involved
DWD Lindenberg (DE)	Not involved

In the measurement system, there is an MGP NIM201K neutron monitor, and an EnvColl environmental parameter measurement and data collector system developed and manufactured by Titon Bt, Hungary. In the NIM201K environmental neutron monitor two main parts are included. The detector assembly consists a He-3 proportional counter contained in a cylindrical tube placed inside a polyethylene sphere for slowing down fast neutron to the thermal energy range. The sphere has a floor/wall-mount support frame, and it is connected to a Local Processing and Display Unit (LPDU3/PPC). LPDU can process the counts and display the H*(10) dose-equivalent rate in the range 100 nSv/h – 300 mSv/h, for 0.025 – 16 MeV energy range. Parallel to this, the EnvColl with its software collects and processes the neutron counts (together with the atmospheric pressure, temperature and relative humidity of air), then calculates 60-s-averages (adjustable) and displays on a PC or notebook screen.

The whole system was involved under a weather-resistant covering and prepared for long-term permanent measuring.

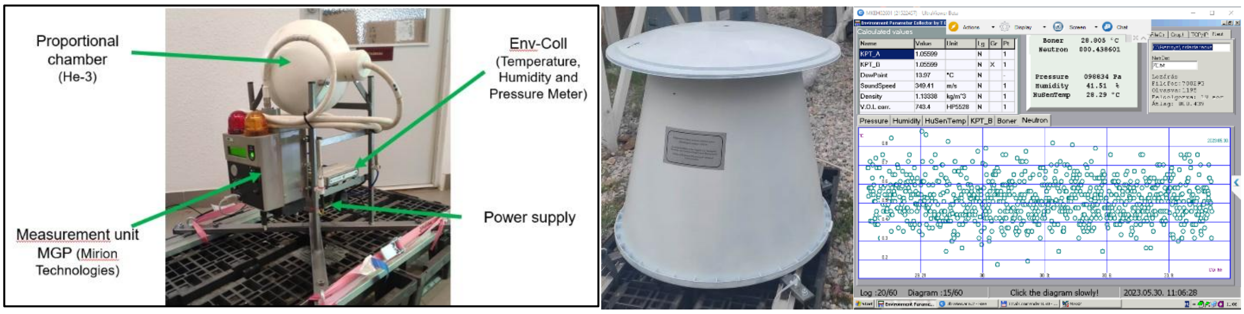

Figure 2.3: *Neutron detector – measurement setup (left), outdoor detector with cover (center), and measurement software (right).*

Measurement Uncertainties

The detector was calibrated with an Am-Be neutron source (calibrated by CMI) in the Metrology Laboratory of Paks Nuclear Power Plant, Hungary. Calibration method eliminates the source-related neutron scattering effects, so the calibration factor was calculated only for direct neutron counts per the cross-section of the detector. The standard uncertainty of the calibration factor is 5.5 %.

2.1.3 Charge particle trackers, stack pixel telescopes Timepix

In order to measure and characterize the mixed-radiation field in the atmosphere in detail and in wide-range, high-sensitivity pixel detectors Timepix were used [GRA18A, GRA14]. These detectors are operated with highly integrated readout electronics in the form of miniaturized radiation cameras [GRA18B]. The Timepix3 chip provides double signal per-pixel in the form of a spectral and time (or counting) channels. The deposited energy, position and direction of single particles are registered. The detectors can be operated as a particle tracker in wide field of view with particle-type discrimination. The stack telescope architecture (shown in Figure 2.4) provides enhanced spectrometry, higher particle tracking capabilities and extended particle type discrimination [GRA22]. This highly sensitive particle telescope has high-angular resolution (sub-degree) and high resolving power of particle discrimination (Granja *et al.*, 2018, 2022, 2025).

Table 2.6: Overview of the Timepix3 detector provided by ADVACAM.

Complete Name	MiniPIX detector with Timepix3 readout chip
Manufacturer	ADVACAM
Instrumental description:	See description below
Provided by:	ADVACAM
Use in campaigns:	
NCSR-DEM Athens (GR)	Involved
Space Pole Brussels (BE)	Not involved
UFA (IAF) Observatory Milešovka (CZ)	Involved
DWD Lindenberg (DE)	Involved

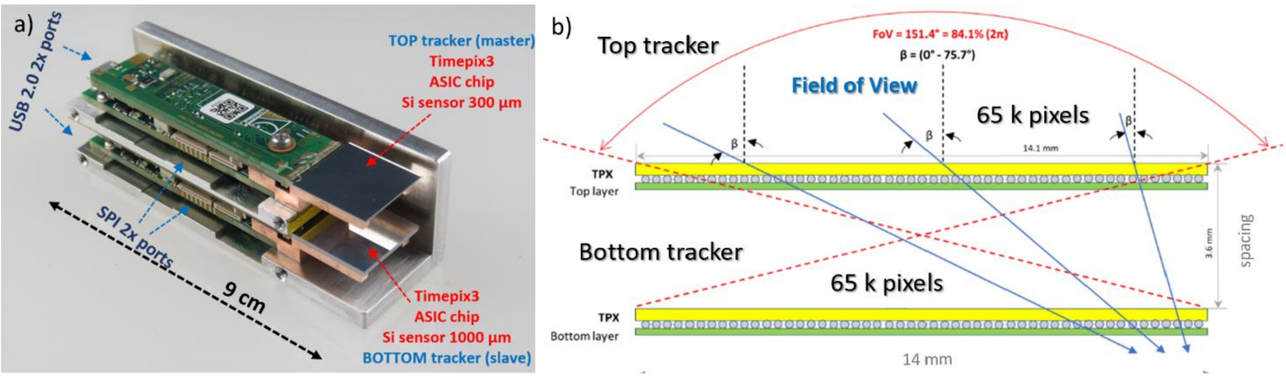

Figure 2.4: *The miniaturized particle telescope MiniPIX-Timepix3 2x Stack with Si sensors: (a) Integrated architecture and dimensions with 10 mm spacing gap between the top (TPX3 300 µm Si) and bottom (TPX3 1000 µm Si) trackers. The assembled device is readout by two USB 2.0 cables to standard PC. (b) The synchronized detection of charged particles (illustrated in blue) and the telescope field-of-view (in red) are indicated.*

To further enhance the spectral tracking response a second architecture was implemented (shown in Figure 2.5) with the bottom tracker equipped with a sensor of different material (CdTe) and thickness (2000 um). The spacing gap was also reduced to 4 mm thanks to the use of FLEXI connectors.

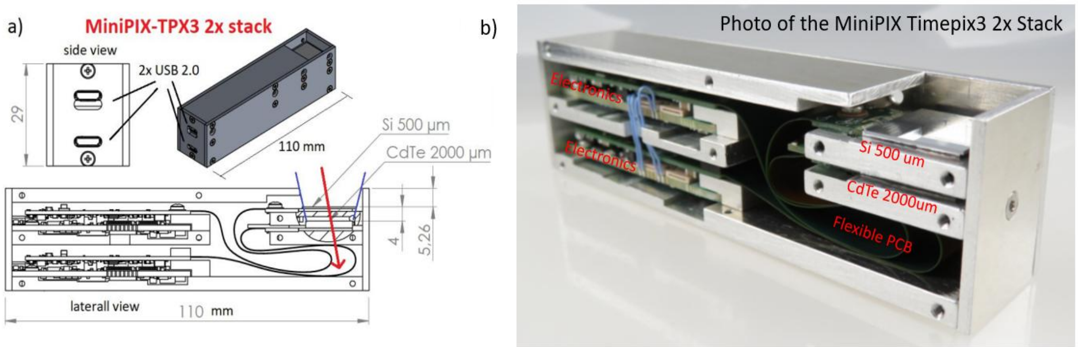

Figure 2.5: *The miniaturized particle telescope MiniPIX-Timepix3 2x Stack with Si and CdTe sensors: (a) Integrated architecture and dimensions with 4 mm spacing gap between the top (TPX3 500 µm Si) and bottom (TPX3 2000 µm CdTe) trackers. The synchronized detection of a charged particle (illustrated in red). b) Assembled device readout by two USB 2.0 cables to standard PC.*

Exploiting the sync operation of the two pixel detectors and high spectral tracking response, particles of similar energy loss can be further resolved such as electrons from muons [GRA25] - (which cannot be resolved in the single-chip detector [GRA18B]. This configuration is valuable for characterization of mixed-radiation fields such as the SCR field in Earth's atmosphere.

The detectors register essentially all ionizing particles namely charged particles both lights charged particles e.g. electrons, muons and heavy charge particles e.g. protons, ions [GRA18A]. In terms of the radiation energies, the particles are detected in wide energy range. Namely there is only a low-energy threshold at the level of few tens of keV for electrons, ≥ 100 keV for protons and ≥ 1 MeV/u for ions. Photons are also registered in a rather narrow energy range which depends on the material of the detector sensor. For silicon is namely in the X ray range, around 5 – 30 keV. For high-density sensor such as CdTe it is higher, up to ≈ 100 keV with decreasing detection efficiency. Neutrons are also detected [GRA23], both thermal and fast, with small ≤ 1% detection efficiency.

The deposited energy is precisely measured as well as the particle track length over the detector semiconductor sensor [GRA13]. Thus, the energy loss and resulting linear-energy-transfer (LET) is directly and accurately measured with particle-type resolving power [GRA21]. Single particles are registered individually with spectrometry (energy loss), position (on the detector pixel matrix), direction (relative to the detector sensor plane) and time resolution. These properties together with extensive physics calibrations in well-defined radiation fields and particle accelerator beams serve to provide the spectral (energy loss) and composition characterization of complex and mixed-radiation fields [GRA14, GRA24].

The detectors are operated by single USB cable to standard computer using the integrated SW tool PIXET [PIXET15] for control, online display and data acquisition. Raw data are stored and processed offline. The data is pre-processed with the data processing engine tool DPE/TraX [MAR24].

The physics data products produced by the Timepix stack telescopes provide extended information on the spectral and composition characterization of radiation fields and are summarized in the table below.

Table 2.7: Particle-type classification by the Timepix detector with silicon sensor [GRA24]. Particle-type classes are resolved in terms of radiations, energy ranges and direction.

Class	Track morphology	Interaction	Radiations	Energy (direction)
a	large tracks (≥4 px) broad, elongated	HETP	LE protons ions neutrons*	< 70 MeV (OD) > 1 MeV/u (OD) Thermal #, fast (OD)
b	large tracks (≥4 px) narrow, straight		ME protons	> 70 MeV (NPP) MIP
c	large tracks (≥3 px) narrow long	LETP	HE electrons	> 300 keV (OD)
			gamma rays**	> 30 keV – 100's keV (OD)
d	small tracks (≤4 px) round		X rays** LE electrons HE protons neutrons*	5-30 keV (OD) < 300 keV (OD), > 10 MeV (PP) MIP, > 150 MeV (PP) fast, IE
e	Narrow thin tracks		muons	Wide E (OD)

** = limited detection efficiency (DE) ≤ 1%*

*** = limited DE, limited energy range < 100 keV*

 # = in the thermal neutron converter mask (Lithium or Boron converter)

HETP = high-energy transfer particles, LETP = low-energy transfer particles, OD = omnidirectional

PP = perpendicular, NPP = non-perpendicular, px = pixel (55 µm), MIP = minimum ionizing particle

IE = intermediate energy, HE = high energy, LE = low energy, ME = mid energy

Measurement Uncertainties

The Timepix detectors provide ultimate sensitivity – photon counting – and particle-type resolving power combined with high spatial resolution, spectral, time and directional response of single particles. However, their small size (2 cm^2 area) limits the count rates especially in low intensity fields such as SCR in the atmosphere. In terms of particle flux measurement, the uncertainties are determined namely by count rate and poison statistics. In terms of spectrometry (energy loss) the energy resolution is around 5-10 % depending on the particle type and energy.

2.2 UV and TOC instruments

We use two categories of instruments: those deployed to measure surface UV radiation and those deployed to measure the Total Ozone Column (TOC).

Table 2.8: Overview of reference and secondary instruments used for UV Index and Total Ozone Column (TOC) monitoring.

Campaign	Athens (May-July 2023)	Brussels (Jan.-March 2024)	Milešovka (Aug-Nov 2024)	Lindenberg (Jan.-May 2025)
UV-Index Reference	BTS (DWD) and UV-Pyranometer (BIRA-IASB)	Bentham (BIRA-IASB)	BTS (DWD)	Bentham and BTS (DWD)
TOC Reference	BTS (GHO)	BTS (GHO)	BTS (GHO)	Brewers and Dobson (DWD)
UV-Index Secondary instruments	UV-Pyranometer, GUV (BIRA-IASB) Brewer (BRKAA)	GUV, UV-Pyranometer (BIRA-IASB)	GUV, UV-Pyranometer (BIRA-IASB)	GUV, UV-Pyranometer (BIRA-IASB)
TOC Secondary instrument	Brewer (BRKAA)	Brewer (IRM-KMI)	ø	BTS (GHO)

2.2.1 UV Instruments

The purpose of deploying UV instruments is to estimate the UV Index, a parameter used to assess the harmful effects of UV radiation on the biosphere, particularly on human skin. To obtain the UV-Index on the ground we deployed instruments to measure surface UV Global Horizontal Irradiance (UV-GHI) from the Sun, from which the UV Index can be derived. UV-GHI refers to the flux of downward solar UV photons received by a unit horizontal surface. When measured spectrally and integrated over all sky directions (to account for both diffuse sky radiation and direct sunlight), it is defined as global solar spectral irradiance expressed in $W \cdot m^{-2} \cdot nm^{-1}$. This quantity represents a dose rate that can be weighted by an action spectrum, which characterizes the sensitivity of a biological system, particularly relevant in the UV range.

The CIE (Commission Internationale de l'Éclairage: International Commission on Illumination) erythema action spectrum is a standardized weighting function that describes how human skin responds to ultraviolet (UV) radiation in terms of erythema (sunburn). The weighting of the total UV solar radiation by this action spectrum provides the biologically active solar UV radiation, often abbreviated UVE (UV Erythemal).

Finally, the UV Index (UVI) is defined as the UVE divided by 25 $mW \cdot m^{-2}$, providing a dimensionless indicator of biologically active solar UV radiation on an open scale.

The most accurate method is to deploy a reference UV spectrometer. Where facilities allow, UV monochromators (Bentham in this project) provide the highest precision. UV array spectrometers (BTS in this project) can also serve as reference instruments. More portable systems may be used if calibrated against a reference shortly before the campaign. These include multi-channel filter radiometers (GUV in this project) and UV pyranometers.

Filter radiometers provide a direct retrieval of the UV Index, whereas reference instruments (spectrometers, either array or monochromators) measure the full UV spectrum. The UV Index is then derived by integrating the spectrum with the CIE response function. All UV instruments use a cosine diffuser (a quartz dome over a horizontal receiving surface) to capture incoming UV radiation over all sky directions.

Figure 2.6 shows all types of UV instruments deployed in the four BIOSPHERE campaigns, arranged from the most precise, stable, bulky, expensive, and complex to operate (left) to the easiest to operate, autonomous, and portable (right).

Figure 2.6: *UV instruments deployed in the BIOSPHERE campaigns, ranging from precise but bulky and labour-intensive (left) to modern, portable, and easy-to-use (right).*

Brewer

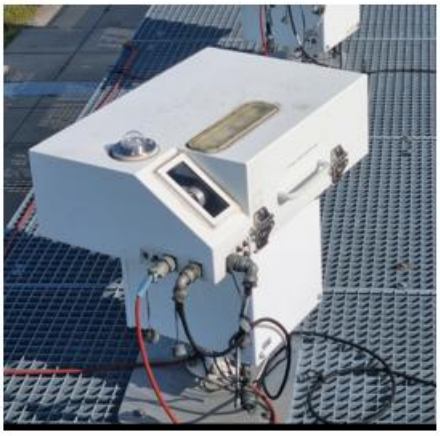

Table 2.9: Brewer spectrophotometer instruments and their use across the BIOSPHERE measurement campaigns.

Complete Name	Brewer MK II (or MK III° ozone spectrophotometer)
Manufacturer	SCI-TEC Instruments Inc. (Canada), then IOS (International Ozone Service, Canada), then OTT-Hydromet-Kipp+Zonen, the Netherlands
Instrumental description:	See description below
Provided by:	Different institutes/operators at each campaign
Use in campaigns:	
NCSR-DEM Athens (GR)	For verification only: Brewer #001 but at the 3-4 km away BRFAA (Biomedical Research Foundation of the Academy of Athens) site.
Space Pole Brussels (BE)	For verifications only. Provided by Royal Meteorological Institute (IRM-KMI) of Belgium; Brewer #016
UFA (IAF) Observatory Milešovka (CZ)	Not used
DWD Lindenberg (DE)	Measurements with DWD Brewers, especially #118 but data not analysed in the campaign.

The Brewer UV spectrometer was designed in the sixties and started to be operational in the seventies. Brewers have been manufactured by IOS (International Ozone Service Inc., Toronto, Canada) until the 2010ies then by Kipp & Zonen (Delft, The Netherlands).

The original idea was to have an automatic instrument that supplies the manual operated Dobson instruments for TOC measurements, but in addition to it, operates UV spectra monitoring in UVB to UVA. Therefore, the instrument was designed with a UV Spectrometer (monochromator), in the range 285 to 325 nm, with a high spectral resolution of 0.5 nm. The instrument has two optical entrances. The first entrance is a dome for the "global" modus, allowing UV spectral measurements of the GHI (Global Horizontal Irradiance). From these measurements, we can compute the UVB and UV-Index reaching the ground. The total standard uncertainty of the Brewer UV measurements is better than ± 5%. The second optical entrance is a periscope that is orientable in zenith in order to catch the direction of the sun. The periscope is put behind a quartz "direct sun window". The whole instrument is set on an azimuth tracker; therefore, the periscope is always pointing the sun direction when the instrument is in "direct sun" modus. The aim of the direct sun modus is the monitoring of Total Ozone Column (TOC). For this purpose, the Brewer has six slits positioned at the output of the monochromator in order to select six spectral channels in the UVB with very narrow triangular spectral response functions. These six spectral channels are at 303.2, 306.3, 310.1, 313.5, 316.8 and 320.14 nm. Some of these bands are positioned at high ozone absorption, some others at narrow ozone absorption. Some wavelengths are affected by SO_2 absorption and some not. A good combination of the measurements at these six wavelengths ("Brewer equation") allows the retrieval of Dobson Unit values of Total Ozone Column (TOC) and Total SO_2 Column. Well-calibrated Brewer instruments can reach uncertainties of ± 1%.

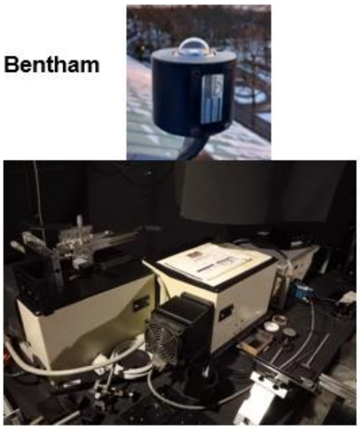

Table 2.10: Overview of the DTM300 double monochromator (Bentham Ltd, UK) and its role as a reference instrument in the BIOSPHERE campaigns

Complete Name	DTM300 double monochromator
Manufacturer	Bentham Ltd (UK)
Instrumental description:	See detailed description below
Provided by:	BIRA-IASB
Use in campaigns:	
NCSR-DEM Athens (GR)	Not involved
Space Pole Brussels (BE)	Reference instrument
UFA (IAF) Observatory Milešovka (CZ)	Not involved
DWD Lindenberg (DE)	Reference instrument

Accurate spectral measurements of global solar UV irradiance can be achieved using a less compact but highly sensitive and precise instrument: an absolute calibrated double monochromator. BIRA-IASB used a DTM300 from Bentham Ltd (UK) equipped with a fiber optics and Teflon diffuser as entrance optics and PMT as detector. Solar spectra are recorded through a scanning mechanism that ensures high straylight rejection. The cosine error of the entrance optics is characterized to correct for angular measurement errors. The UV index is obtained from the wavelength-integrated solar spectrum, weighted according to the CIE action spectrum. For daily profiling, measurements were taken every 15 minutes, with each spectral scan between 280 and 400 nm lasting approximately 4.5 minutes.

This instrument participated only in campaigns #2 and #4 (Brussels, Belgium, and Lindenberg, Germany). The radiometric characterization and absolute calibration were conducted by BIRA-IASB. Spectral lamps were used to calibrate the wavelength scale of the spectrometers and to determine its spectral resolution. The calibration results yielded a wavelength accuracy of ±0.05 nm and a spectral resolution (FWHM of the slit function) of 0.58 nm. The instrument response curve, which relates the electronic signal (PMT photocurrent) to irradiance, was established using NIST secondary standards of spectral irradiance (1000 W quartz-halogen lamps).

Measurement Uncertainties

The uncertainty budget for spectral solar UV irradiance measurements with a spectrometer is determined by evaluating the various contributions associated with the instrument, its characterization, and calibration. Key components include, for example, the residual non-linearity of the detection system, uncertainties from the calibration certificate of the standard lamp, the temperature dependence of the instrumentation and its effect on the detector response and wavelength scale, as well as measurement noise, etc.

For typical measurements, the standard uncertainty is approximately 1.7 % in the 310–400 nm range, increasing at shorter wavelengths, reaching about 3.5 % at 300 nm.

BTS (in global "GHI" modus)

Table 2.11: Overview of the BTS2048-UV spectrometer (Gigahertz-Optik GmbH, Germany) and its role as a reference instrument in the BIOSPHERE campaigns.

Complete Name	BTS2048-UV
Manufacturer	Gigahertz-Optik GmbH (GHO), Tuerkenfeld bei München, Germany
Instrumental description:	UV Array spectrometer, 2048 Channel 190-430 nm (functional: 290-400 nm) For UV measurements used in global (GHI) modus
Provided by:	DWD
Use in campaigns:	
NCSR-DEM Athens (GR)	Reference instrument until tech. problem
Space Pole Brussels (BE)	Not involved
UFA (IAF) Observatory Milešovka (CZ)	Reference instrument
DWD Lindenberg (DE)	Reference instrument

The Gigahertz-Optik BTS2048-UV-S is a modern UV array spectroradiometer developed as a compact and fast alternative to traditional scanning instruments. Introduced in 2018, it employs a back-thinned CCD array combined with an integral photodiode in the proprietary BiTec sensor, offering high spectral resolution (0.7 nm FWHM, 190–430 nm), wide dynamic range, and effective stray-light suppression. Its direct-sun cosine diffuser, filter wheel, and Peltier cooling ensure stability and radiometric accuracy, while the weather-proofed BTS2048-UV-S-WP variant adds temperature control, sealed optics, and heated domes for reliable outdoor use. Both instruments are factory-calibrated in ISO/IEC 17025-accredited labs, traceable to national standards.

The BTS2048 series has become widely adopted in Europe, particularly in Germany, where it complements Brewer and Dobson spectrometers in the national solar UV monitoring network coordinated by the Bundesamt für Strahlenschutz (BfS: German National Administration of protection against radiation) with until other DWD and UBA (Umwelt Bundesamt: German National Administration of Environment).

https://www.gigahertz-optik.com/de-de/produkt/bts2048-uv-s-wp/

Measurement Uncertainties

Long-term intercomparison studies show excellent stability and agreement with for instance Brewer reference instruments, with deviations typically within ±5 % in the 305–360 nm range relevant for UV-B and UV Index monitoring, though uncertainties increase at shorter UV wavelengths (< 300 nm).

GUV (GUV-511)

Table 2.12: Overview of the GUV-2511 multi-channel filter radiometer and its use as a secondary instrument in all BIOSPHERE campaigns.

Complete Name	GUV-2511, multi-channel filter radiometer
Manufacturer	BIOSPHERICAL Inc (USA)
Instrumental description:	See detailed description below
Provided by:	BIRA-IASB
Use in campaigns:	
NCSR-DEM Athens (GR)	Secondary instrument
Space Pole Brussels (BE)	Secondary instrument
UFA (IAF) Observatory Milešovka (CZ)	Secondary instrument
DWD Lindenberg (DE)	Secondary instrument

This instrument is designed to measure downwelling global spectral irradiance E_λ (in $\mu W \cdot cm^{-2} \cdot nm^{-1}$) at the following wavelengths: 305 nm, 313 nm, 320 nm, 340 nm, 380 nm, and 395 nm, as well as the Photosynthetically Active Radiation (PAR - 400-700 nm). Although the GUV-2511 does not directly measure erythemal irradiance, the UV Index (UVI) can be reconstructed using a parametric algorithm based on a linear combination of selected UV channels (305, 313, 320, and 340 nm). The methodology and associated coefficients are detailed in BIOSPHERICAL Application Note #AN-2015-0001-Rev1.

BIRA-IASB used the instrument serial number 25110406130 during the BIOSPHERE campaigns. It was factory recalibrated in April 2023, just before the campaigns (certificate “2511_130v3 4-3-2023_Cal_Cert.pdf” and ACCESS table “25110406130v3 4-3-2023.mdb”).

Measurement uncertainties

According to the BIOSPHERICAL study for a well-calibrated GUV-2511, the difference between the parametrized UV Index and the true UV Index is typically within ±0.2 UVI units.

UV-Pyranometer

Table 2.13: Model MS-212W pyranometer (EKO, Japan) used as a secondary instrument in all BIOSPHERE campaigns.

Complete Name	Model MS-212W, serial number S1104401
Manufacturer	EKO (Japan)
Instrumental description:	See detailed description below
Provided by:	BIRA-IASB
Use in campaigns:	
NCSR-DEM Athens (GR)	Secondary instrument
Space Pole Brussels (BE)	Secondary instrument
UFA (IAF) Observatory Milešovka (CZ)	Secondary instrument
DWD Lindenberg (DE)	Secondary instrument

This instrument is designed to measure the solar global irradiance integrated over the UVB range. Although its spectral response does not perfectly match the CIE erythema action spectrum, it can still be used to calculate the UV Index (UVI) in real time by applying an advanced correction methodology described by Hülsen and Gröbner, 2007. This approach involves an angular response correction to compensate for any deviation of the entrance optics from an ideal cosine response, and a spectral transfer function that virtually converts the instrument's spectral response to match the CIE erythema action spectrum.

The measurement equation used to obtain the UV index is based on the pyranometer's raw electrical signal (a net voltage $U - U_{offset}$), which is proportional to the UV energy received (typically over 280–400 nm), and also on instrument specific parameters determined from its radiometric characterization and calibration.

The general form of the equation is:

$$UVI = \frac{E_{CIE}}{25}$$

with

$$E_{CIE} = \left(U - U_{offset}\right) \cdot C \cdot f_n(SZA, TO_3) \cdot Coscor$$

where:

- E_{CIE} (in $mW \cdot m^{-2}$) is the wavelength-integrated erythemal global irradiance (obtained after CIE weighting),
- U is the measured raw signal
- U_{offset} is the dark signal
- C is the calibration factor (in mW.m^{-2}.CIE weighted.mV^{-1}),
- $f_n(SZA, TO_3)$ is the dimensionless conversion function, which translates from detector weighted solar irradiance to erythemal weighted irradiance
- $Coscor$ is a dimensionless correction function that compensates the cosine error of the instrument.

This pyranometer was radiometrically characterized and calibrated by the PMOD during the UVC-III campaign (summer 2022, Davos, Switzerland; see GAW Report No. 284). This calibration was used throughout the BIOSPHERE campaigns.

The calibration frequency of an instrument is a critical factor in assessing the uncertainty of solar UV measurements. Ideally, instruments should undergo annual calibration to ensure data quality, maintain traceability, and provide confidence in long-term stability. However, during the two-year duration of the BIOSPHERE campaigns, only the 2022 PMOD calibration was used to the instrument without intermediate recalibration.

The expanded uncertainty of UV index measurements can be estimated by applying the measurement uncertainty propagation approach to the pyranometer equation. The calculation performed by the WCC-UV laboratory of PMOD considers the uncertainties on individual parameters as the angular correction, the conversion function, the calibration coefficient, etc. The results is described in Section 6.1 of the GAW report No. 284. The standard uncertainty on UV index is 1.55 %, and 3.1 % at 2σ (expanded uncertainty: k = 2).

2.2.2 TOC Instruments

In this project, we expect ground-level UV Index variations induced by PCR effects (detected via SCR measurements) and by SPEs. Since these variations primarily result from SCR- and SPE-driven changes in stratospheric ozone, continuous monitoring of the ozone layer is required. We measure the Total Ozone Column (TOC) using ground-based UV remote sensing, which relies on differential ozone absorption in the UV-B range. Direct-sun spectrometers are employed, including single-channel instruments (Dobson), scanning monochromators (Brewer), and modern compact array spectrometers (BTS). During the campaigns, we deployed all three systems, spanning the historical Dobson reference, the Brewer standard, and the portable BTS (Figure 2.7).

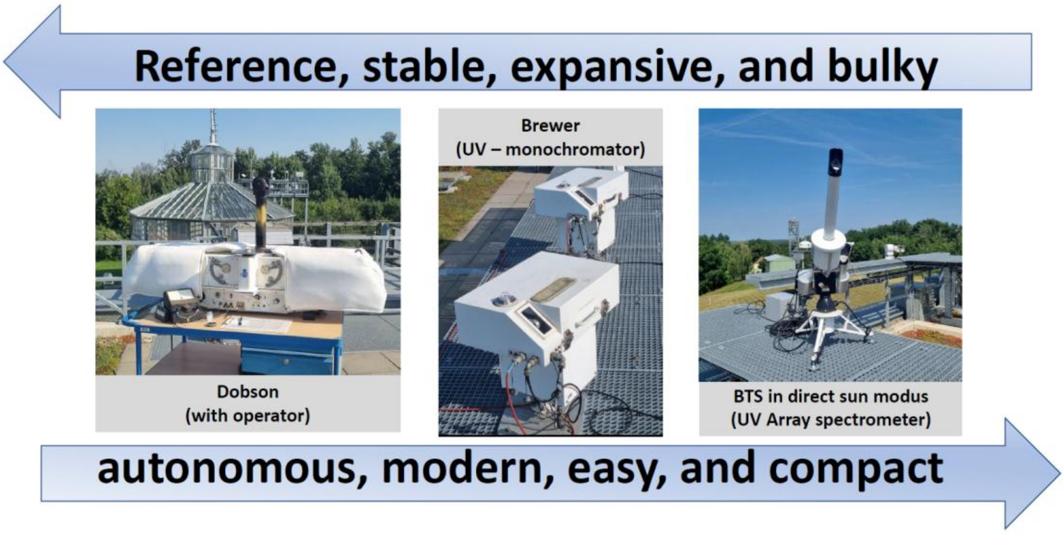

Figure 2.7: *Ozone instruments deployed in the BIOSPHERE campaigns, arranged from older and more labour-intensive (left) to modern and user-friendly (right).*

Dobson

Table 2.14: *Dobson UV spectrometer, originally manufactured by R & J Beck Ltd. (UK), used in the Lindenberg campaign (DWD) for reference TOC measurements.*

Complete Name	Dobson UV spectrometer
Manufacturer	Originally: R & J Beck Ltd. (London, UK), not manufactured anymore since late 1960s.
Instrumental description:	See below
Provided by:	DWD for the Lindenberg campaign
Use in campaigns:	
NCSR-DEM Athens (GR)	Not involved
Space Pole Brussels (BE)	Not involved
UFA (IAF) Observatory Milešovka (CZ)	Not involved
DWD Lindenberg (DE)	Dobson #071 of DWD for reference TOC with Brewer measurements together

The Dobson UV spectrometer, developed by Gordon M. B. Dobson in the 1920s, remains a cornerstone in global ozone monitoring. Initially produced by R & J Beck Ltd. in London, approximately 120 units were manufactured until the end of the 1960s. Early collaborations, notably with F. W. P. Götz in Arosa, Switzerland, led to the establishment of one of the longest continuous ozone measurement series (Dobson, 1931). The International Geophysical Year (1957–1958) revitalized global interest in ozone studies, with Walter Komhyr enhancing calibration techniques and operational procedures, establishing a calibration chain that underpins the Global Ozone Observing System (GOOS) of the World Meteorological Organization (WMO) (Steinbrecht et al., 2025; Komhyr, 1980). Despite the advent of automated instruments like the Brewer spectrometer in the 1980s, the Dobson spectrometer remains a reference standard, with approximately 50 operational stations worldwide, including about 15 under the NOAA's Global Monitoring Laboratory. In Europe, the Deutscher Wetterdienst (DWD: German Meteorological Service) hosts the Regional Dobson Calibration Centre Europe (RDCC-E) at Meteorological Observatory Hohenpeißenberg (Bavarian Alps), coordinating intercomparisons and providing technical support.

The Dobson technique utilizes the strong ultraviolet absorption of ozone below 315 nm. A quartz prism separates two UV wavelengths; one is strongly absorbed by ozone, and the other is less so. A rotating disc with slits alternately passes each wavelength, and a second prism recombines them before reaching a photomultiplier. To equalize the signals, a calibrated "grey wedge" is introduced into the less absorbed wavelength path. The wedge's position, when the photomultiplier's output nullifies, directly correlates to ozone absorption. The total ozone column is derived using this calibrated wedge position and known absorption coefficients (Komhyr, 1980). Combining measurements from both wavelength pairs reduces aerosol interference, enhancing accuracy (Steinbrecht et al., 2025).

WMO Dobson Network: https://public.wmo.int/en/programmes/global-atmosphere-watch/ozone

RDCC-E at DWD: https://www.dwd.de/EN/research/international_programme/gaw/rdcc/rdcc_node.html.

Measurement Uncertainties

TOC measurements with Dobson are from very high quality and are below 3 DU (basis 300 DU, therefore less than 1 %).

Brewer

Table 2.15: *Brewer MK II/III ozone spectrophotometer, provided by different institutes during the campaigns in Athens and Brussels.*

Complete Name	Brewer MK II (or MK III° ozone spectrophotometer
Manufacturer	SCI-TEC Instruments Inc. (Canada), then IOS (International Ozone Service, Canada), then OTT-Hydromet-Kipp+Zonen, the Netherlands.
Instrumental description:	See description below
Provided by:	Different institutes/operators at each campaign
Use in campaigns:	
NCSR-DEM Athens (GR)	Brewer #001 on the site of BFRAA (Biomedical Research Foundation of the Academy of Athens), 3-4 km from main campaign site as verification of BTS direct measurements.
Space Pole Brussels (BE)	Provided by Royal Meteorological Institute (IRM-KMI) of Belgium; Brewer #016 -> As control instrument for TOC; Reference after the campaign for Mother Day 2024 strong SPE case (12 May 2024).
UFA (IAF) Observatory Milešovka (CZ)	Not involved
DWD Lindenberg (DE)	Brewers #030, #078 and #118 of DWD as reference instrument or TOC

See description in section 2.2.1.

Measurement Uncertainties

TOC measurements with Brewer are from high quality and are below 5 DU (basis 300 DU, therefore less than 2 %). When recently calibrated for TOC measurements, the uncertainty is below 3 DU (1 %).

BTS in direct sun modus

Table 2.16: UV-BTS2048 spectrometer used in direct sun mode as reference instrument for TOC during all campaigns.

Complete Name	UV-BTS2048 in direct sun modus
Manufacturer	Gigahertz Optik GmbH, Türkenfeld bei München, Germany
Instrumental description:	See below
Provided by:	GHO (Gigahertz Optik)
Use in campaigns:	
NCSR-DEM Athens (GR)	As reference for TOC
Space Pole Brussels (BE)	As reference for TOC
UFA (IAF) Observatory Milešovka (CZ)	As reference for TOC
DWD Lindenberg (DE)	As control for TOC (reference: local Brewers and Dobson of DWD)

The UV-BTS2048-UV-S-WP instrument (UV array spectrometer, see description in 1.3.1) is deployed on solar trackers to record direct-sun UV spectra using its cosine diffuser and BiTec sensor, with hardware stray-light suppression ensuring high-quality measurements. From these spectra, the Total Ozone Column (TOC) can be retrieved using differential absorption in the UV-B range. In an intercomparison at Izaña, the UV-BTS-Solar showed excellent agreement with reference Brewer and Dobson instruments, with TOC deviations typically below 1.5 % and not exceeding 3 %. A detailed uncertainty analysis confirmed that high-end array spectroradiometers like the BTS2048 achieve expanded uncertainties of about ±1.5 % (k=2), which is comparable to Brewer reference instruments (Zuber et al., 2018).

Measurement Uncertainties

BTS has an expanded uncertainty (95% confidence) of about ±1.5%, comparable to high-end scanning instruments, while simpler array setups exhibit larger uncertainties (~4.7%). Therefore, TOC measurements with UV-BTS2048 in direct sun modus almost reach the standards of Brewer and Dobson TOC measurements and is below 5 DU uncertainty (less than 2 %).

2.2.3 Instruments for complementary information about atmospheric state and composition

Raman Lidar Athens

Complementary atmospheric information was obtained using Light Detection and Ranging (lidar) systems, which provide range-resolved vertical profiles of atmospheric parameters such as temperature, pressure, density, wind, water vapor, and aerosols.

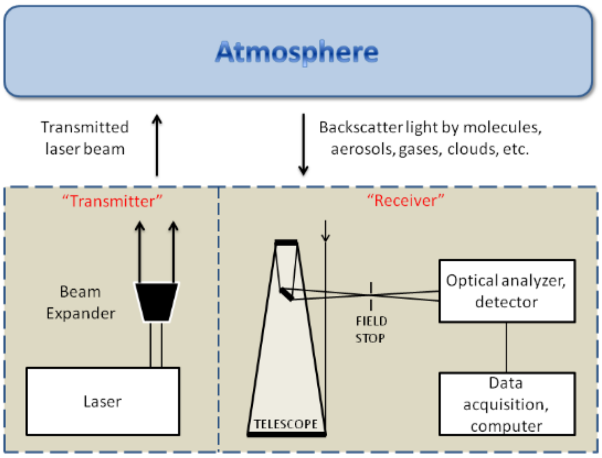

Figure 2.8: *General lidar system schematic configuration (Weitkamp, 2005).*

Table 2.17: *EOLE multi-wavelength aerosol-Raman lidar from NTUA, used during the Athens campaign for vertical profiling of aerosols and atmospheric properties.*

Complete Name	EOLE multi-wavelength aerosol-Raman lidar
Manufacturer	NTUA
Instrumental description:	Vertical profiling of aerosol optical properties, water vapour mixing ratio, atmospheric density, aerosol mass concentration (0.8-8-8-10 km)
Provided by:	NTUA
Use in campaigns:	
NCSR-DEM Athens (GR)	Involved
Space Pole Brussels (BE)	Not involved
UFA (IAF) Observatory Milešovka (CZ)	Not involved
DWD Lindenberg (DE)	Not involved

A lidar system typically consists of two main subsystems: a transmitter, where a pulsed laser beam is emitted and expanded, and a receiver, where the backscattered light from atmospheric molecules, aerosols, gases, or clouds is collected by a telescope and analyzed by optical detectors connected to a computer system for data acquisition (Figure 2.8).

For aerosol vertical profiling, pulsed lasers operating in the UV–NIR spectral range (355–2000 nm) are employed, while for atmospheric density retrieval, 532 nm elastic backscatter is commonly used. During daytime, aerosol vertical profiles are obtained through the Mie elastic backscattering technique (Klett, 1981, 1983), whereas at nighttime, Raman scattering of atmospheric N_2 is additionally exploited. This combined approach enables accurate retrievals of aerosol extinction (αaer) and backscatter (βaer) coefficients, as well as aerosol mass concentration.

At the National Technical University of Athens (NTUA), the EOLE lidar system is employed for vertical profiling of aerosols and atmospheric parameters (Figure 2.9). Its detection range extends from approximately 0.8 km up to 8–10 km altitude, achieving an accuracy of 10–15 % for αaer and 10–25 % for βaer, with a spatial resolution of 30 m near the ground (800 m altitude) and 100–250 m at higher altitudes (8–10 km) (Kokkalis et al., 2021). Moreover, elastic Rayleigh scattering from atmospheric molecules enables retrieval of density profiles in aerosol-free atmospheric layers, typically above 4–5 km (Weitkamp, 2005).

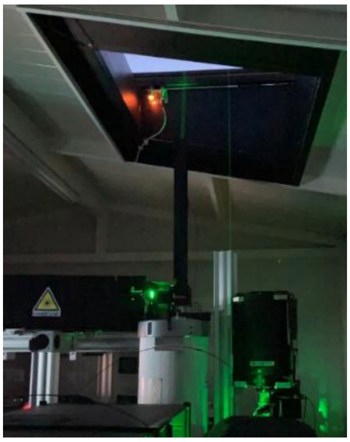

Figure 2.9: The EOLE lidar system

Radiosonde

The Vaisala RS41 radiosonde, produced by the Finnish company Vaisala Oyj, is a widely deployed upper-air measurement instrument designed for reliable and accurate profiling of atmospheric conditions. It measures temperature, humidity, pressure, and wind through an integrated system combining platinum-resistive temperature sensors, heated thin-film humidity sensors, and GPS-based height and wind determination—even under demanding weather conditions. The RS41 typically ascends to altitudes of up to approximately 35 km, being carried by the standard weather balloons as it is done in Lindenberg.

Radiosounding with Vaisala RS41 and weather balloons

Table 2.18: *Vaisala RS41 radiosonde provided by IRM-KMI and DWD, used in Brussels and Lindenberg campaigns for atmospheric profiling.*

Complete Name	Vaisala RS41 radiosonde
Manufacturer	Vaisala Oyj, Vantaa (Helsinki), Finland
Instrumental description:	See below
Provided by:	IRM-KMI or DWD
Use in campaigns:	
NCSR-DEM Athens (GR)	Not involved
Space Pole Brussels (BE)	From IRM-KMI
UFA (IAF) Observatory Milešovka (CZ)	Not involved
DWD Lindenberg (DE)	From DWD (GRUAN product): 4 soundings a day

As part of the GRUAN (GCOS Reference Upper-Air Network), RS41 soundings adhere to traceable calibration and uncertainty quantification protocols, enabling their use as high-quality climate reference data

At the Deutscher Wetterdienst (DWD: German Meteorological Service) observatory in Lindenberg, RS41 soundings are carried out four times daily at 04:45, 10:45, 16:45, and 22:45 UTC, providing valuable continuous vertical profiling.

- GRUAN: https://www.gruan.org/
- DWD Lindenberg Radiosonde Operations: https://www.dwd.de/EN/research/observing_atmosphere/lindenberg_column/in_situ/in_situ_node.html

Measurement Uncertainties

The RS41 demonstrates impressive stability and measurement precision: temperature uncertainties after ground preparation are below 0.11 °C (k = 2). For pressure, the GNSS-based method offers enhanced reproducibility and lower uncertainty compared to conventional barometric sensors, evidencing robust performance in operational use.

3 Field Measurement Campaigns and Data Analysis

3.1 Athens Campaign

The BIOSPHERE field campaign in Athens was coordinated by the National Technical University of Athens (NTUA) in collaboration with the Institute of Nuclear & Radiological Sciences & Technology, Energy & Safety (INRSTES) of the National Centre for Scientific Research “Demokritos” (NCSR-DEM). The primary measurement site was located at NCSR-DEM (37.995° N, 23.816° E, elevation 270 m a.s.l.), situated in the Athens Basin approximately 8 km north-east of the city centre and 4 km from the NTUA campus (37.960° N, 23.780° E, elevation 212 m) (cf. Figure 3.1, upper left). Both NCSR-DEM and NTUA sites provided unique LIDAR capabilities, enabling accurate measurements of key atmospheric profiling parameters (temperature, density, aerosol optical properties, and concentration), which are essential for establishing reliable correlations between secondary cosmic rays (SCR) and atmospheric parameters.

The Athens Campaign was conducted from 1 June to 31 August 2023. Instruments in Figure 3.1 were installed at NCSR-DEM at least 10–30 days prior to the campaign start, ensuring stable operation and calibration. The deployed instrumentation included:

- Portable mobile muon detector (PTB)
- Portable neutron detector (UJF CAS)
- ^{3}He detector for neutron spectra measurements and neutron counts (BFKH)
- UV spectroradiometer and BTS solar sun tracker (GGO)
- UVB pyranometer and GUV-511 multichannel filter radiometer (BIRA-IASB)
- Upgraded lidar system for atmospheric profiling (temperature, density, aerosol) developed by Raymetrics S.A

In addition, Aerosol Optical Depth (AOD) measurements at several wavelengths (UV to near-IR) were continuously performed at NTUA using a CIMEL sun photometer, as part of the AERONET network. Vertical profiles of aerosol optical properties (extinction and backscatter coefficients) and mass concentration were retrieved under cloud-free conditions using the NTUA elastic/Raman lidar system operating at 355, 532, and 1064 nm, covering altitudes from approximately 0.8 to 8–10 km.

Figure 3.1: *(upper left to down right) NCSR-DEM and NTUA sites, UV spectroradiometer, BTS solar sun tracker, UVB pyranometer, GUV-511 multi-filter radiometer, NTUA and Raymetrics lidars, neutron, muon detectors.*

3.1.1 Measurements of Secondary Cosmic Rays on the Ground

During the Athens campaign, simultaneous measurements of muon and neutron fluxes were conducted at the NCSR-DEM site using the PTB mobile muon monitor, the UJF CAS liquid scintillator neutron detector and BFKH ^{3}He detector for neutron spectra measurements and neutron counts. These ground-based SCR observations were complemented with co-located atmospheric pressure and temperature measurements, enabling environmental corrections and correlation analyses, as presented in Figure 3.2. Data gaps correspond to periods without measurements due to the power cutting caused by the heatwave that, coupled with strong winds, led to numerous wildfires, including some near Athens.

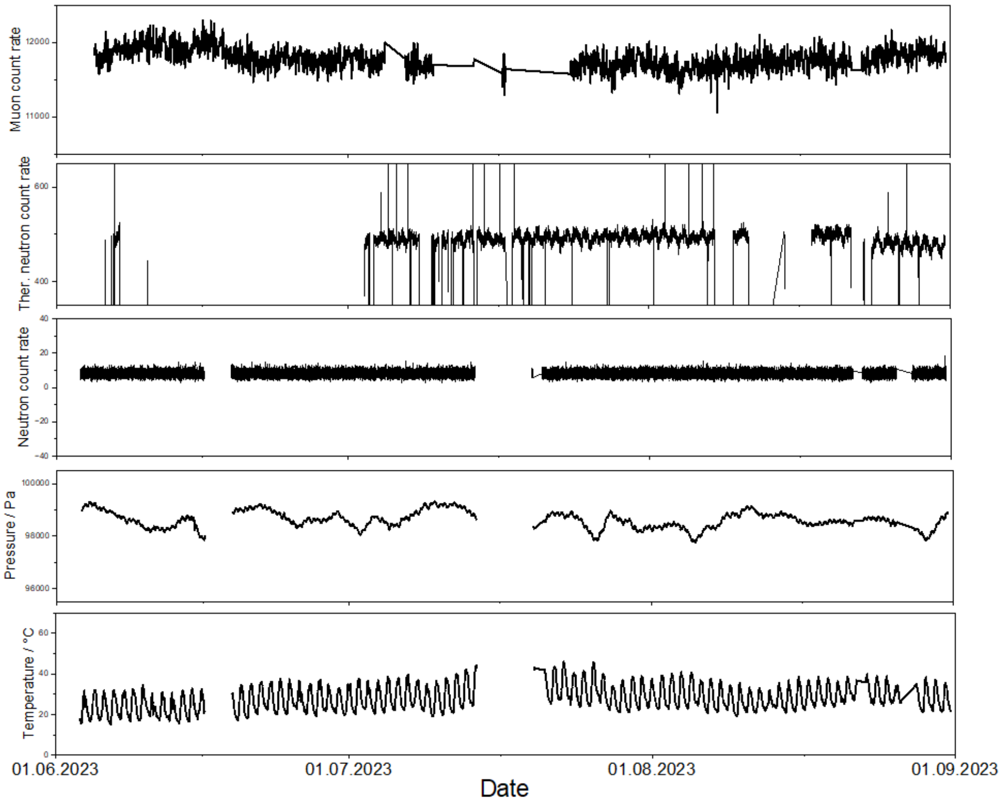

Figure 3.2: *Time series of measured secondary cosmic ray (SCR) and atmospheric parameters during the Athens campaign (June–August 2023). Panels show (from top to bottom): muon count rate (PTB muon monitor, DECOS2), thermal neutron count rate (UJF CAS liquid scintillator detector), total neutron count rate, atmospheric pressure, and air temperature.*

To identify the correlation between Secondary Cosmic Rays (SCRs) and atmospheric parameters (i.e., pressure, temperature, and humidity), we analysed both the time series and direct correlation plots.

Figure 3.3a shows muon count rates (black) overlaid with atmospheric pressure (Gray) for the period 24 July to 21 August 2023. A clear anti-correlation is evident: increases in pressure correspond to decreases in muon flux, consistent with the well-known barometric effect, where higher atmospheric column density attenuates the muon flux reaching the detector (Wissmann, Dangendorf and Schrewe, 2005; Alekseev *et al.*, 2022). Synoptic-scale pressure changes are closely followed by short-term variations in muon rate, but the long-term baseline remains constant, suggesting stable detector performance. Ground-level temperature variations do not play a role since muons are produced much higher in the atmosphere. It is the stratospheric temperature that matters, and this evolves only on seasonal or synoptic time scales, and our data which only available for 3-month campaign. That’s exactly what is observed in muon seasonal modulation studies (Wissmann, Dangendorf and Schrewe, 2005; Arunbabu *et al.*, 2017).

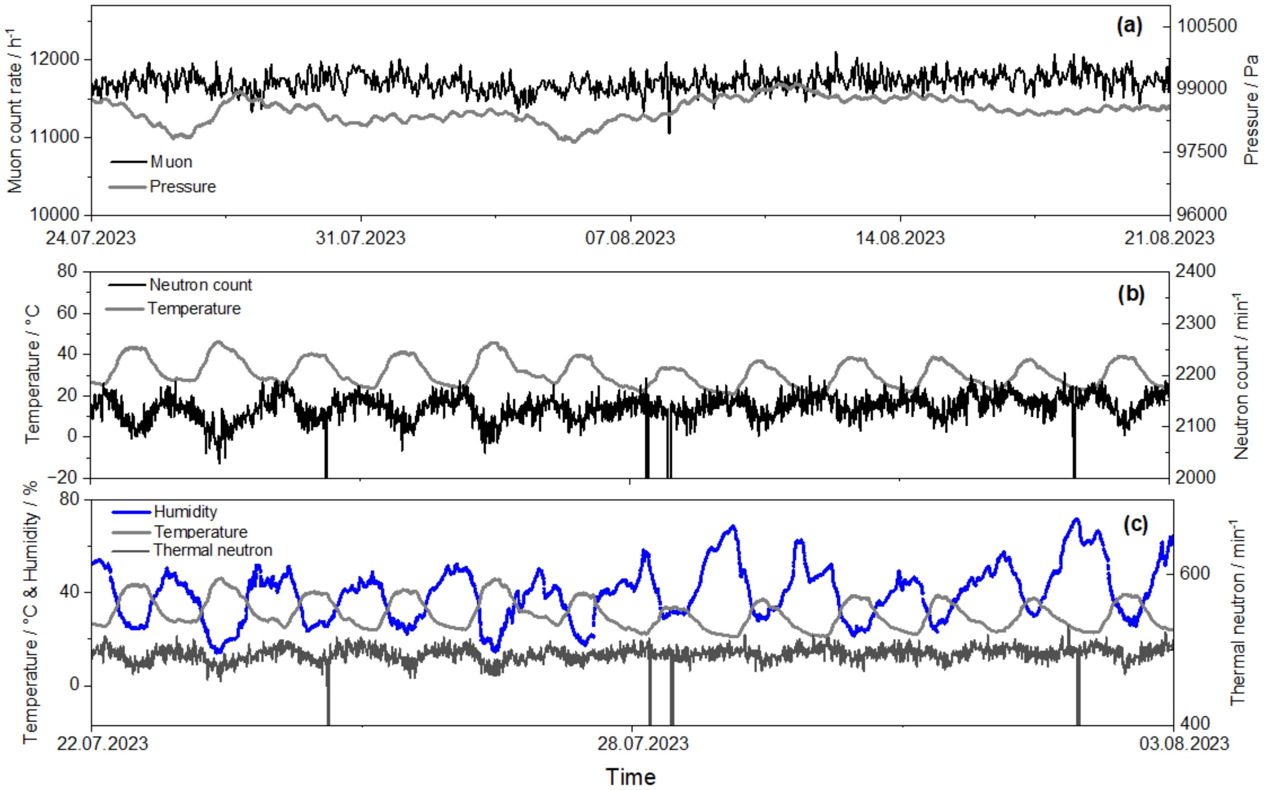

Figure 3.3: *(a) time series of muon count rate (black, left axis) measured with the PTB muon monitor and atmospheric pressure (Gray, right axis) during the Athens campaign (24 July – 21 August 2023). (b) Time series of neutron count rate (Black, right axis) measured with the UJF CAS liquid scintillator detector and ambient temperature (Gray, left axis) during the Athens campaign (22 July – 3 August 2023). (c) Thermal neutrons count rate (black, right axis) compared with ambient temperature (Blue) and relative humidity (Gray), 22 July – 3 August 2023.*

The corresponding scatter plots in Figure. 3.4a–b confirms these findings. Muon flux exhibits almost no correlation with ground temperature (r = 0.02), but a moderate negative correlation with pressure (r = –0.30). These results reinforce the dominance of the barometric effect and the negligible role of surface temperature.

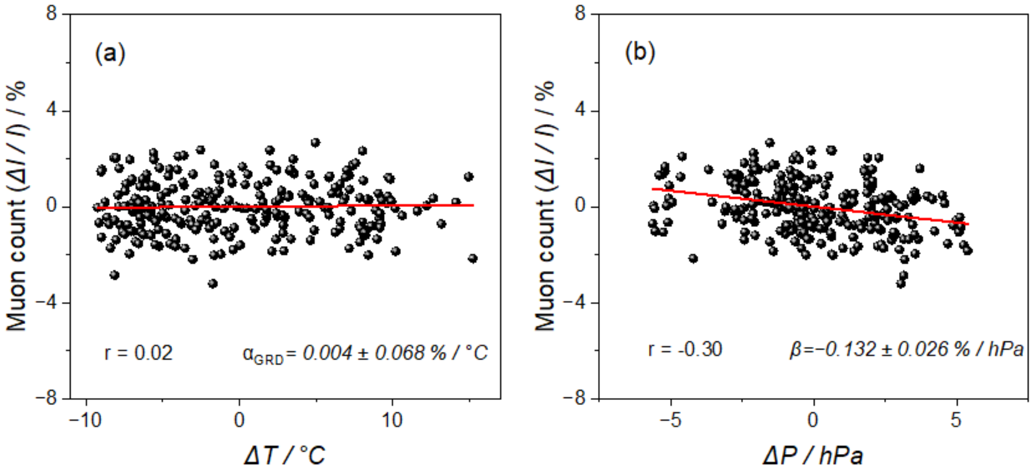

Figure 3.4: *Scatter plots of relative variations in muon count rate (ΔI/I, %) as a function of (a) ground temperature (ΔT, °C) and (b) atmospheric pressure (ΔP, hPa) during the Athens campaign. Each panel includes the linear regression fit (red line) and the corresponding correlation coefficient r.*

For neutrons, Figure 3.3b shows the liquid scintillator neutron count rate (black) plotted against ground temperature (Gray) for 22 July to 3 August 2023. The neutron signal displays more pronounced short-term variability and occasional sharp drops. Meanwhile, the temperature exhibits a regular daily cycle with amplitudes exceeding 15 °C. These observations suggest that local atmospheric conditions, such as daily temperature variations, may indirectly influence neutron moderation and detection (Zuo et al., 2022).

The correlation plots in Figure 3.5a–c provides further evidence. The thermal neutron flux shows only a weak dependence on pressure (r = 0.05), which can be attributed to the limited time period considered for the analysis (22 July – 3 August 2023). But a strong negative correlation with ground temperature (r = –0.80) and a strong positive correlation with relative humidity (r = 0.74). Increased humidity enhances neutron moderation, since hydrogen-rich air more effectively thermalizes fast neutrons, leading to enhanced counts in the thermal range. Together, these results demonstrate that while muons are primarily sensitive to pressure, thermal neutrons are strongly influenced by both temperature and humidity, underscoring the necessity of multi-parameter atmospheric characterization in SCR studies.

Pressure correction significantly reduces atmospheric effects in muon data, while ground temperature correction improves neutron stability as we can see from Figure 3.6. These corrections are essential for ensuring reliable SCR variability analysis across campaigns.

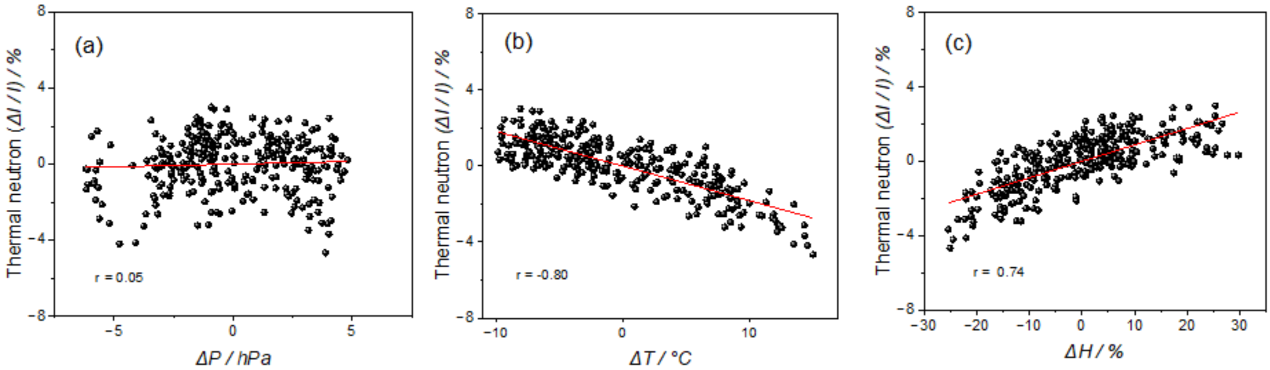

Figure 3.5: *Scatter plots of relative variations in thermal neutron flux (ΔI/I, %) as a function of (a) atmospheric pressure (ΔP, hPa), (b) ground temperature (ΔT, °C), and (c) relative humidity (ΔH, %). Linear regression fits (red lines) and correlation coefficients are shown in each panel.*

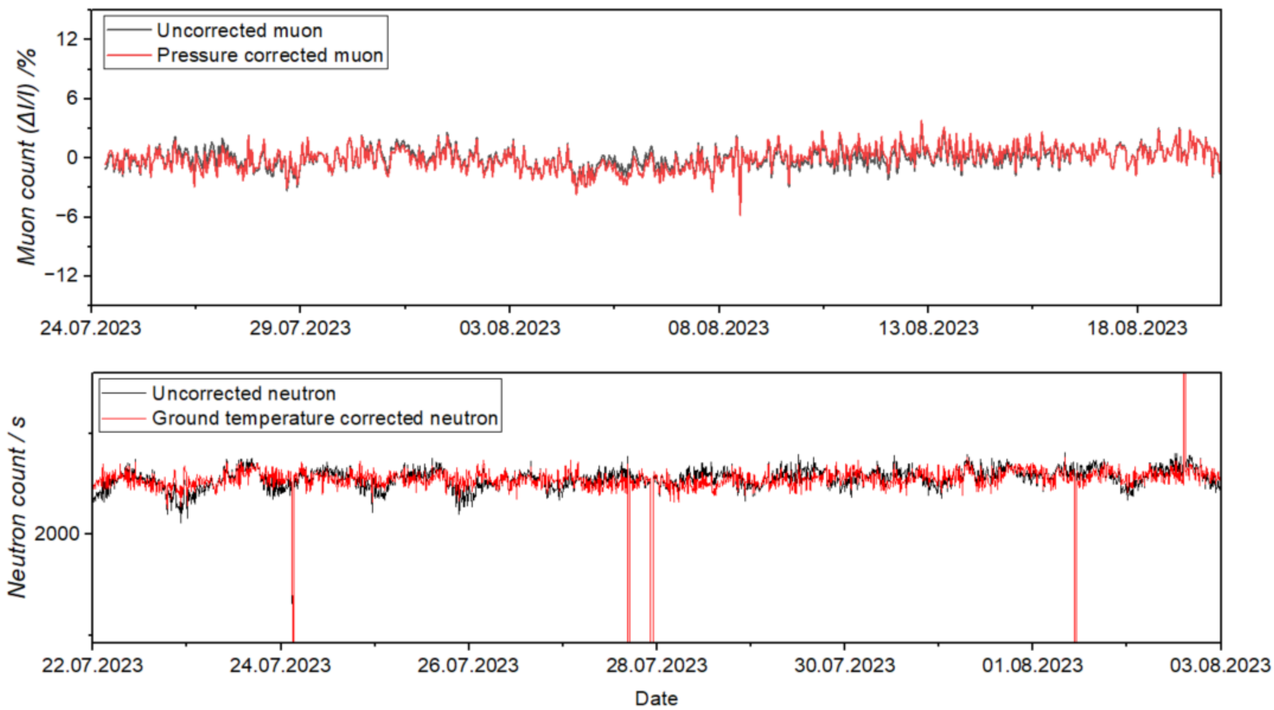

Figure 3.6: *Time series of muon (top) and neutron (bottom) count rates during the Athens campaign. Black curves show uncorrected data, while red curves represent pressure-corrected muons and ground temperature-corrected neutrons.*

3.1.2 Observations of PROBA-V/EPT

The Energetic Particle Telescope (EPT) onboard the ESA PROBA-V satellite provides high-resolution measurements of charged particle fluxes in the Earth's radiation belts and during solar energetic particle events (Pierrard et al, 2014). Developed by the Center for Space Radiation (CSR) at UCLouvain in Belgium in collaboration with the Royal Institute for Space Aeronomy and QinetiQ Space, the instrument was launched on 7 May 2013 into a sun-synchronous polar Low Earth Orbit (LEO) at 820 km altitude (inclination 98.73°). Its design is based on the energy-dependent stopping power of charged particles, allowing real-time, contamination-free discrimination between electrons, protons, alpha particles, and heavier ions. The EPT consists of two measurement sections: the Low Energy Section (LES) dedicated to low-energy electron fluxes, and the High Energy Section (HES), which measures higher-energy electrons, protons, and heavy ions. During the Athens campaign period, EPT data served as complementary space-based observations of geomagnetic activity and particle injections into the magnetosphere.

Figure 3.6 presents the differential flux of electrons in the radiation belts from June to August 2023, averaged over L-time bins of size (0.25L, 3h). Six energy channels are shown, ranging from 0.5–0.6 MeV up to 2.4–2.5 MeV. The electron dynamics in the outer radiation belt (L ≥ 2.5) clearly reflect the sensitivity of this population to geomagnetic disturbances. Two moderate geomagnetic storms were recorded during this period: 16 June and 5 August. Both events triggered electron dropouts in the outer belt, followed by rapid flux enhancements due to injections at the inner edge of the outer belt. These signatures are typical storm-time processes, where magnetospheric wave-particle interactions and radial transport drive rapid variability. Importantly, while electron precipitation at high geomagnetic latitudes can increase ionization in the mesosphere and lower thermosphere, no direct impact on atmospheric conditions over Athens (low geomagnetic latitude) is expected from these events.

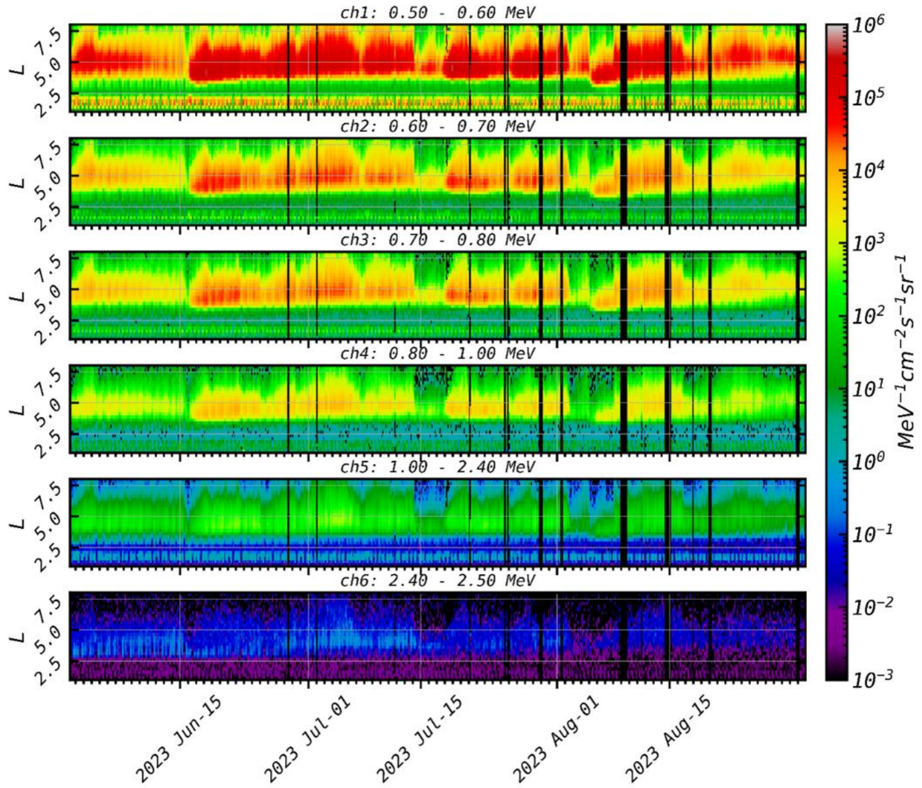

Figure 3.6: *Differential flux of electrons in the radiation belts measured by the Energetic Particle Telescope (EPT) onboard the PROBA-V satellite during June–August 2023.*

Figure 3.7 shows the corresponding proton fluxes measured by the EPT over the same period. Under quiet conditions, protons above 9.5 MeV are confined to the inner belt (L ≤ 2.5) and are mainly observed in the South Atlantic Anomaly (SAA). At L ≥ 2.5, protons appear only during Solar Proton Events (SPEs), when solar protons accelerated by coronal mass ejections (CMEs) or corotating interaction regions (CIRs) penetrate the magnetosphere. Four SPEs were detected between June and August 2023, the most prominent on 18 July. However, all remained relatively weak, with protons observed only in the first three channels (up to ~61 MeV). These events, while detectable by the EPT, did not produce fluxes intense enough to cause significant perturbations in middle- or low-latitude atmospheric ionization, including the Athens campaign region.

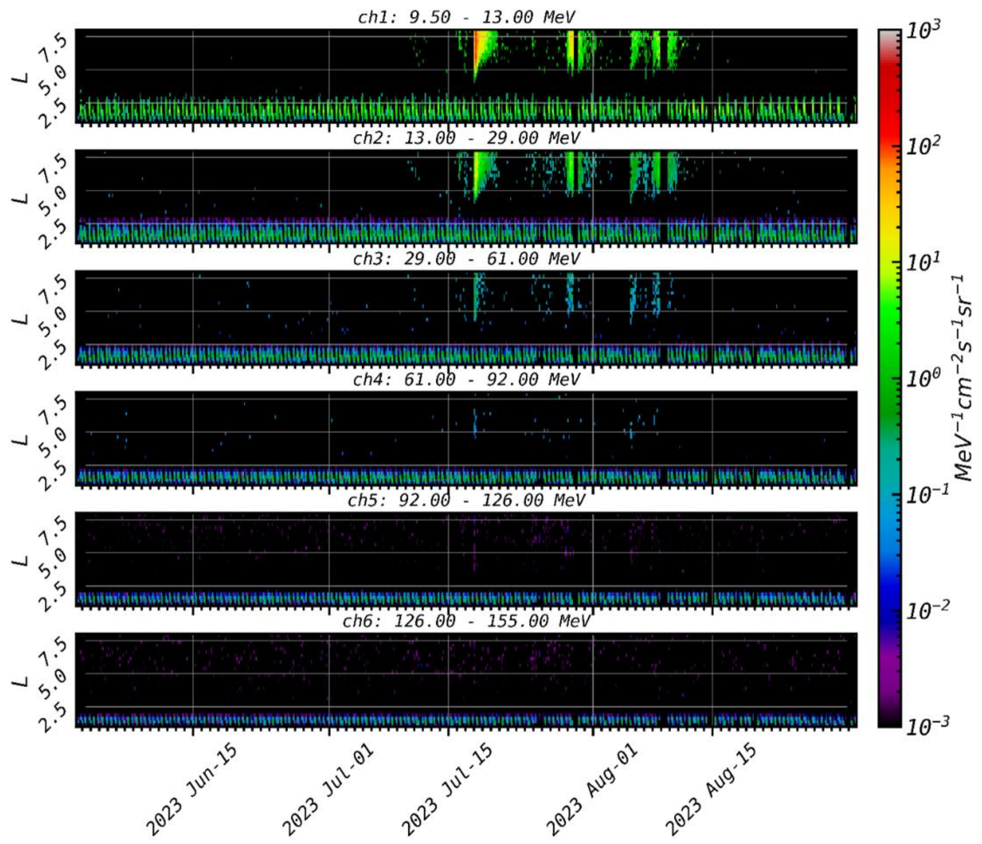

Figure 3.7: *Differential flux of protons in the radiation belts measured by the EPT onboard PROBA-V during June–August 2023. Panels correspond to six proton energy channels from 9.5–13 MeV (top) up to 126–155 MeV (bottom).*

In summary, the PROBA-V/EPT observations highlight the modest geomagnetic activity and solar particle conditions prevailing during the Athens campaign period. The electron belt variability was dominated by two moderate storms, while proton fluxes remained low, with no major solar proton event recorded.

3.1.3 Measurements of UV and TOC

During the Athens campaign, ground-based measurements of ultraviolet (UV) radiation and total ozone column (TOC) were conducted using a combination of UV spectroradiometers, multichannel radiometers, and sun-tracking systems. Figure 3.8 summarizes the temporal evolution of UVA, UVB, and the UV Index, together with TOC, total SO_2 column (TC-SO_2), and the solar zenith angle (SZA) between June and August 2023.

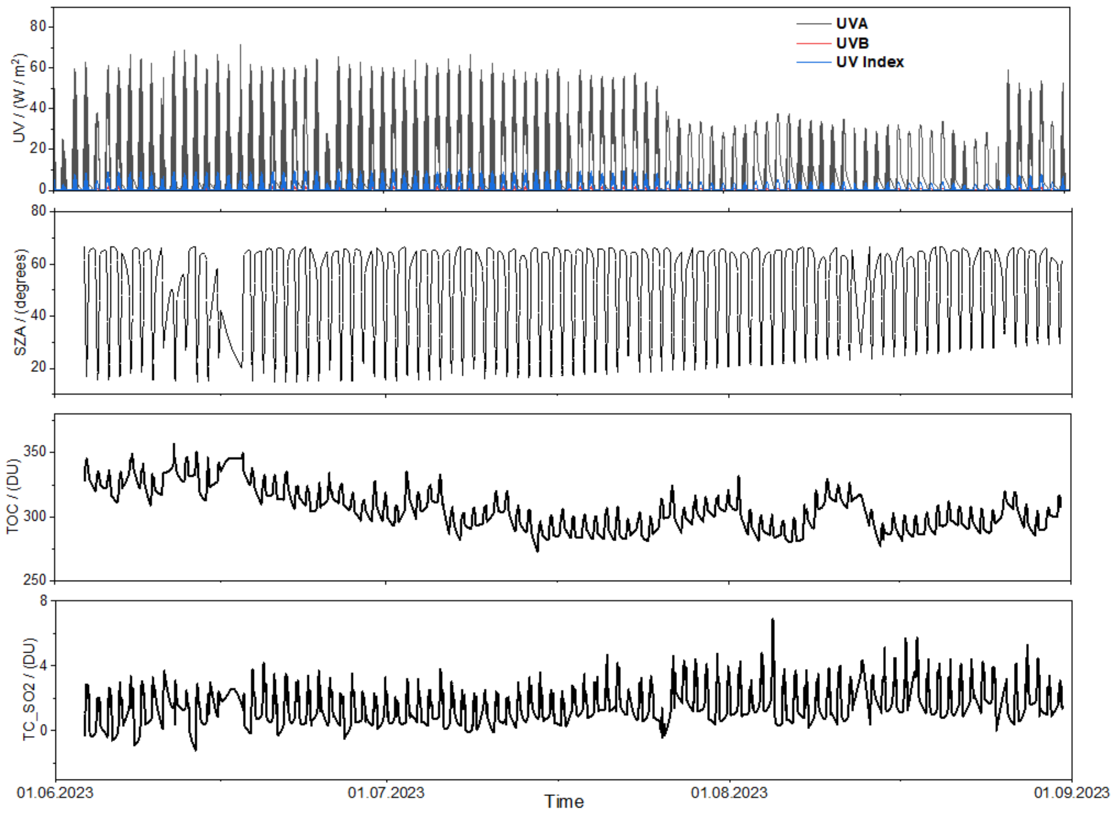

Figure 3.8: *Time series of ground-based UV and atmospheric composition parameters during the Athens campaign (June–August 2023). From top to bottom: UVA, UVB, and UV Index; Total Ozone Column (TOC); Total SO_2 column (TC-SO_2); and Solar Zenith Angle (SZA).*

The UV Index was measured using three instruments: a BTS spectroradiometer (Gigahertz-Optik BTS2048-UV, DWD), a UV pyranometer (EKO UV pyranometer, BIRA-IASB), and a GUV radiometer (GUV-2511, BIRA-IASB) (see Section 2.2 for instrument details). The BTS was intended as the reference instrument, but from Day 60, it experienced overheating. Consequently, data from Days 60–75 are invalid. The instrument was removed, repaired by the manufacturer (Gigahertz-Optik, Germany), recalibrated, and returned only for the final part of the campaign.

The UV pyranometer showed good stability relative to the initial BTS reference, with a mean bias error (MBE) of 4% and a moderate standard deviation (STD = 6.55%), as shown in Figure 3.9. The lower panel of the figure indicates that these discrepancies are most pronounced at high solar zenith angles (low sun elevation), implying that differences during typical daytime measurements were smaller. Therefore, the UV pyranometer was adopted as the reference for UV Index evolution during the campaign, and its values were used for further analyses (e.g., correlation with SCR).

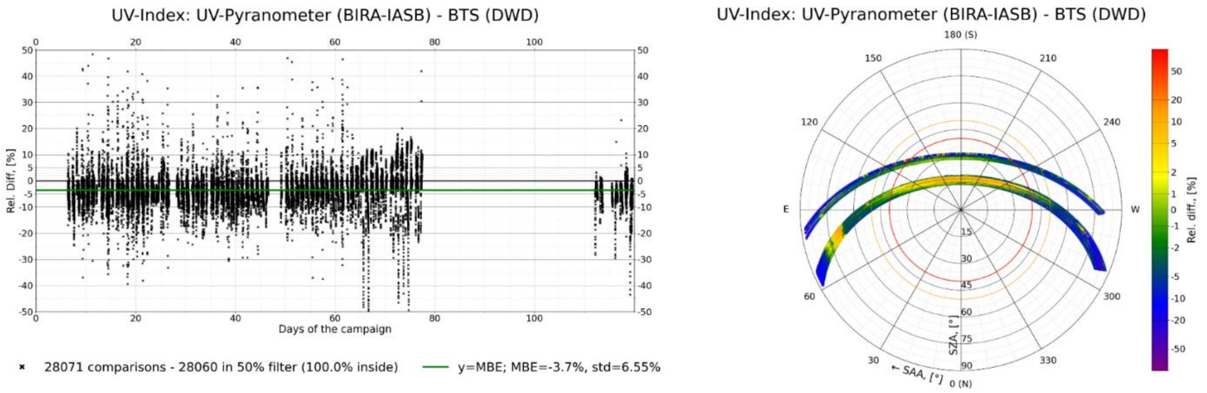

Figure 3.9: *Relative differences (%) in UV Index between the UV pyranometer and BTS: (left) time series over the campaign (individual measurements shown); (right) distribution as a function of solar zenith angle (radius) and solar azimuth angle (angle).*

The UV radiation (top panel) shows a strong daily cycle, with maxima around local noon, consistent with variations in solar zenith angle. Periods of reduced amplitude correspond to cloudy conditions, which are relatively rare in the Athens Basin during summer. The solar zenith angle (SZA) directs the observed UV variability, with smaller angles in July corresponding to the highest UV levels.

The TOC (280–350 DU) shows variability consistent with climatological values for the Eastern Mediterranean in summer. A gradual decrease in July followed by recovery in August was observed, in line with the seasonal ozone cycle. The comparison of TOC with UVB radiation (Figure 3.10a) highlights the expected anti-correlation: lower ozone columns allow stronger penetration of UVB to the ground, whereas higher TOC values correspond to suppressed UVB. The TC-SO_2 record remained generally low (<2–4 DU) as illustrated in Figure 3.10b, indicating the absence of significant volcanic or anthropogenic SO_2 plumes (Georgoulias *et al.*, 2009).

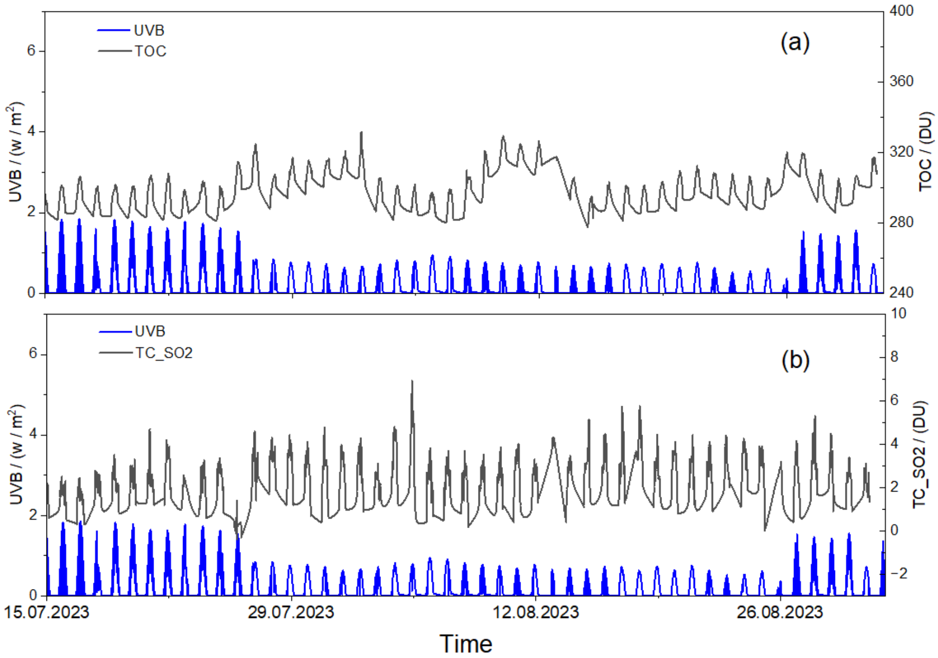

Figure 3.10: *(a) Comparison of UVB irradiance with TOC, illustrating the anti-correlation between ozone abundance and surface UVB levels. (b) Comparison of UVB irradiance with TC-SO_2, showing the effect of episodic SO_2 enhancements on surface UVB radiation.*

3.1.4 Measurements of the Vertical Atmospheric Profile with LIDAR Systems

The Light Detection and Ranging (LIDAR) technique is a powerful remote sensing tool for retrieving range-resolved vertical profiles of atmospheric parameters such as density, temperature, pressure, and wind, as well as gas concentrations (e.g., water vapor) and aerosol properties. A typical lidar system consists of a transmitter, which emits laser pulses in the ultraviolet to near-infrared spectral range (355–2000 nm), and a receiver equipped with optical and opto-electronic subsystems that detect the backscattered radiation. Pulsed laser systems are commonly used for aerosol profiling, while lasers at 532 nm are widely employed for atmospheric density and temperature retrievals.

The NTUA LIDAR systems have been upgraded to meet the BIOSPHERE project's requirements, which include temperature profiling up to 22–25 km with 1 K accuracy at 1 min temporal resolution and density and aerosol mass concentration profiling with better than 10% accuracy up to 25 km at 15–30 min resolution. These improvements concentrate on two tactics: (i) increasing the emitting laser's power to amplify the backscattered signal, and (ii) improving the receiver system to reduce ambient background noise and increase the signal-to-noise ratio.

During the Athens campaign, the EOLE lidar system operated at NTUA provided continuous vertical profiling of aerosols and atmospheric structure. Figure 3.11 illustrates the spatio-temporal evolution of the range-corrected lidar signal (RCS) at 1064 nm for the period 22–25 August 2023. In this figure several aerosol layers are observed between 2-5 km height, indicating the presence of mixed air masses containing Saharan dust and biomass burning aerosols, over the Planetary Boundary Layer (ground up 1.5-2.0 km height) the latter being influenced by local aerosol emissions (Gidarakou et al., 2025). It is interesting to note the formation of clouds, seen with dark brown colours between 4-5 km height (22-23.08.25) and 1.5-3.2 km (24-25.08.25).

These clouds together with the presence of desert dust and smoke aerosols play a crucial role in reducing UV-B levels by 30-62% at ground level (Gidarakou et al., 2025).

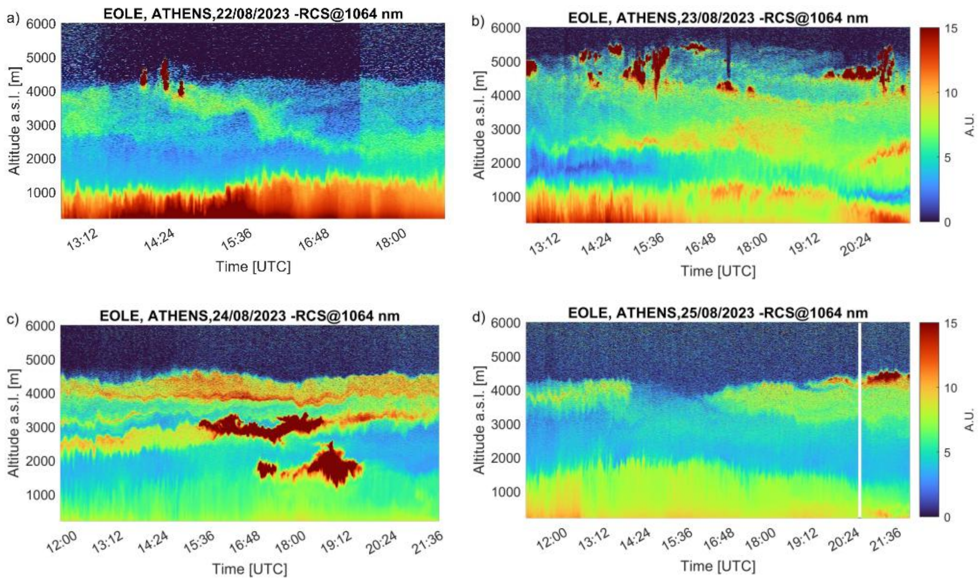

Figure 3.11: *Spatio-temporal evolution of the range-corrected lidar signal (RCS) at 1064 from 22 to 25 August 2023 obtained by the NTUA EOLE lidar (Gidarakou et al., 2025).*

Complementary vertical profiles of 24 August 2023 (Figure 3.12) provide detailed insight into aerosol microphysical properties. Profiles of aerosol backscatter and extinction coefficients at 355, 532, and 1064 nm (Figure 3.12-a-b) indicate the presence of aerosol layers up to 4.8 km height, poorly depolarizing (less than 8%), with enhanced aerosol concentrations (mean value of 30 ug/m^3 between 3.2-4.8 km) of fine (biomass burning-blue line) and coarse (desert dust-red line) particles.

Together, these measurements demonstrate the crucial role of lidar observations in characterizing the vertical distribution of aerosols and atmospheric parameters, providing essential input for evaluating the correlation between cosmic rays, UV radiation, and atmospheric composition within BIOSPHERE.

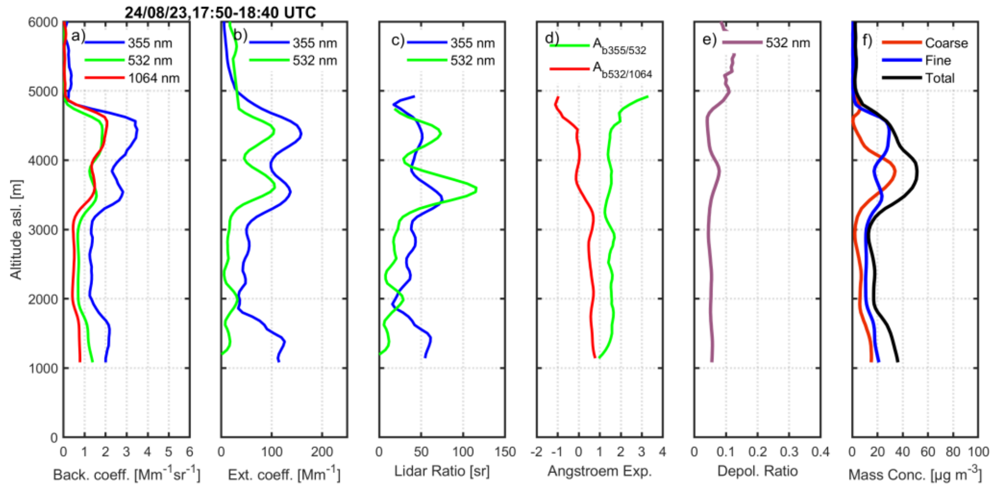

Figure 3.12: *Vertical profiles of aerosol (a) backscatter coefficient (355, 532 and 1064 nm) (b) extinction coefficient (355 and 532 nm) (c) lidar ratio (355 and 532 nm) (d) Ångström exponent (e) depolarization ratio (532 nm) and (f) aerosol mass concentration (coarse, fine mode and total particles) obtained by the EOLE and DEPOLE NTUA lidar systems on 24 August 2023 (17:50-18:40 UTC) (Gidarakou et al., 2025).*

3.2 SpacePole site in Brussels Campaign

The BIOSPHERE campaign in Brussels was co-organized by the Royal Belgian Institute for Space Aeronomy and the Royal Meteorological Institute of Belgium, BIRA-IASB and IRM (known as KMI-IRM), respectively. Both institutes are located in the southern part of Brussels at the Spacepole site located in Uccle (Avenue Circulaire, Brussels, Belgium, 50.797° N, 4.357° E, at ~100 m a.s.l.). It is an urban site situated on a flat area and close to a forest.

Figure 3.13: *Left: aerial view of the Spacepole site in Brussels. Right: general view of the BIRA-IASB building.*

Figure 3.14: *Left: general view of IRM. Right: close-up view of BIRA-IASB.*

During this campaign, both institutes played an active role, providing extended infrastructures and measurement capabilities for the monitoring of solar irradiance, meteorological and atmospheric parameters, with controlled quality assurance using their own and pertinent instruments available. Partners from Germany, Hungary and Czechia also participated in this campaign. They provided high level instrumentation and key contributions for the monitoring of Secondary Cosmic Rays (SCR), Aerosol Optical Depth (AOD) and Total Ozone Column (TOC). The installation of their equipment was managed by BIRA-IASB. A detailed description of the instruments is presented below.

IRM instrumentation

- Vertical profiling of the atmosphere using automatic ceilometer-LIDAR and balloon-borne radio- and ozonesondes (launched three times per week) measuring ozone, temperature, pressure, humidity, and wind profiles, as well as precipitation radars,
- A comprehensive suite of instruments from both official and research-grade weather stations.
- Measurements of UV index and columnar parameters, including total column of ozone, performed using Brewer ozone spectrophotometers,
- Neutron monitoring station (Dourbes, ~100 km away from Brussels, *http://ionosphere.meteo.be/instruments/neutron.php*).

Figure 3.15: *Left: Brewer spectrophotometers measuring solar UV and total ozone column. Right: balloon-borne ozone sondes measuring the vertical profile of atmospheric ozone concentrations.*

Figure 3.16: *Automatic LIDAR Ceilometer measuring the backscattering signal by aerosols, fog and clouds.*

BIRA-IASB instrumentation

- AOD using a CIMEL sunphotometer,
- Solar irradiance parameters: global UVB, UVA and Total (from 300 nm to 3000 nm), broadband solar irradiance measurements with pyranometers. UV index measurements with UVB pyranometer, a multi-channel filter radiometer and a double monochromator.

Figure 3.17: *Left: UVB pyranometer (model MS-212W from EKO) and multi-channel radiometer (GUV-2511 from Biospherical), installed on the roof of BIRA-IASB. Center: Gigahertz Optik BTS2048-UV for AOD and TOC measurements. Right: neutron detector from BFKH (Hungary).*

Instrumentation from the partners

- Monitoring of muons flux using instruments from PTB (Germany) installed in a trailer, parked close to the BIRA-IASB building,
- AOD and TOC using a spectroradiometer in direct Sun mode (from Gigahertz Optik, Germany),
- Monitoring of neutron flux (instruments from BFKH, Hungary and UFJ-NPI, Czechia).

Figure 3.18: *In the PTB trailer, from left to right: PTB muon detectors DECOS-2 and MUDOS, the neutron detector from UJF-NPI.*

The Spacepole campaign took place officially from January 1 to March 30, 2024 (with some extension in December 2023 and April-May 2024), covering winter and spring weather conditions. Preparation and coordination of the campaign were carried out nominally by the BIRA-IASB and IRM staff, with no major issues encountered (for example: power cut). This campaign provided good opportunities to collect valuable data, particularly due to the high level of solar activity observed in March 2024 (and May 2024 for instruments still installed).
The data collected within the frame of the BIOSPHERE (EURAMET) project consist of measurements of secondary cosmic radiation (SCR), ground-level solar UV irradiance, total ozone column and atmospheric parameters (including vertical profiles).

3.2.1 Measurements of Secondary Cosmic Rays on the Ground

Secondary cosmic rays were measured during the Brussels campaign by the Physikalisch-Technische Bundesanstalt (PTB, Germany) using the DECOS2 muon detector, by the Nuclear Physics Institute of the Czech Academy of Sciences (NPI, Czech Republic) and the Royal Meteorological Institute of Belgium (RMI, Dourbes, Belgium) using neutron monitors. Figure 3.19 shows the time series of hourly muon count rates recorded at Brussels, plotted together with surface pressure measured at Dourbes. The anti-correlation between muon flux and atmospheric pressure is clearly visible.

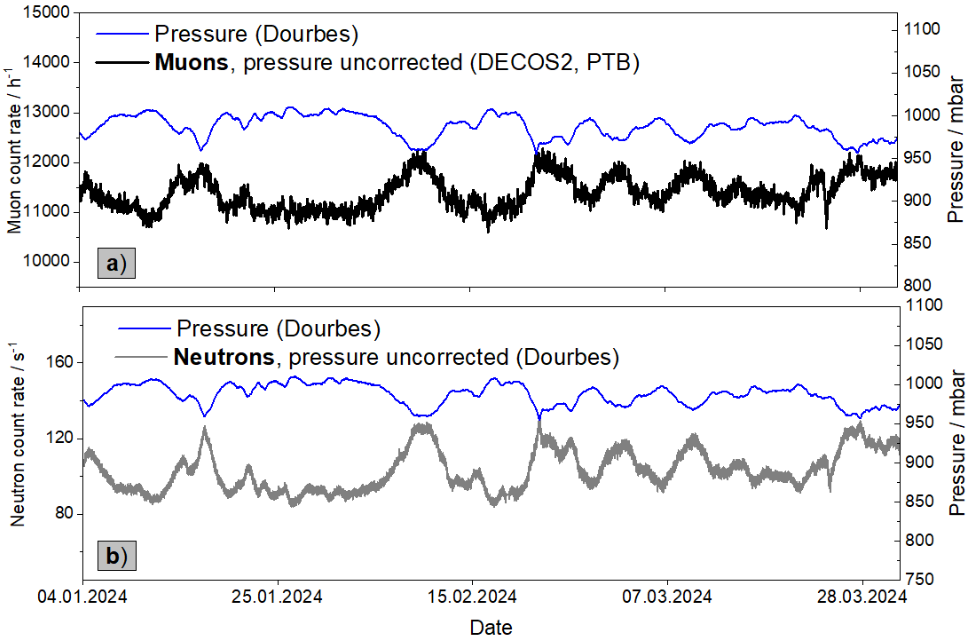

Figure 3.19: *(a) Hourly muon count rate (pressure uncorrected, DECOS2 at PTB, black) compared with surface pressure at Dourbes (blue) from January to March 2024. The data show an anti-correlation between cosmic ray flux and atmospheric pressure. (b) Neutron count rate and corresponding surface pressure (blue) over the same period.*

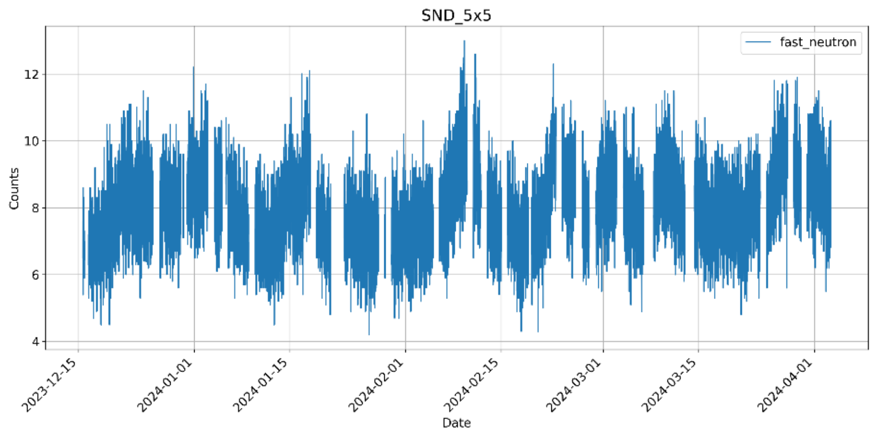

Figure 3.20: *Fast neutron counts rates recorded during the BIOSPHERE campaign (mid-December 2023 to mid-April 2024).*

Figure 3.19b, presents the corresponding neutron monitor data (pressure-uncorrected, Dourbes) together with the local pressure. Similarly, a Forbush decrease signature is evident during the same solar event. Figure 3.20 depicts the fast neutron counts collected over the entire observation period. The data show the expected variability driven primarily by changes in surface pressure. Several gaps are visible in the time series, corresponding to temporary instrument failures.

3.2.2 Observations of PROBA-V/EPT

The EPT space instrument provided in-situ measurements of space radiations (radiation belt electrons and solar protons) on board the PROBA-V Belgian satellite. The electron and proton fluences are measured along respectively 6 channels and 10 channels (depending on energy levels). In Figures 3.21 and 3.22 we show proton and electron flux measured from 1 January 2024 to 31 March 2024 by PROBA-V/EPT in 3 energy channels respectively. EPT data provided a continuous monitoring from space and helped to detect SPEs during the Brussels campaign. The first two months (January and February 2024) of the second measurement campaign in Brussels were very quiet in term of geomagnetic activity. Only weak SPEs were observed on January 4, 22 and 28 and in February 10 and 13. However, the second part of the campaign (i.e. March) was much more dynamic both for solar protons and geomagnetic activity. Geomagnetic indices show two strong events. The first one occurred on March 3 and the second one on March 24. For these latest, strong solar protons fluxes were recorded.

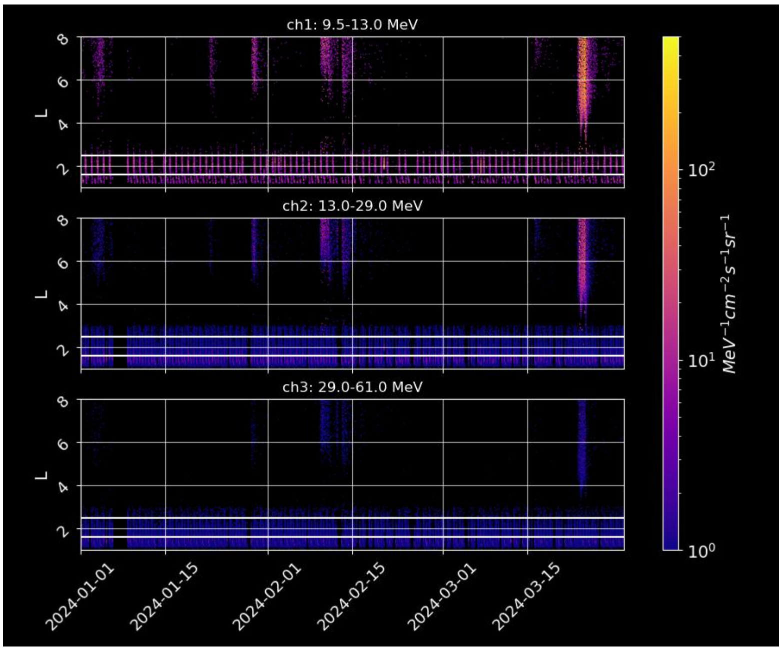

Figure 3.21: *Proton flux measured from 1 January 2024 to 31 March 2024 by PROBA-V/EPT in 3 energy channels*

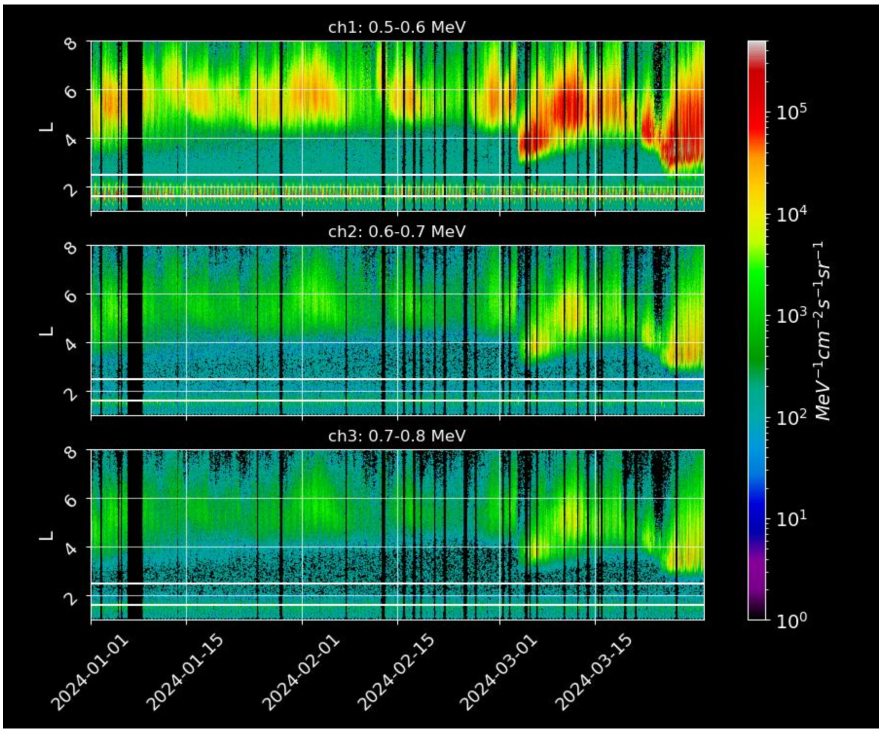

Figure 3.22: *EPT monitoring for the electron fluence. Two events are visible on March 3 and 24 2024.*

The Mother's Day event (11 May 2024), the strongest SPE since 20 years occurred after the official end of the campaign but was also monitored by EPT. This event induced a sharp increased ionization rate that affected the ozone concentration in the stratosphere. EPT measurements for the proton and electron fluences are presented in Figure 3.23.

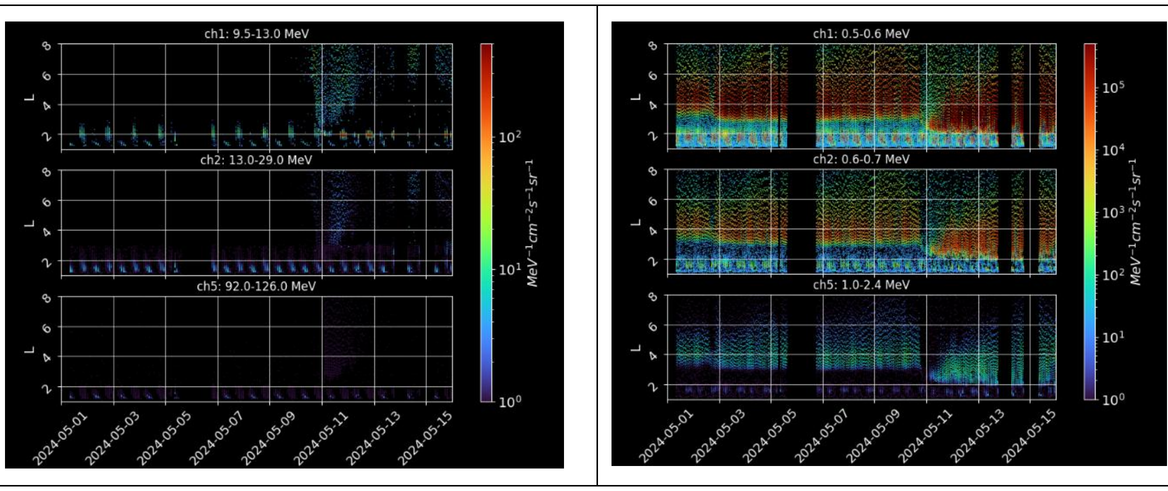

Figure 3.23: *EPT monitoring for the electron (right panel) and proton (left panel) fluences during the Mother's day event (11 May 2024).*

3.2.3 Measurements of UV and TOC

Several partners of the BIOSPHERE project, namely the IRM, and the Royal Belgian Institute for Space Aeronomy conducted measurements of solar UV irradiance and total ozone column.

For ozone and UV, the IRM deployed a Brewer MK II spectrophotometer. The daily maximum UV index measured from January to May 2024 shows a clear temporal increase, reflecting the seasonal transition from winter to early summer as showed in Figure 3.24.

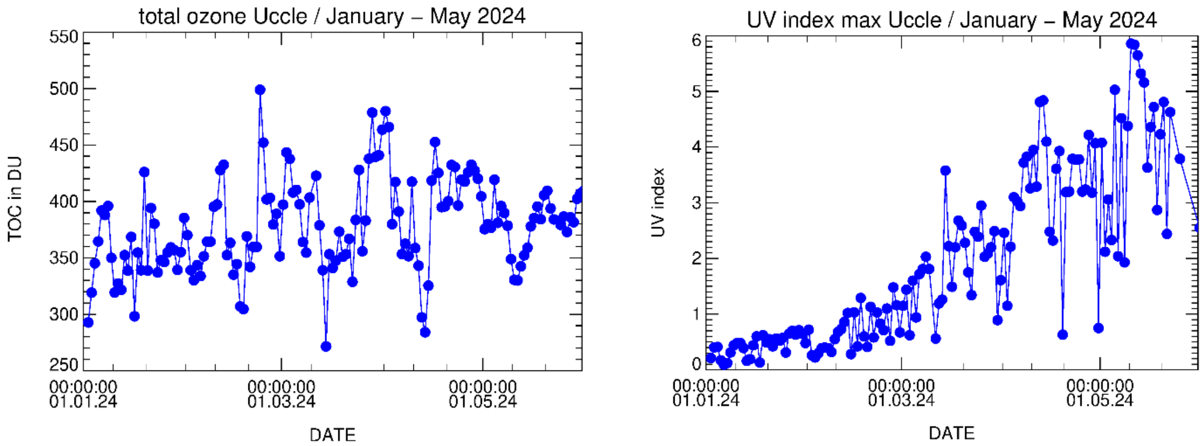

Figure 3.24: *TOC measurements. Maximum UV index measured in Uccle for the period from January 2024 to June 2024.*

Additional UV data were obtained using a DTM300 double monochromator (BIRA-IASB), a GUV radiometer (BIRA-IASB), and a pyranometer Model MS-212W (BIRA-IASB). To assess the consistency of UV measurements across instruments, a direct comparison was performed between different radiometers operated at BIRA-IASB. Figure 3.25 illustrates the relative difference between the UV Index measured by the pyranometer and the Bentham double monochromator. On average, the relative difference amounts to approximately 9%. It is stable during the campaign (Figure 3.25) and the sift is systematic without a lot of dispersion (standard deviation “std” is at about 5.5 %). Figure 3.26 shows that there is no sun direction that is worse. Only at sun set and sun rise (Edge of the circle on Figure 3.26, for high SZA (Solar Zenith Angle) corresponding to low sun elevation and high air mass, the Pyranometer has a worse accuracy. This performance is well known for such type of instrument and has been observed in the other campaigns (see Sections 3.1: Athens, 3.3: Milešovka and 3.4: Lindenberg).

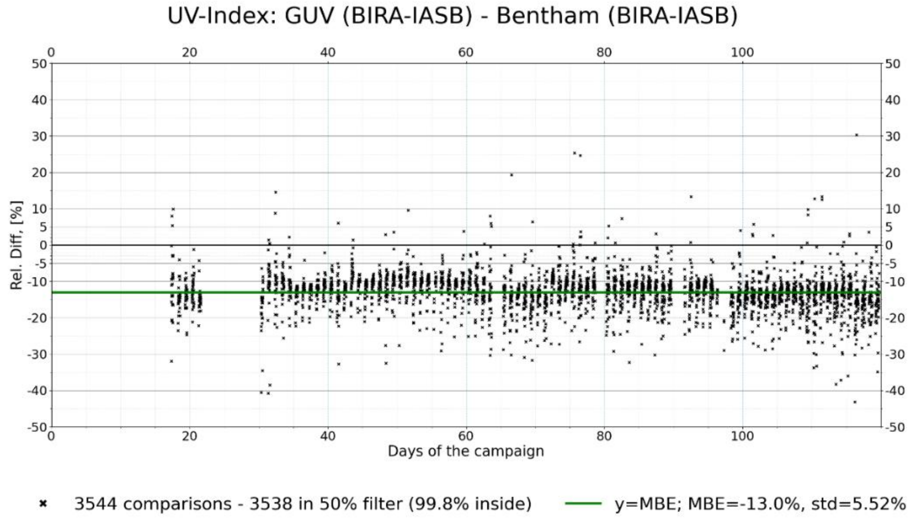

Figure 3.25. *Relative difference of the UV Index measured by the pyranometer and the Bentham spectrometer (reference) as a function of days of the campaign. The mean relative difference (MBE: Mean Bias Error) is shown as a green line.*

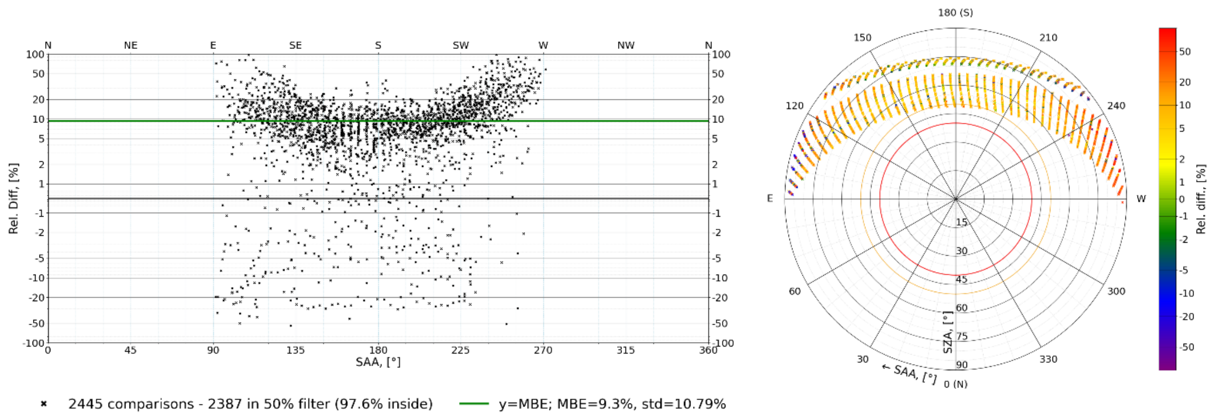

Figure 3.26: *Relative difference of the UV Index measured by the pyranometer and the Bentham spectrometer as a function of solar zenith angle (SZA) and solar azimuth angle (SAA) (right). The mean relative difference is shown as a green line (left).*

In Brussels, a clear anticorrelation was observed between ground-level solar UV irradiance and the total ozone column. Daily ozone measurements performed with the Brewer instrument at RMI, correlated with UV data from BIRA-IASB and DWD instruments showed that higher ozone values systematically correspond to lower surface UV levels. This behavior reflects the absorption of ultraviolet radiation by stratospheric ozone, which effectively shields the biosphere.

This campaign was a success in terms of its implementation and logistics. The site was well equipped for this kind of organization. From a scientific perspective, it should be noted that this campaign coincided with the most interesting and intense SPE thank to high solar activity. The data acquisition was nominal. The data processing allowed the involved teams to perform the most in-depth study of correlations between physical parameters when they were clearly identifiable (for example, between SCRs and atmospheric parameters).

3.3 Milešovka Observatory Campaign

The third measurement campaign was organized by ÚJF CAS during August–November 2024 at Milešovka, Czech Republic. Milešovka observatory (altitude: 840 m, 50.5549050N, 13.9310911E) is located on top of Milešovka hill, which rises 400 meters above its surroundings. It is a 24-hour manned professional meteorological observatory (see Figure 3.27) belonging to the Institute of Atmospheric Physics (IAP) of the Czech Academy of Sciences (CAS). It consists of professional measurements of meteorological data, such as temperature, pressure, dew point, visibility, cloud cover, and solar irradiance. It also contains an X-band weather radar.

Figure 3.27: *Milešovka observatory*

In the frame of the third measurement campaign, the instruments provided by UJF CAS, PTB, GGO, and ADVACAM were installed at selected locations. Instruments used for UV measurements were mounted on the southwest corner of the roof of the observatory, while instruments for measuring SCR were installed inside the SEVAN house (Figure 3.28).

The campaign was originally scheduled to begin from August, but due to the emergency roof repair, the installation of UVB pyranometer, GUV-511 multichannel filters radiometer, BTS-Solar and BTS-Global on the roof of the observatory had to be postponed to mid-August.

Instruments installed inside the SEVAN house (Figure 3.28):

- PTB muon detector
- UJF CAS neutron detector
- ADVACAM Timepix3 SCR particle tracker detectors
- UJF CAS Vaisala CARBOCAP ® Hand-held Carbon Dioxide Meter GM7

Figure 3.28: *PTB muon detector and UJF SEVAN detector, UJF neutron detector, UJF gamma-ray spectrometer RT-56, ADVACAM Timepix3 SCR particle tracker detectors*

Instruments installed on the roof of the observatory (Figure 3.29):

- BTS-direct sun: GHO UV array spectroradiometer BTS2048-UV-Solar (in direct sun modus with sun tracker and collimator) for TOC measurements
- BTS: DWD UV array spectroradiometer BTS2048-UV
- BIRA-IASB UV pyranometer and GUV (GUV-511 multichannel filters radiometer).

  More precision about these instruments in Section 2.2.

Figure 3.29: *The UV-Index and TOC suite: from left to right: BIRA-IASB GUV and UV pyranometer DWD BTS, GHO BTS-direct, on the rooftop platform of Milešovka observatory.*

Instruments already available on the site:

- SEVAN radiation detector
- gamma-ray spectrometer RT-56
- ceilometers
- X-band FURUNO
- METEK MIRA 35c radars

All instruments, except for the METEK MIRA 35c radar, were working nominally. METEK was damaged during a thunderstorm in July and had to be sent for repair.

3.3.1 Measurements of Secondary Cosmic Rays on the Ground

An example of data measured during the 3rd measurement campaign with SEVAN (for selected coincidences/particles) and PTB muon detector is shown in Figure 3.30 and Figure 3.31.

The SEVAN detector consists of three active plastic detectors coupled with photomultiplier tubes and separated by lead. Based on the combinations of the 3-layered detector output, the traversal particle can be identified. If a photon or electron has lower energy, it will trigger only the top channel and thus shows the coincidence of “100”. Neutrons will not trigger the top channel and by interacting with the top lead layer, they will trigger a signal in the middle channel that is thick enough, hence the coincidence of “010”. Muons, on the other hand, trigger signals in all channels they pass and are thus the main part of the coincidence “111&101”.

In SEVAN data we can see anticoincidences of measured counts with the pressure.

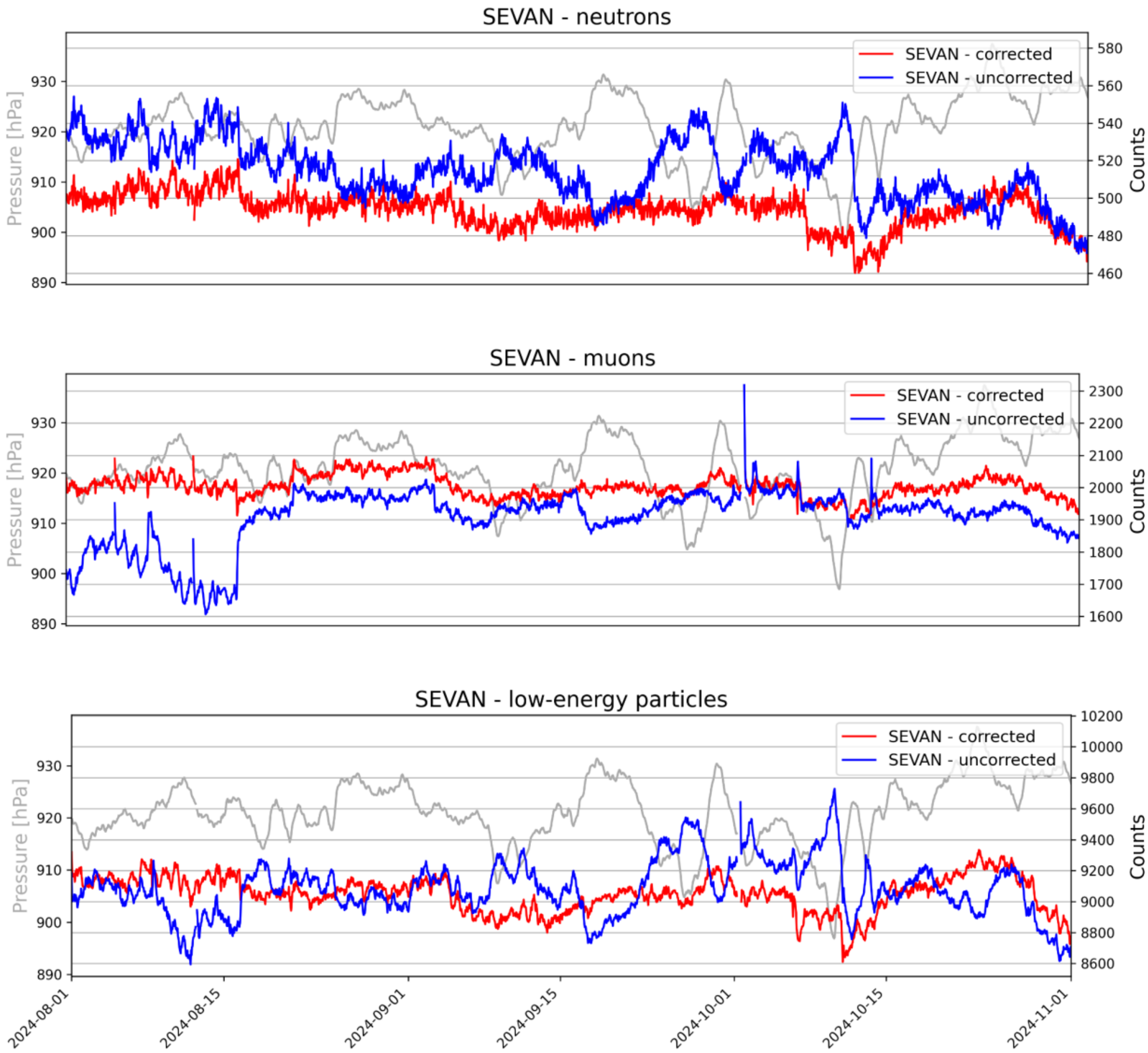

Figure 3.30: *SEVAN uncorrected and pressure and temperature corrected data for selected particles - neutrons, muons, and low-energy electrons and photons.*

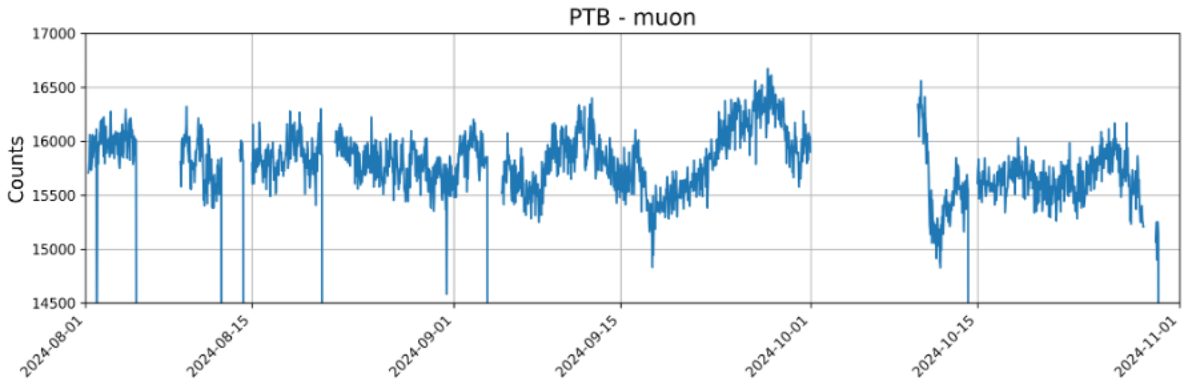

Figure 3.31: PTB Muon measurements

Figure 3.32 shows particles measured by the gamma-ray spectrometer RT-56, for both total counts of all energies corrected on dead time and particles with energy above 3 MeV. The increases in total counts are mainly due to the rain and radon progenies.

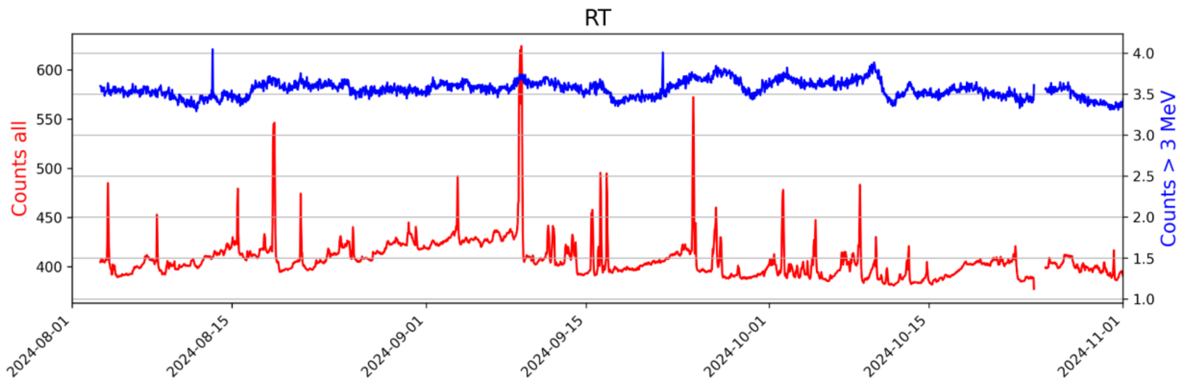

Figure 3.32: *Gamma-ray spectrometer measurements.*

CO2 concentration measurements

CO2 concentration measurements (Figure 3.33) were performed using the portable device Vaisala CARBOCAP® Hand-held Carbon Dioxide Meter GM7.

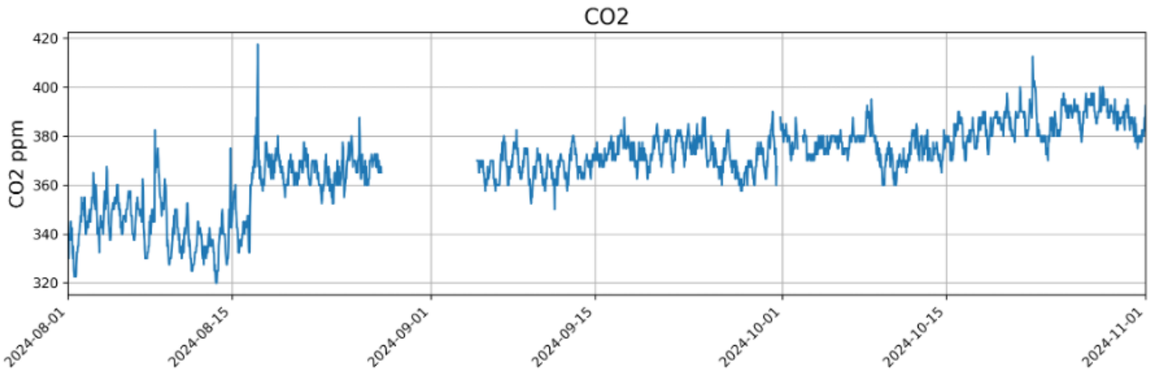

Figure 3.33: *CO2 measurements.*

3.3.2 Observations of PROBA-V/EPT

The Energetic Particle Telescope (EPT) measures the fluxes of high-energy particles in the radiation belts and the injection of solar protons in the magnetosphere. Figure 3.34 shows the time evolution of the electron fluxes as a function of the McIlwain parameter, while Figure 3.35 shows measured proton fluxes.

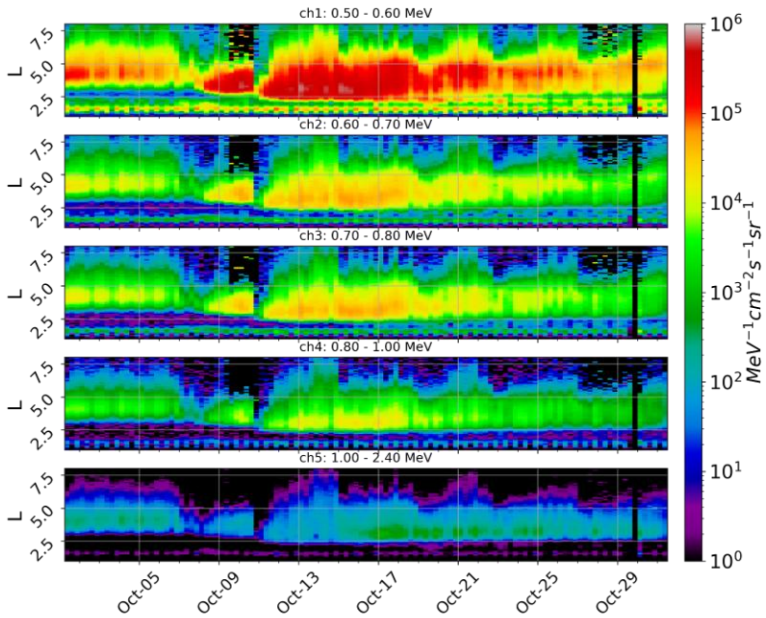

Figure 3.34: *Electron fluxes observed during October 2024 as a function of the McIlwain parameter L (vertical axis in Earth's radii) and time (horizontal axis) for the 5 energy channels of EPT on board PROBA-V.*

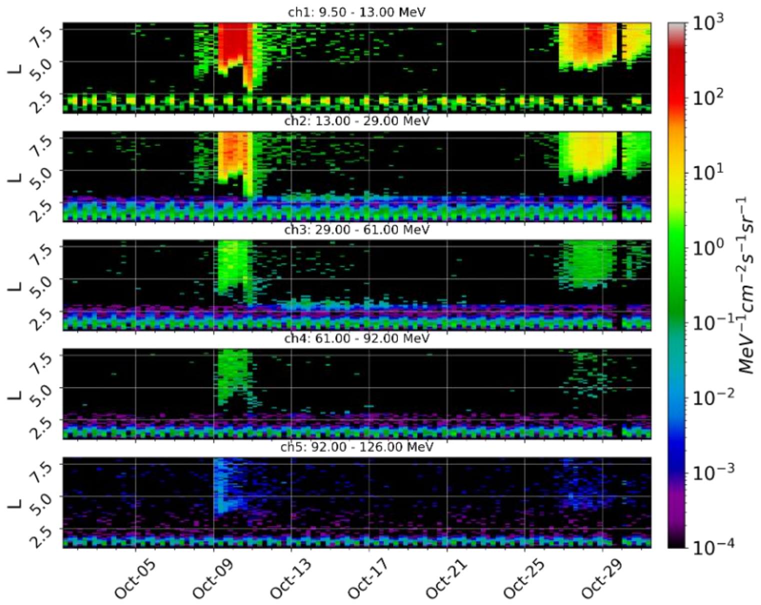

Figure 3.35: *Proton flux measured during October 2024 by PROBA-V/EPT in 5 energy channels.*

3.3.3 Measurements of UV

UV radiation as explain in 3.1 UV was measured by the DWD instrument BTS (reference), GUV and UV Pyranometer as secondary instruments. Figure 3.36 shows, that we have a good agreement between BTS and UV pyranometer, in shift (Mean Bias Error: MBE = 5.6 %), especially in the beginning of the campaign, in late summer / begin autumn when the solar zenith angle (SZA) was lower (it is a difficulty of UV pyranometer: the quality of the measurements is much lower for lower sun elevation: higher SZA): in this time the MBE was in average lower than 3%.

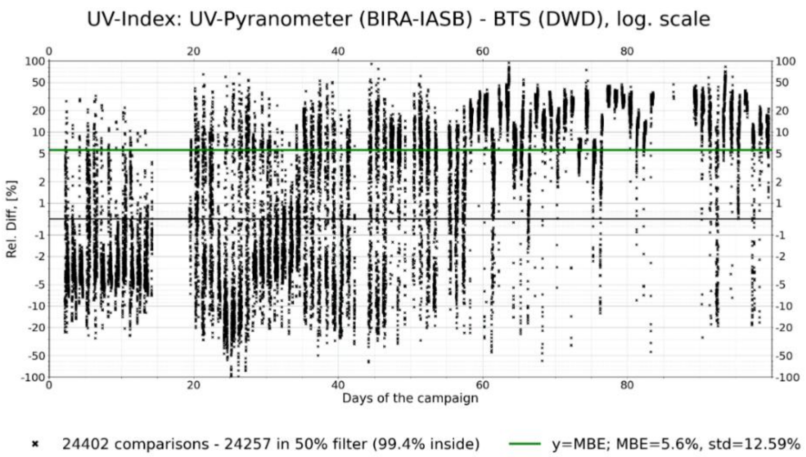

Figure 3.36: *Relative difference of UV-Index UV pyranometer – BTS during the campaign of Milešovka (x = days of the campaign).*

3.4 DWD Lindenberg Campaign

The BIOSPHERE campaign at DWD Lindenberg was organized by the Meteorological Observatory Lindenberg (MOL-RAO) of the German Meteorological Service, DWD (Deutscher Wetterdienst). The Lindenberg site (52.21° N, 14.12° E, 121 m a.s.l.) is located in a rural and flat area of the Brandenburg region, approximately 80 km southeast of Berlin (see Figure 3.37). This site represents one of Europe's most advanced atmospheric research infrastructures and has long been recognized as a reference observatory for meteorology and atmospheric sciences.

The MOL-RAO facilities offer an unparalleled set of instruments for continuous profiling and column measurements of the atmosphere:

- Vertical profiling of the atmosphere: Lidars, ceilometers, and balloon-borne radiosondes (launched every 6 hours, day and night, measuring temperature, pressure, humidity, and wind profiles), cloud and precipitation radars, wind profilers, wind lidars, and microwave radiometers (temperature and humidity profiles).
- Columnar parameter measurements: Photometers (for aerosol parameters such as aerosol optical depth, AOD) and UV spectroradiometers (for total ozone column, TOC).
- Radiation parameters: Global, diffuse, and direct broadband solar radiation measured with pyranometers and pyrheliometers; atmospheric (thermal) broadband radiation measured with pyrgeometers; global and direct spectral radiation in the UV (UV-B and UV-A), visible, and near-infrared (NIR) ranges.
- A complete suite of instruments from both official and research-grade weather stations.

The Lindenberg campaign took place from 15 January to 31 May 2025 (initially scheduled for 1 February to 30 April but extended due to excellent measurement conditions and the absence of other overlapping campaigns). Preparation and coordination were carried out by the DWD MOL-RAO staff in close collaboration with BIOSPHERE partners.

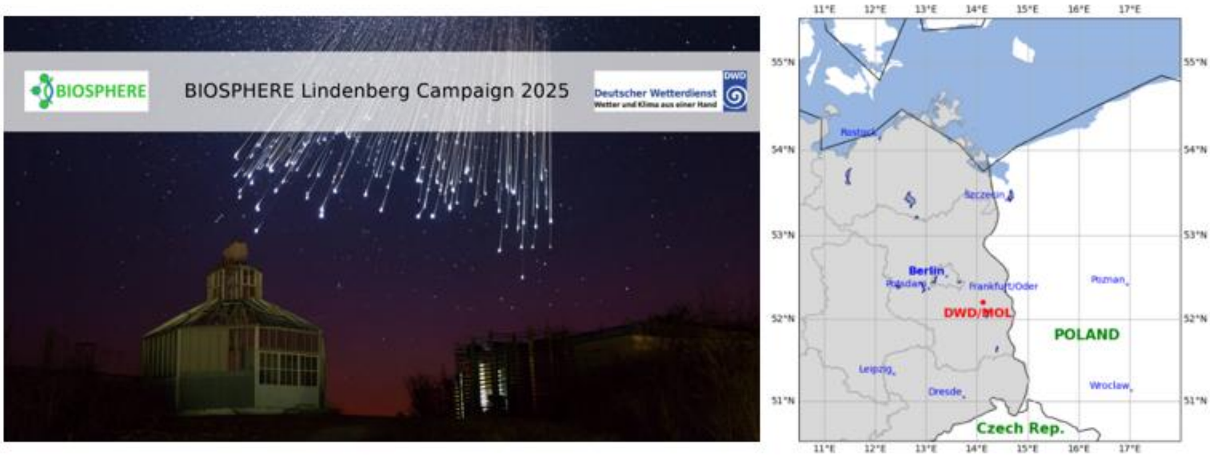

Figure 3.37: *Left: Flyer image of the DWD Lindenberg Campaign, featuring a Google Magic Editor AI–generated cosmic ray shower over the DWD infrastructure in Lindenberg (Tauche). Right: Location of Lindenberg (DWD/MOL) shown on a regional map.*

Instruments for TOC and UV measurements were mounted on the Strahlungsmessplattform (radiation platform) located on the rooftop and inside the Strahlungsmesszentrale (SMZ, Radiation Laboratory) building at MOL-RAO. In parallel, instruments dedicated to the measurement of Secondary Cosmic Rays (SCR) were installed in a dedicated trailer provided by PTB (Physikalisch-Technische Bundesanstalt), positioned ~40 m from the radiation platform (see Figure 3.38).

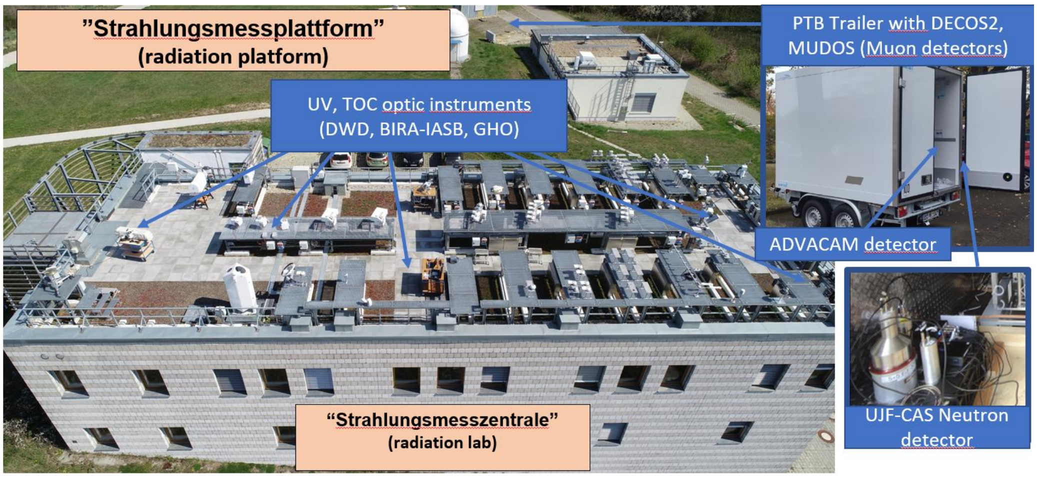

Figure 3.38: *DWD infrastructure provided for the measurement campaign at MOL-RAO: In the foreground is the 'SMZ' building (Strahlungsmesszentrale – Radiation Laboratory), on whose rooftop all TOC and UV measurement instruments were deployed. In the background, a nearby trailer provided by PTB housed all SCR measurement instruments.*

The following instruments were operational at Lindenberg from 15 January 2025, ensuring stable measurements before the official campaign start date:

- Muon detector DECOS2 (PTB): portable position-sensitive muon monitor.
- Neutron detector (UJF CAS): portable liquid scintillator system for fast and thermal neutron monitoring.

- Radiosondes (DWD, RS41-SGP): launched four times daily to provide high-resolution profiles of temperature, humidity, pressure, and wind.
- UV and TOC suite (DWD, BIRA-IASB, GGO): including Brewer and Bentham spectroradiometers, UV spectroradiometers with BTS solar sun tracker, and GUV-511 multichannel radiometer.
- ADVACAM instrument: installed in the PTB trailer for particle and radiation environment monitoring.

Figures 3.39–3.41 illustrate the SCR instruments deployed at Lindenberg, alongside the radiation measurement platform and UV/TOC systems. Detailed technical descriptions of all instruments are provided in Section 2 (On the Ground Instrumentation Overview).

Figure 3.39: *Secondary Cosmic Rays (SCR) instrumental suite of the DWD Lindenberg Campaign in the PTB trailer (left) at MOL-RAO. Inside the trailer (right): PTB muon detectors MUDOS ("M") and DECOS-2 ("D"), and the UJF-NPI neutron detector ("N"). Not shown in the picture, but also present in the trailer during the campaign, were ADVACAM Timepix micro-telescopes.*

Figure 3.40: *TOC (Total Ozone Column) instrumental suite of the DWD Lindenberg Campaign on the rooftop of MOL-RAO 'SMZ' building. Left: DWD instruments Brewers and Dobson (background). Middle: DWD BTS2048-UV in direct-sun mode. Right: Gigahertz-Optik BTS2048-UV in direct-sun mode.*

Figure 3.41: *UV instrumental suite of the DWD Lindenberg Campaign on the rooftop and in the MOL-RAO 'SMZ' building. Left: DWD Bentham DTM 300 (below) and BIRA-IASB Bentham DTM 300 (above right), with their optical entrance on the roof (above left). Middle: BIRA-IASB GUV-511 multi-filter radiometer (left) and UV-Pyranometer (right). Right: DWD BTS2048-UV in global measurement mode.*

3.4.1 Measurements of Secondary Cosmic Rays on the Ground

During the DWD Lindenberg campaign, SCR were continuously monitored using the PTB mobile muon detector DECOS2 and the UJF CAS liquid scintillator neutron detector (see Section 2.1). These instruments were installed in a dedicated PTB trailer located ~40 m from the main Strahlungsmessplattform, providing stable environmental conditions for long-term data acquisition. The Timepix detectors stack telescopes were included too. They provide the wide-range spectral and composition characterization of the SCR field as shown in Figure. 3.42. Data are shown integrated over a selected time interval – e.g. 52 minutes in the figure. The large track in subplot (b) in Figure 3.42 is produced by a fast neutron interacting on the 1000 um Si sensor of the TPX3 bottom detector.

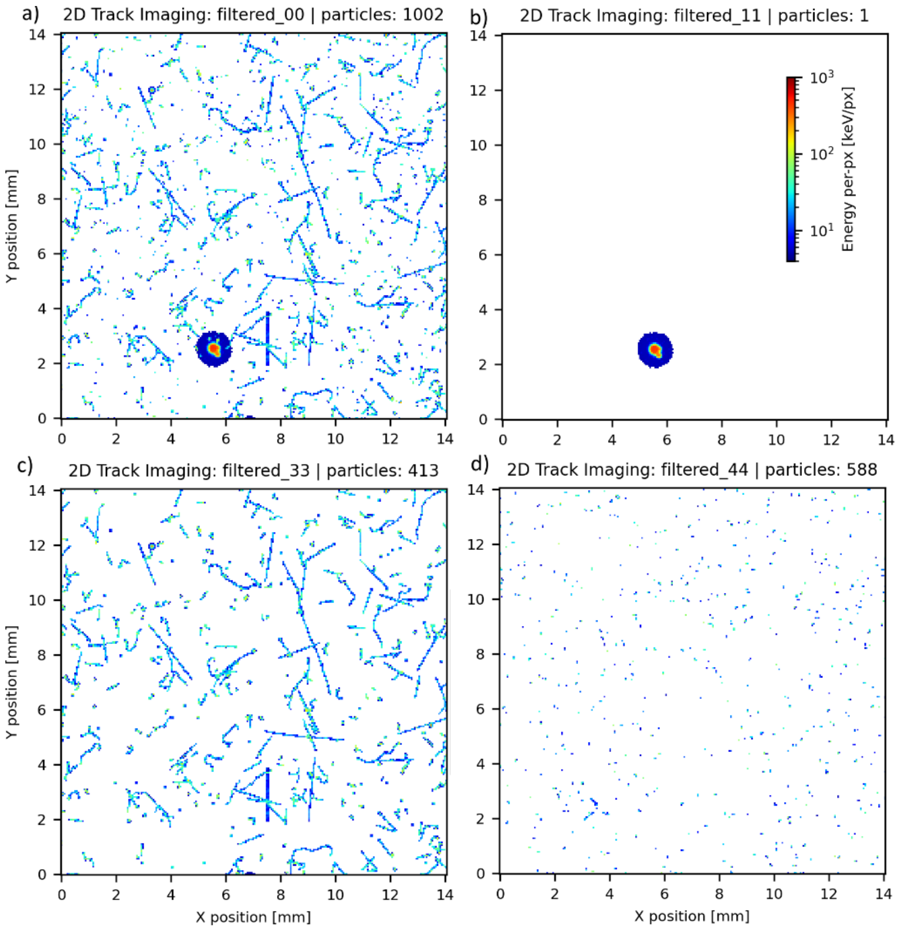

Figure 3.42: *Spectral and composition characterization of the SCR field at Lindenberg, DWD: (a) all particles – which are decomposed into broad-type classes: (b) high-energy transfer particles, (c) low-energy transfer particles, high-energy electrons and low-energy gamma rays, (d) X rays and low-energy electrons. Data acquired by the bottom TPX3 tracker 1000 um Si sensor during 52 minutes on 13 May 2025 at Lindenberg.*

Figure 3.43 shows the hourly averaged muon count rate together with surface pressure and temperature for the period from February to April 2025. The muon signal remained relatively stable, fluctuating between 9000 and 10200 counts per hour, but clear anti-correlation with atmospheric pressure is visible. Periods of high surface pressure correspond to reduced muon count rates, a well-known effect of the barometric response of cosmic ray muons, caused by the increased column density of the atmosphere (Savić *et al.*, 2021; Tirado-Bueno, Mendoza-Torres and de Mendonça, 2021; Taricco *et al.*, 2022). Seasonal warming from February to April is also evident in the temperature record, with the onset of more pronounced daily cycles in March and April, although no direct modulation of muons by temperature is apparent at the surface level.

The relationship between muon counts and surface pressure is highlighted in Figure 3.44, where the two time series are overlaid. The anti-correlation is clearly expressed, confirming the sensitivity of ground-based muon measurements to barometric variations. This allows for the determination of the barometric coefficient for the Lindenberg site, which is a key parameter for correcting SCR data and enabling inter-comparisons between different campaign locations.

Neutron measurements were also performed using UJF CAS liquid scintillator detector at DWD Lindenberg. The corrected fast neutron data in Figure 3.45 show stable background levels over the campaign period. The short gap in mid-April reflects a temporary interruption rather than a physical variation.

These observations confirm the robustness of the SCR measurements at DWD Lindenberg and highlight the importance of continuous atmospheric monitoring (pressure, temperature) for the interpretation and correction of cosmic-ray ground data.

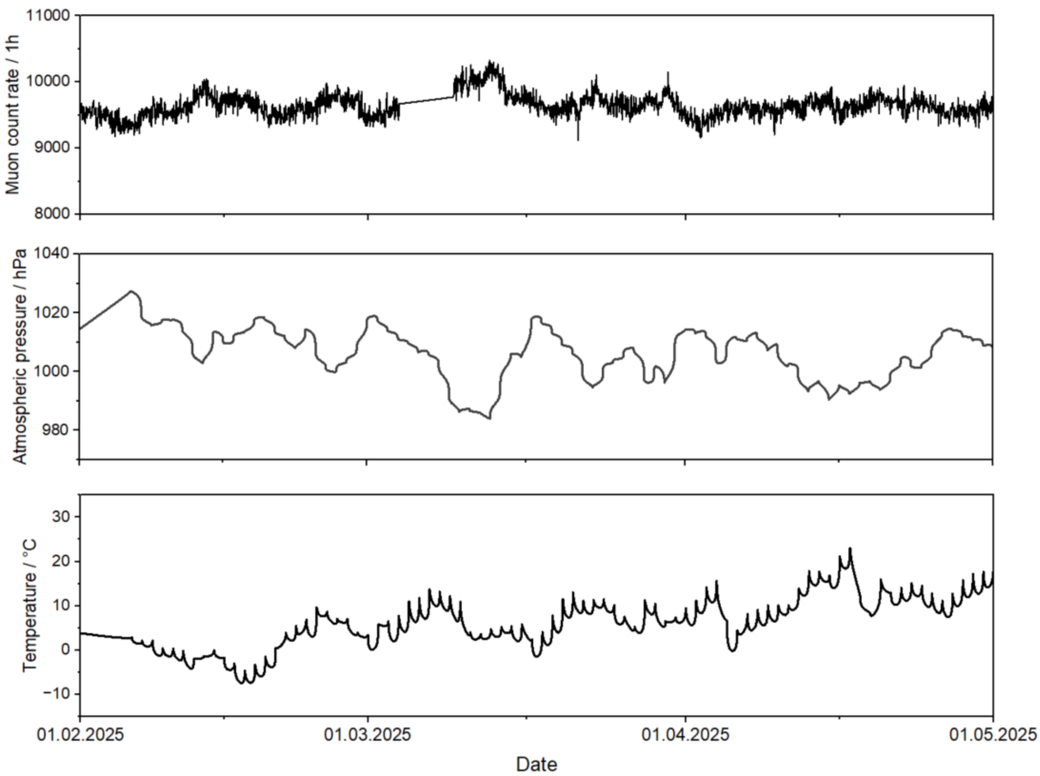

Figure 3.43: *Time series of muon count rate (top), surface pressure (middle), and temperature (bottom) measured at DWD Lindenberg during the campaign period (February–April 2025).*

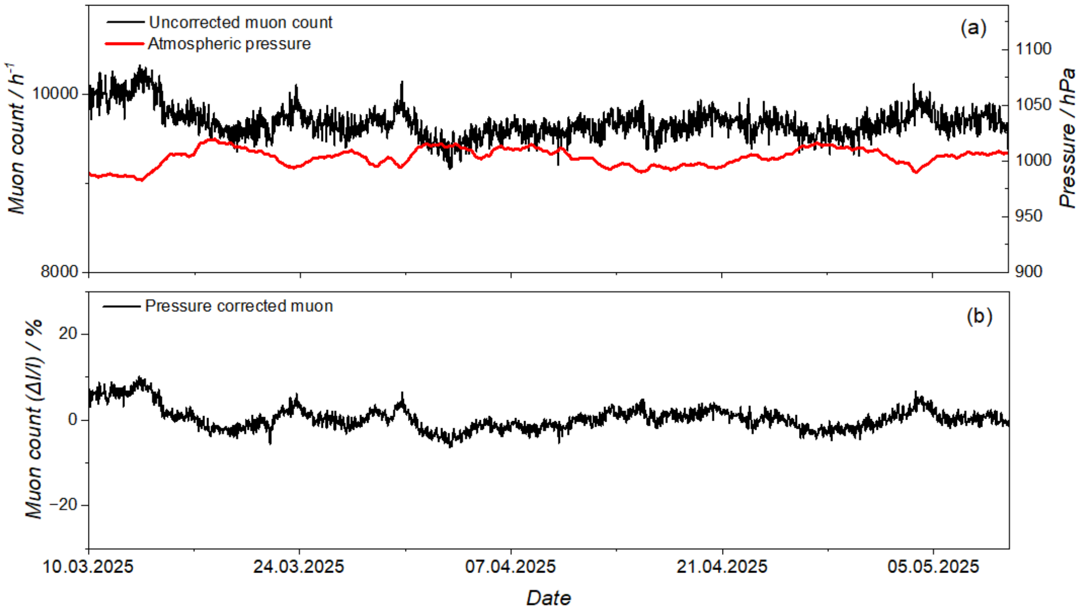

Figure 3.44: *Comparison of muon count rate (black) and atmospheric pressure (red) showing the clear anti-correlation characteristic of the barometric effect on cosmic-ray muons.*

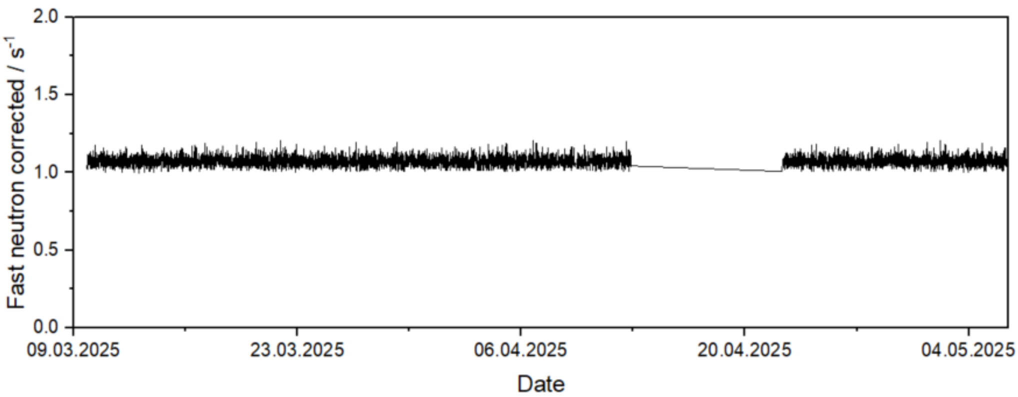

Figure 3.45: *Time series of pressure-corrected fast neutron counts* (UJF CAS liquid scintillator detector) *at DWD Lindenberg from 9 March to 5 May 2025.*

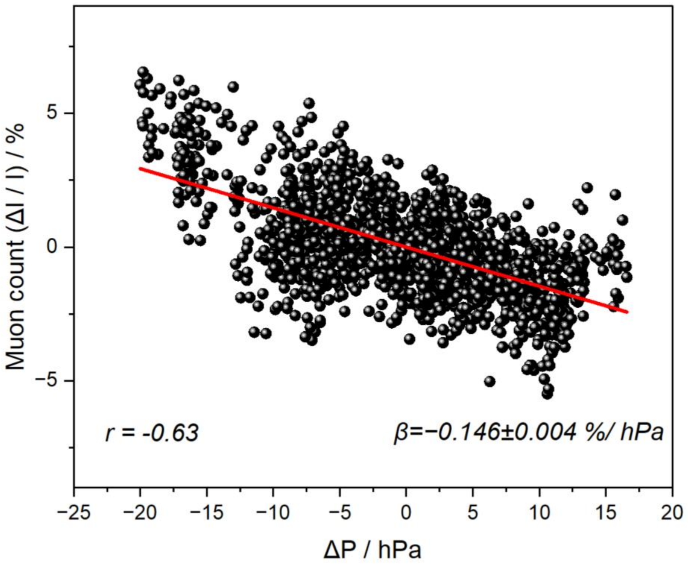

Figure 3.46: *Correlation between muon count rate variations and atmospheric pressure deviations during the campaign. A significant negative correlation is observed (r = –0.63), with a barometric coefficient of β = –0.146 ± 0.004 %/hPa.*

3.4.1 Observations of PROBA-V/EPT

During the DWD Lindenberg campaign (February – May 2025), particle flux measurements from the EPT provided valuable information on the variability of energetic electrons and protons in near-Earth space. The EPT instrument, operating on board the PROBA-V satellite, continuously monitors differential fluxes of charged particles across a broad energy range, thereby offering complementary data to ground-based cosmic-ray measurements.

Figure 3.47 shows the temporal evolution of differential electron fluxes in the energy range 0.5–2.5 MeV for six distinct energy channels during the DWD Lindenberg campaign. Overall, the electron fluxes remain relatively stable throughout the observation period, consistent with the fact that geomagnetic activity was not particularly intense. As a result, no major disturbances or large-scale variations in the electron radiation belts were observed. Nonetheless, minor fluctuations in several energy bands can still be seen, reflecting moderate magnetospheric dynamics and highlighting the importance of space-borne measurements for capturing even subtle particle precipitation events and their potential coupling to atmospheric processes.

Figure 3.48 presents the differential proton fluxes measured by PROBA-V/EPT in the energy range 9.5–155 MeV over the same campaign period. Overall, proton intensities remained low, with only a few short-lived enhancements observed. These enhancements likely correspond to SPEs or magnetospheric acceleration processes; however, none of the SPEs that occurred during this period penetrated deeply into the radiation belts — even the strongest event at the beginning of April. This indicates limited proton access to near-Earth space and suggests that their potential influence on atmospheric ionization and chemistry during this period was minimal. The EPT observations presented here provide essential context for interpreting ground-based cosmic-ray and UV radiation measurements. By combining space-borne particle flux data with surface observations, a more comprehensive understanding of the coupling between solar activity, magnetospheric particle dynamics, and atmospheric processes is achieved.

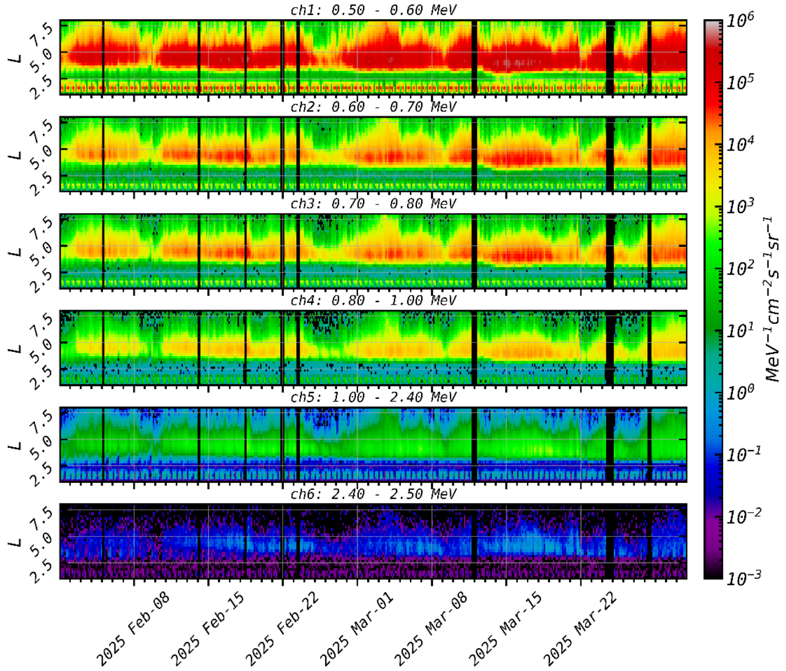

Figure 3.47: *Differential fluxes of energetic electrons (0.5–2.5 MeV) measured by PROBA-V/EPT during the DWD Lindenberg campaign (1 February – 1 May 2025). Enhancements correspond to variations in magnetospheric dynamics and electron precipitation.*

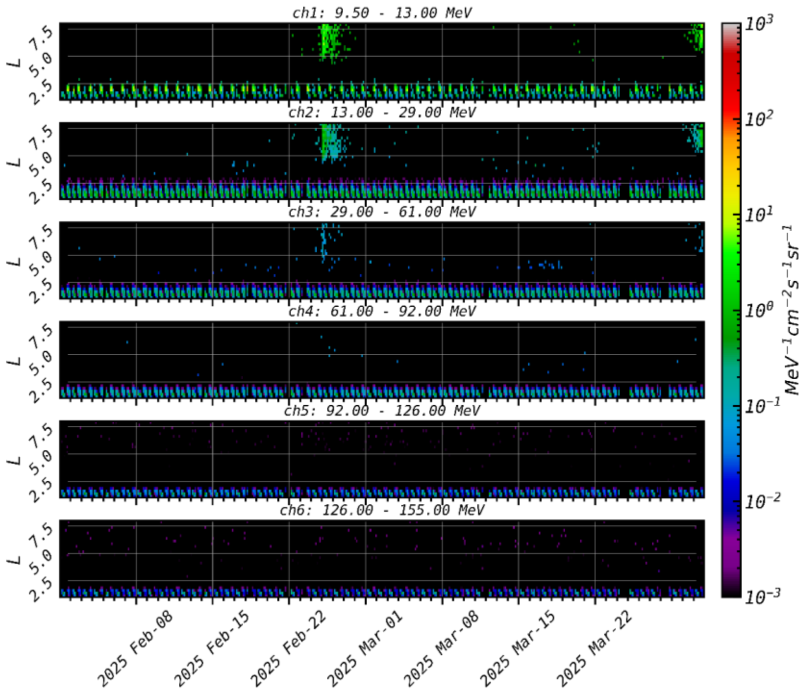

Figure 3.48: *Differential fluxes of energetic protons (9.5–155 MeV) measured by PROBA-V/EPT over the same period. Intermittent increases indicate possible solar particle events and magnetospheric acceleration episodes.*

3.4.2 Measurements of UV and TOC

During the DWD Lindenberg campaign, measurements of UV radiation, the TOC, and the total nitrogen dioxide column (TC-NO_2) were performed using the spectroradiometric suite installed at the Strahlungsmessplattform (radiation platform) and inside the SMZ building (Section 3.4). These included the DWD UV and TOC instruments, a BIRA-IASB Bentham spectroradiometer, and a GUV-511 multichannel radiometer. Together, these instruments provided high-quality data on both solar irradiance and key atmospheric trace gases.

Figure 3.49 summarizes the temporal evolution of TOC, and TC-NO_2 from February to May 2025. The TOC (top panel) varied between ~280 and 450 Dobson Units (DU), consistent with climatological values for Central Europe in late winter and spring. Occurrences of lower TOC, notably around late February and March, are associated with enhanced transmission of UVB radiation to the surface. Conversely, the partial recovery in April reflects the seasonal strengthening of the ozone layer in the Northern Hemisphere. The TC-NO_2 (bottom panel) remained generally low (<1 DU) throughout the campaign,

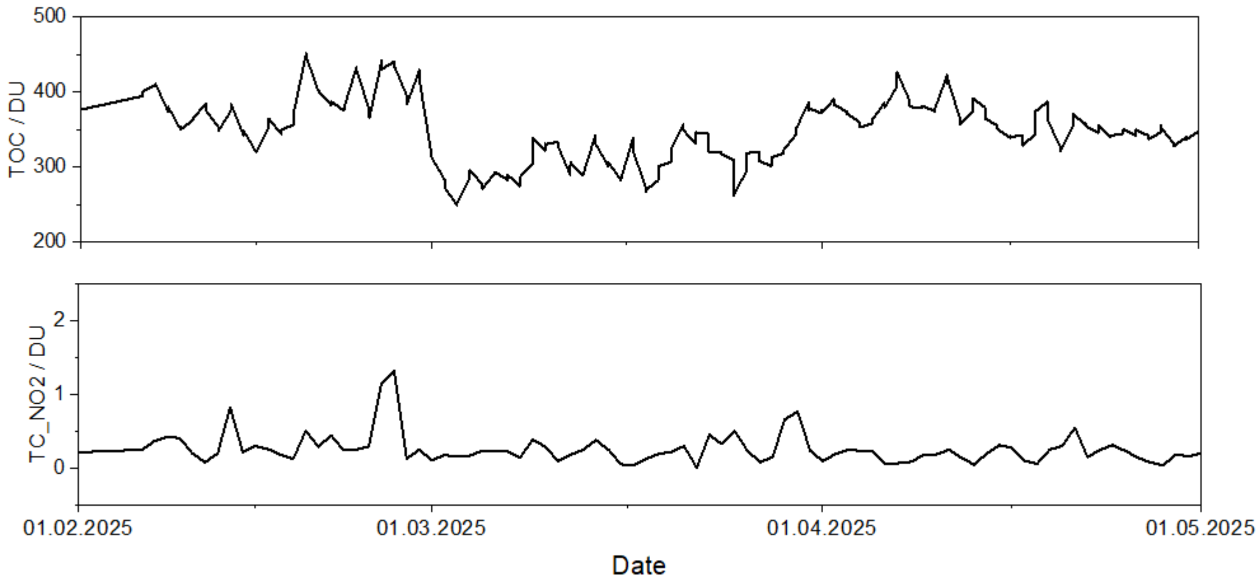

Figure 3.49: *Time series of total ozone column (TOC, middle), and total nitrogen dioxide column (TC-NO_2, bottom) measured at DWD Lindenberg during the campaign period (February–May 2025).*

We monitored TOC throughout the campaign using Brewer spectrophotometers (daily), a Dobson instrument (most working days), and BTS spectrometers in direct-sun mode at GHO and DWD (daily). The UV Index was measured with a UV pyranometer (BIRA-IASB), GUV radiometers (BIRA-IASB), Bentham spectroradiometers (from DWD and BIRA-IASB "Bent"), and BTS (DWD). The BTS served as the reference instrument, as it was included in all campaigns (except Brussels), enabling a quality assessment of the different systems presented below.

Quality study for UV instruments:

BTS (DWD), Bentham (BIRA-IASB) and Bentham (DWD) can be considered as reference instruments since there are verified well calibrated spectrometers. We will show there intercomparison to each other and discuss the pertinence of nominate them as reference instruments for the different campaigns: BTS (DWD) was reference in Athens, Milešovka and Lindenberg and Bentham (BIRA-IASB) was the reference in Brussels. Here in Lindenberg both referent instruments are present and can be compared to a third reference (Bentham

DWD). Moreover, we also verify if the UV-Pyranometer of BIRA-IASB is stable and precise enough to be considered as reference in Athens, when the BTS (DWD) needed to be put out of service for reparation.

1) Stability during the days of the campaign

The five graphs below (Figures 3.50 – 3. 54) show the relative difference (%) in UV Index between pairs of instruments (y-axis) as a function of campaign days (x-axis). Each point represents a comparison of individual measurements. The instrument pairs are considered in the following order:

- Bentham (BIRA-IASB) – BTS (DWD)
- Bentham (DWD) – BTS (DWD)
- Bentham (DWD) – Bentham (BIRA-IASB)
- UV-Pyranometer (BIRA-IASB) – BTS (DWD)
- UV-Pyranometer (BIRA-IASB) – Bentham (BIRA-IASB)

To quantify the differences, we calculated two statistical parameters over all comparison points of the campaign:

- MBE (Mean Bias Error, %), representing the systematic shift between instruments.
- STD (Standard Deviation, %), indicating the spread of the comparisons.

These statistical parameters are summarized in Table 3.1.

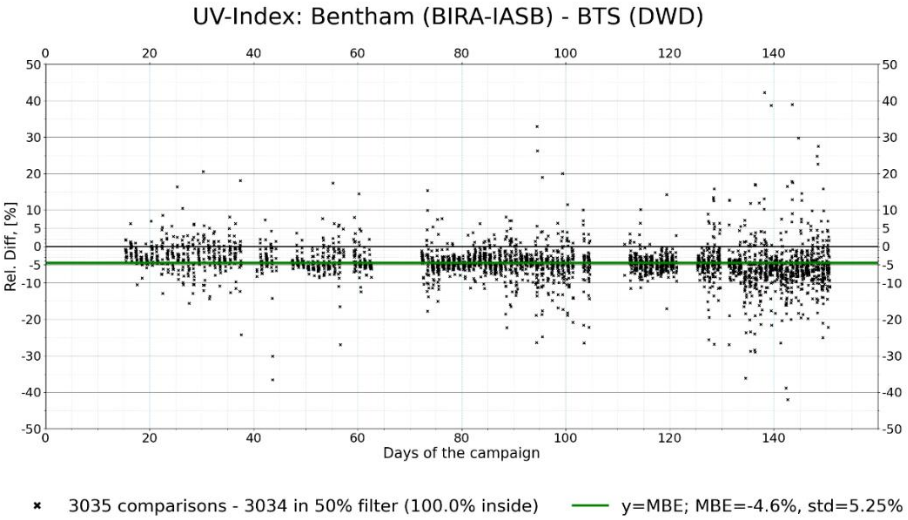

Figure 3.50: *Comparison of UV index measurements between the Bentham spectroradiometer (BIRA-IASB) and the BTS reference instrument (DWD) during the campaign*

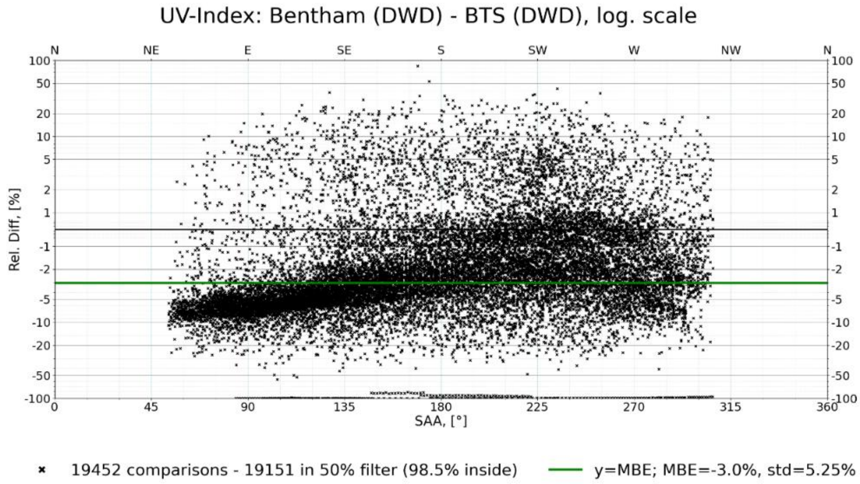

Figure 3.51: *Scatter plot of UV index comparison between the Bentham spectroradiometer (DWD) and the BTS reference instrument (DWD), in logarithmic scale.*

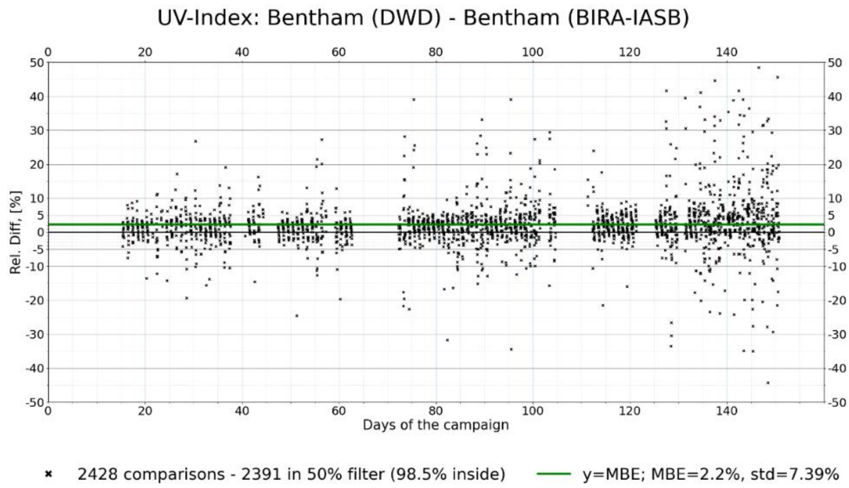

Figure 3.52: *Scatter plot of UV index comparison between the Bentham spectroradiometer (DWD) and the Bentham spectroradiometer (BIRA-IASB).*

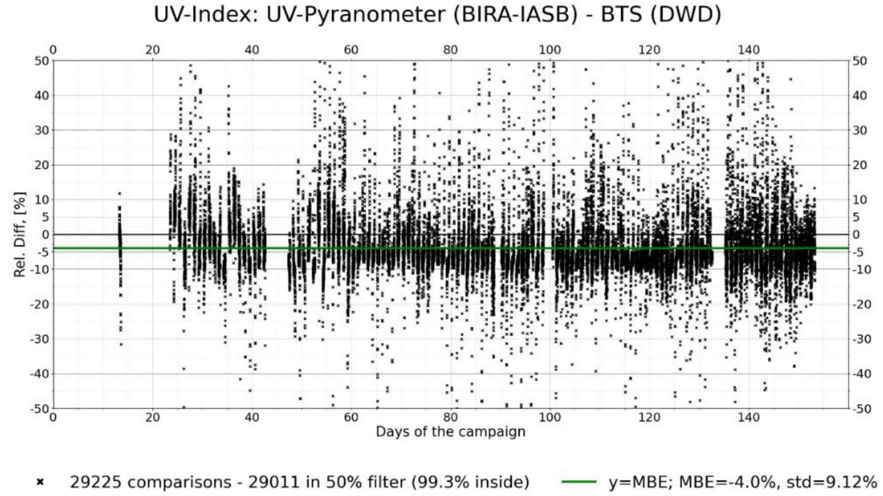

Figure 3.53: *Comparison of UV index measurements between the UV-Pyranometer (BIRA-IASB) and the BTS reference instrument (DWD) over the full campaign.*

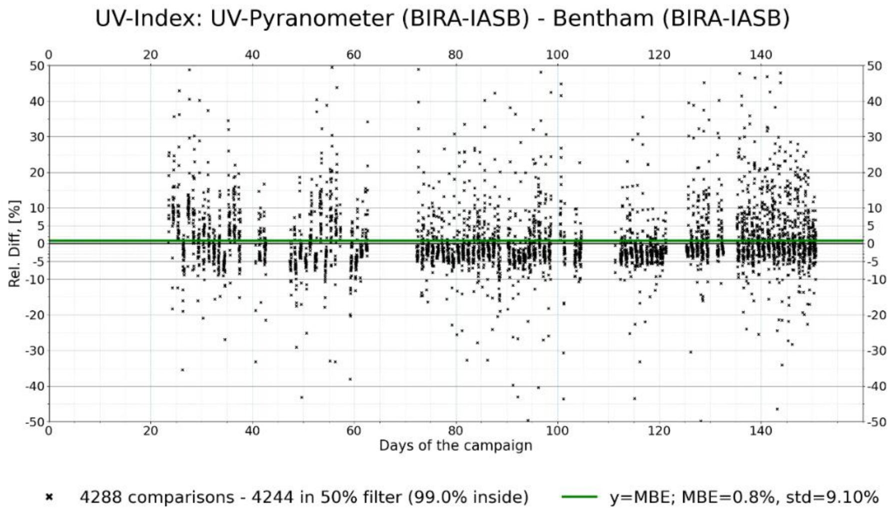

Figure 3.54: *Comparison of UV index measurements between the UV-Pyranometer (BIRA-IASB) and the Bentham reference instrument (BIRA-IASB) during the campaign.*

Table 3.1: *Statistical elements (MBE and STD) characterizing the difference between the two instruments of each pair.*

	MBE (%)	STD (%)
Bentham (BIRA) – BTS (DWD)	- 4.6 %	5.25 %
Bentham (DWD) – BTS (DWD)	- 3.0 %	5.25 %
Bentham (BIRA) – Bentham (BTS)	2.2 %	7.39 %
UV-Pyranometer (BIRA) – BTS (DWD)	-4.0 %	9.12 %
UV-Pyranometer (BIRA) – Bentham (BIRA)	0.8 %	9.10 %

The graphics show a good stability in terms of time (no slope during the days, no jumps). This is important, because even if the measurement of UV-Index is not exactly precise, the error should not change from day to day or time to time since we want to detect small variations of UV-Index due to PCR/SCR or SPE.

Table 1 shows a good agreement between reference instruments (the two Benthams and the BTS), with less than 5 % MBE and a standard deviation of about 5 % also. The larger STD for the Bentham comparison is due to the few points of comparison (STD decrease with the number of comparisons).

The bias of the UV-Pyranometer is moderate (MBE smaller than 5%), but the STD is large. The study below considering the solar angles give some explanation.

2) Study considering the solar angles

In this study, we analyze the relative differences between instruments as a function of the Sun Azimuth Angle (SAA). SAA ranges from 0–90° in the early morning (N–NE–E), 90–180° in the late morning (E–SE–S), 180° at solar noon (S), 180–270° in the early afternoon (S–SW–W), and 270–360° in the late afternoon/evening (W–NW–N). The Solar Zenith Angle (SZA) is defined as 90° minus the solar elevation, equal to 90° at sunrise and sunset, and minimal at solar noon. Color plots display relative differences as a function of SZA (radial axis) and SAA (angular axis), while conventional plots show relative differences (y-axis) versus SAA, with the daily evolution from morning to evening represented from left to right.

We retain the same order of figures as for the daily stability plots of the campaign:

- Bentham (BIRA-IASB) – BTS (DWD)
- Bentham (DWD) – BTS (DWD)
- Bentham (DWD) – Bentham (BIRA-IASB)
- UV-Pyranometer (BIRA-IASB) – BTS (DWD)
- UV-Pyranometer (BIRA-IASB) – Bentham (BIRA-IASB)

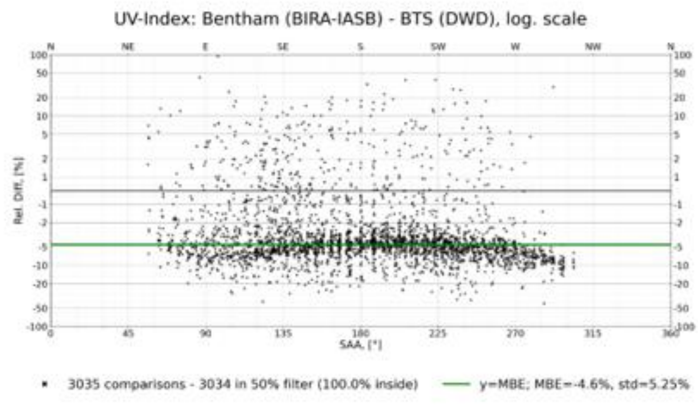

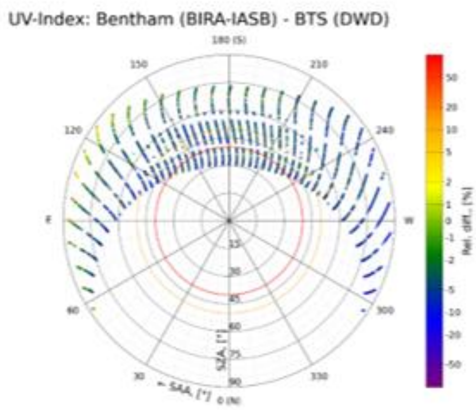

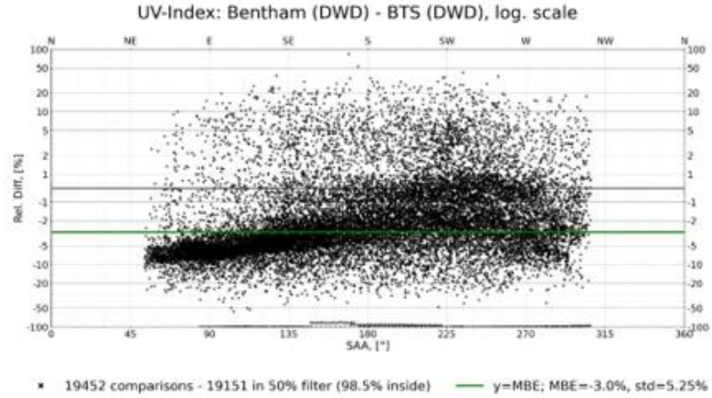
UV-Index: Bentham (DWD) - BTS (DWD), log. scale
Rel. Diff. [%]
SAA, [°]
19452 comparisons - 19151 in 50% filter (98.5% inside)
y=MBE; MBE=-3.0%, std=5.25%

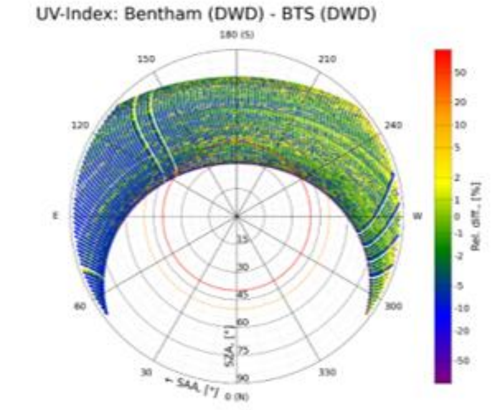
UV-Index: Bentham (DWD) - BTS (DWD)
Rel. diff., [%]
SZA, [°]
SAA, [°]

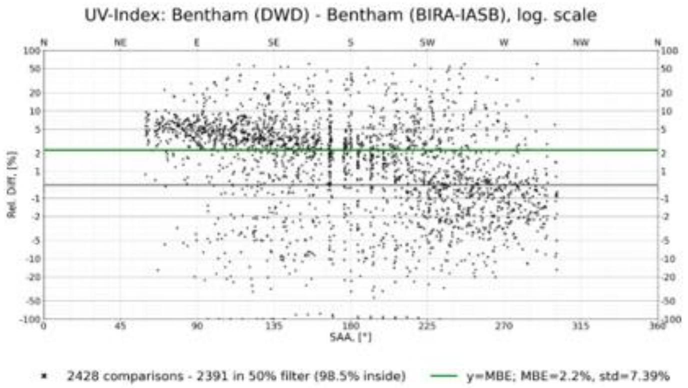
UV-Index: Bentham (DWD) - Bentham (BIRA-IASB), log. scale
Rel. Diff. [%]
SAA, [°]
2428 comparisons - 2391 in 50% filter (98.5% inside)
y=MBE; MBE=2.2%, std=7.39%

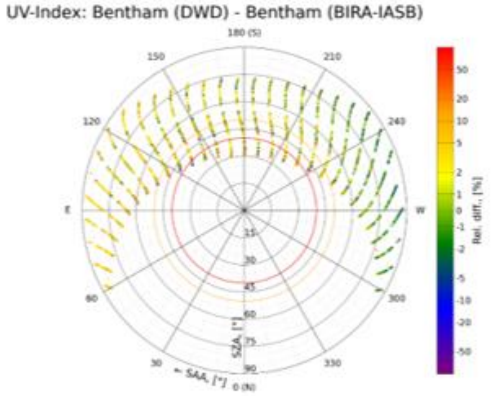
UV-Index: Bentham (DWD) - Bentham (BIRA-IASB)
Rel. diff., [%]
SZA, [°]
SAA, [°]

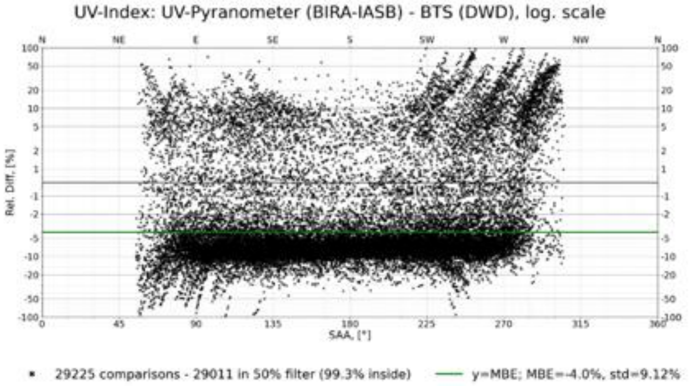
UV-Index: UV-Pyranometer (BIRA-IASB) - BTS (DWD), log. scale
Rel. Diff. [%]
SAA, [°]
29225 comparisons - 29011 in 50% filter (99.3% inside)
y=MBE; MBE=-4.0%, std=9.12%

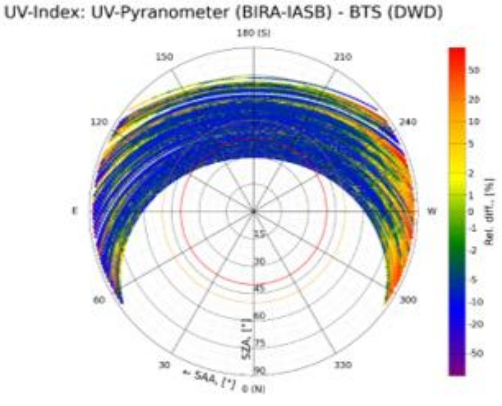
UV-Index: UV-Pyranometer (BIRA-IASB) - BTS (DWD)
Rel. diff., [%]
SZA, [°]
SAA, [°]

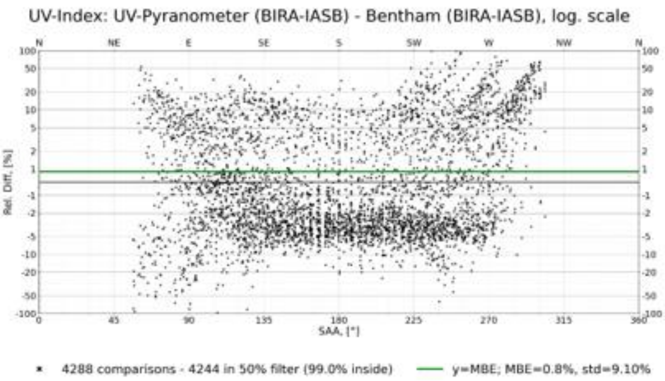

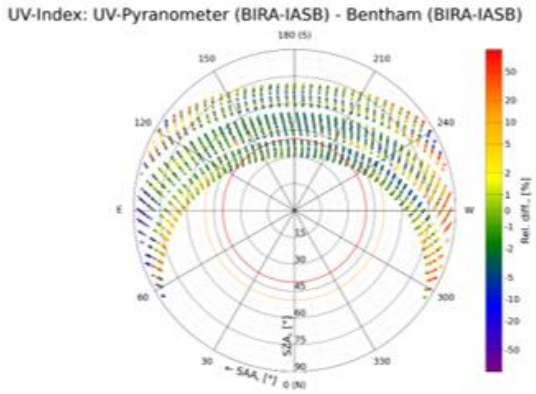

Based on the results, no dependence on solar angles is observed in the differences between the two main campaign references (Bentham BIRA and BTS DWD), implying no time-of-day dependence.

A slight decreasing trend with SAA appears in Bentham (DWD) – Bentham (BIRA), likely an artefact related to timestamp definition, since monochromators record spectra sequentially rather than instantaneously (unlike pyranometers or array spectrometers such as the BTS).

The Bentham (DWD) – BTS (DWD) plot versus SAA is somewhat surprising, possibly also linked to timestamping in the DWD Bentham UV Index measurements. However, the statistical results (e.g., STD) are better than the apparent spread suggests.

The UV pyranometer shows large scatter, particularly at high air mass (low sun: very small or very large SAA, SZA ~90° at sunrise and sunset). During the rest of the day, its agreement with the reference instruments is good.

4 Main Solar Particle events observed

One of the most important sources of short-term variability in the atmosphere and the near-Earth space environment is solar particle events (SPEs). They are linked to coronal mass ejections (CMEs) and solar flares, which have the ability to accelerate protons and heavier ions to energies high enough to enter the atmosphere and magnetosphere deeply (Trottet *et al.*, 2015; Papaioannou *et al.*, 2016; Maurchev *et al.*, 2024). Within the BIOSPHERE project, three field campaigns coincided with periods of enhanced solar activity, allowing a detailed investigation of how SPEs, geomagnetic storms, and associated phenomena such as Forbush decreases were reflected in the ground-based measurements of secondary cosmic rays (SCR), ultraviolet radiation, and total ozone column (TOC). The following subsections summarize the major events observed during the Brussels, Milešovka and DWD Lindenberg campaigns.

During the Brussels Campaign

The Brussels campaign, conducted between January and March 2024, took place during an exceptionally active phase of the solar cycle. During this period, several solar energetic particle events and geomagnetic storms were recorded, which were well captured by both satellite and ground-based instruments. GOES spacecraft data indicated multiple SEP events exceeding the classical threshold of >10 MeV protons with intensities greater than 10 particles $cm^{-2}\ s^{-1}\ sr^{-1}$ (Pierrard *et al.*, 2025). In total, seven SEP events were observed during the campaign period, with the most significant occurring on 24 March 2024. This event was accompanied by a strong geomagnetic storm (Dst ≈ −125 nT, Kp = 8), as illustrated in Figure 4.1, which ranks among the most intense disturbances of solar cycle 25 up to that point. The 24 March event was characterized by a sudden increase in high-energy proton flux, a simultaneous depression of the geomagnetic field, and pronounced effects on the radiation belts. Measurements from the Energetic Particle Telescope (EPT) on board the PROBA-V satellite showed electron dropouts in the outer belt, followed by subsequent injections of relativistic electrons, a behavior typical of strong geomagnetic storms as showed in section 3.2.2, Figure 3.21 and 3.22 for proton and electron respectively.

OMNI2_H0_MRG1HR

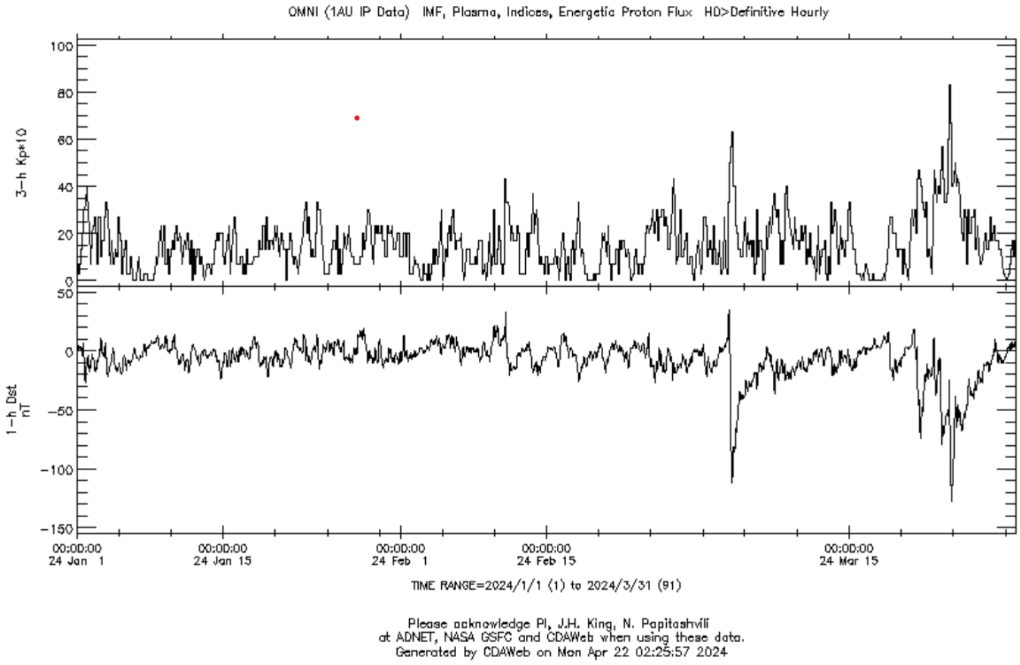

Figure 4.1: *Observations from 1 January 2024 to 31 March 2024. Disturbed Storm Time Dst and Bartels Kp geomagnetic activity indices,*

At ground level, neutron monitors and muon detectors in Brussels and Dourbes recorded clear Forbush decreases. Muon counts which measured by PTB-DECOS2 detector decreased by approximately 7%, while neutron monitors showed a stronger response of about 10%, consistent with their greater sensitivity to lower-energy primary cosmic rays as we can see in Figure 4.2 respectively.

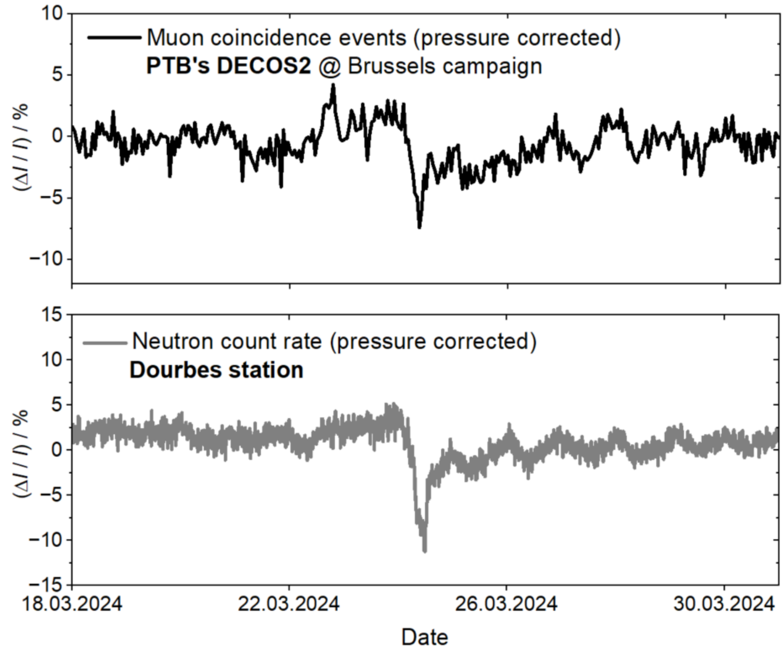

Figure 4.2: *Pressure-corrected and normalized c) muon coincidences (1 h averages) and d) neutron count rates showing the FD event on 24 March 2024.*

Satellite observations of the atmosphere further revealed changes linked to these events. Aura/MLS ozone profiles showed significant depletion in the mesosphere during SEP events, particularly at altitudes around 90 km (see Figure 4.3). These ozone losses are attributed to the enhanced ionization and subsequent catalytic cycles involving odd hydrogen and odd nitrogen produced by energetic particle precipitation. The 24 March event, therefore, provided a clear example of how solar particle events can influence both the upper atmosphere and surface-level parameters relevant for human exposure.

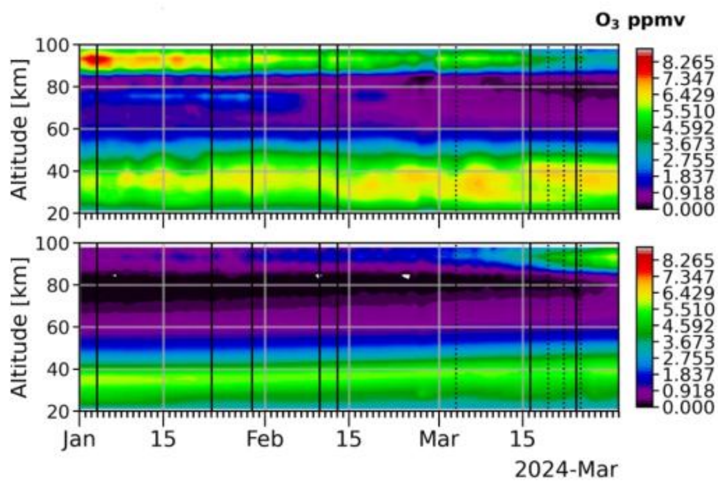

Figure 4.3: *In the North hemisphere (top panel), and in the South hemisphere (bottom panel), concentration of ozone in part per million by volume (ppmv) as observed by MLS/Aura as a function of the altitude from 20 km to 100 km*

Although the official campaign concluded in March, it is worth noting that the subsequent Mother's Day superstorm of 10–11 May 2024, the strongest geomagnetic storm in two decades, provided additional insight into the impacts of extreme solar events. Data from Brussels monitoring stations recorded an even more pronounced Forbush decrease, along with large short-term variability in TOC and UV radiation. These results serve as a benchmark for understanding the atmospheric implications of extreme space weather, and more details for the Mother's Day superstorm are presented by Pierrard *et al.*, 2025.

During the Milešovka Observatory Campaign

Several geomagnetic events were detected during the 3rd measurement campaign at the Milešovka Observatory. In particular, two consecutive geomagnetic storms took place on October 8 and October 11**,** 2024, as indicated by sharp variations in the geomagnetic indices (Kp and Dst; Figure 4.4). These disturbances were associated with enhanced solar wind activity and proton fluxes, which reached elevated levels in the days following the storms (Figure 4.5).

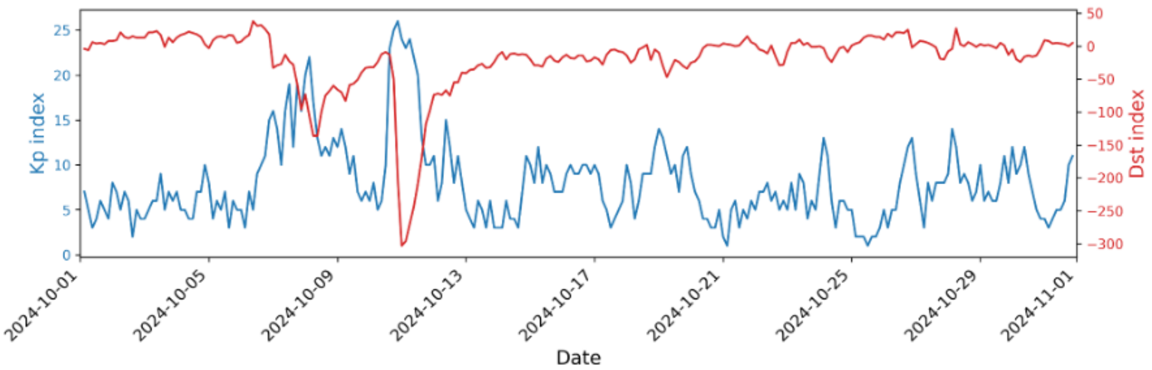

Figure 4.4: *Time series of geomagnetic indices during October 2024, showing the Kp index (blue) and Dst index (red).*

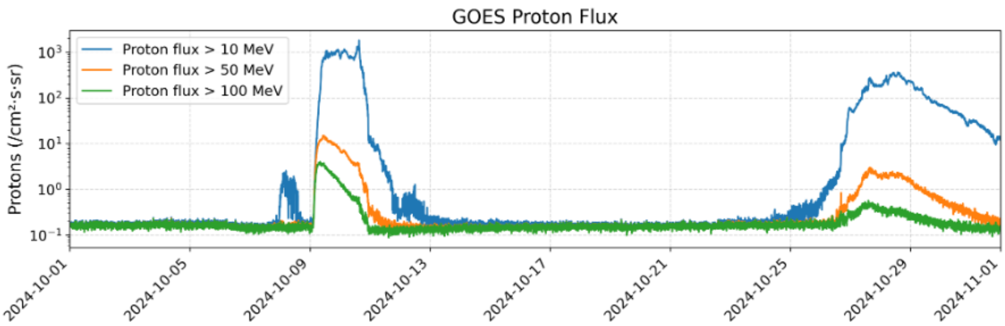

Figure 4.5: *GOES proton flux measurements (>10, >50, >100 MeV) from October 1 to November 1, 2024. Enhanced proton activity is observed during and after the geomagnetic disturbances.*

The impact of these events on secondary cosmic rays (SCR) was clearly observable. Neutron monitor data from Lomnický Štít showed marked Forbush decreases, with neutron flux reductions of up to 8% around October 11 (Figure 4.6, top). Also, the SEVAN neutron detector displayed similar temporal variations (Figure 4.6, bottom), consistent with the suppression of cosmic-ray intensity following the geomagnetic disturbances.

Furthermore, ground-based muon detectors also recorded corresponding decreases in intensity, both at SEVAN station and with PTB mobile detector (DECOS2), reflecting the modulation of galactic cosmic rays by the interplanetary disturbances (Figures 4.7). These coincident signatures across multiple SCR channels highlight the strong coupling between solar wind dynamics, geomagnetic activity, and secondary cosmic-ray fluxes during this campaign period.

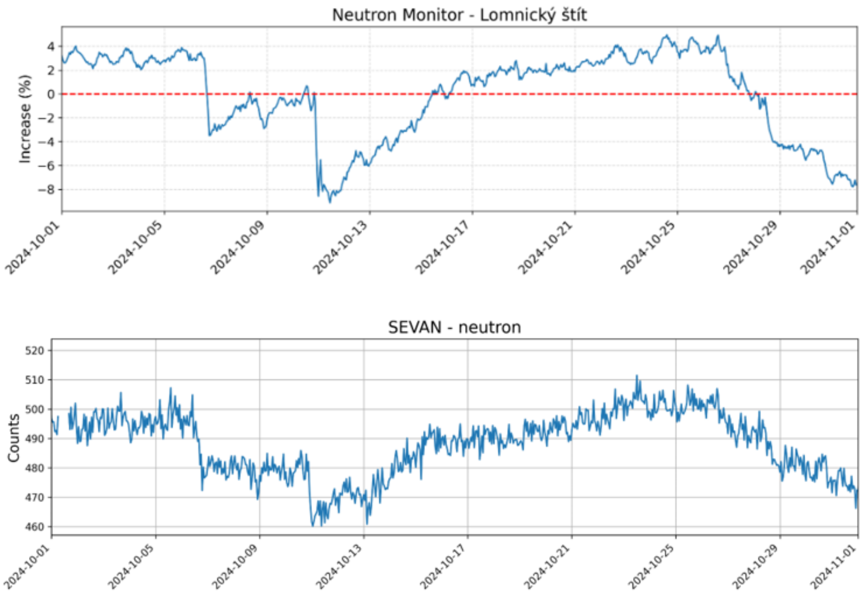

Figure 4.6: *(Top) Neutron monitor data from Lomnický Štít showing relative changes in neutron flux (%).. (Bottom) Neutron count rates measured by the SEVAN neutron detector during October 2024. Forbush decreases are evident around October 11and October 13.*

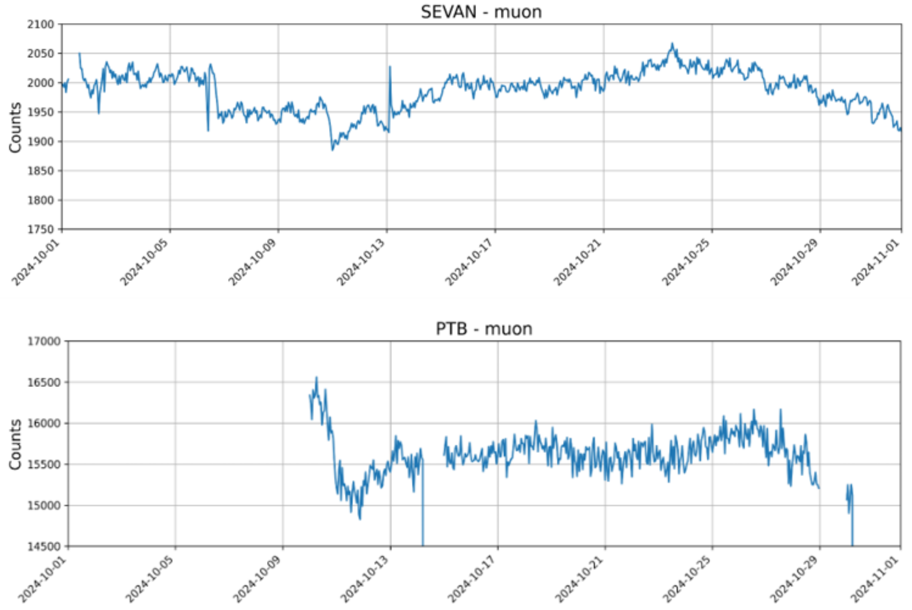

Figure 4.7: *Muon count rates measured by the SEVAN detector (Top). Muon count rates measured by the PTB detector (bottom). Both during October 2024.*

During the DWD Lindenberg Campaign

The third major opportunity to investigate solar particle events occurred during the DWD Lindenberg campaign, which extended from January to May 2025. Although solar activity during this period was not as extreme as in early 2024, several notable SPEs were detected, including events with proton fluxes exceeding the GOES threshold. Based on Figure 4.8, we can see that the period between January 1st and May 31th 2025 was relatively quiet in term of geomagnetic activity (top panel), Solar Proton Events (middle panel) and Forbush Decrease (bottom panel). However, during this period, one major event took place at the beginning of January. Around this time, both a very intense geomagnetic storm (Dstmin ~ -210 nT) was observed on Earth together with a Forbush Decrease which started in late December. A short amount of time later (January 6th), the first of the 3 major SPE event of the year took place. It was also accompanied by a moderate geomagnetic storm.

At the same time, daily ozone profiles from MLS/Aura instrument averaged over the northern polar hemisphere shows a decrease in the mesospheric concentrations (Figure 4.9). This decrease is likely caused by the solar protons, however the SPE was not extremely large, and we must check if other factors from the atmosphere could explain this drop in O3 concentration.

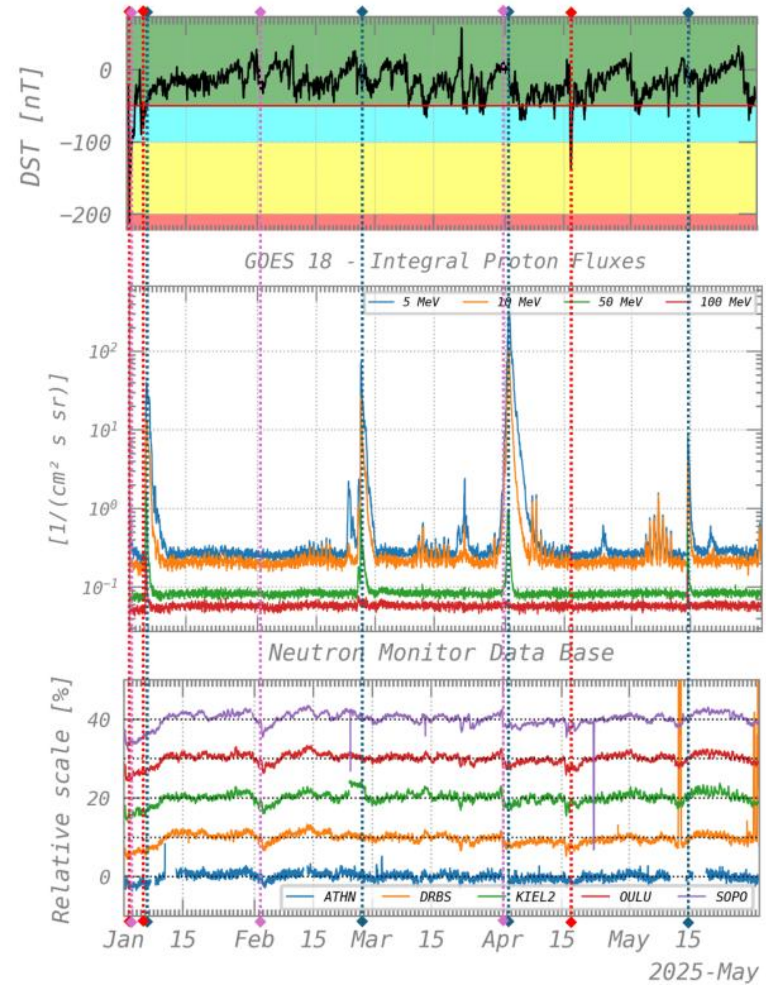

Figure 4.8: *Top: Disturbed storm time. Middle: Proton integral flux measured by GOES 18. Bottom: Relative counts of neutrons from the neutron monitor database.*

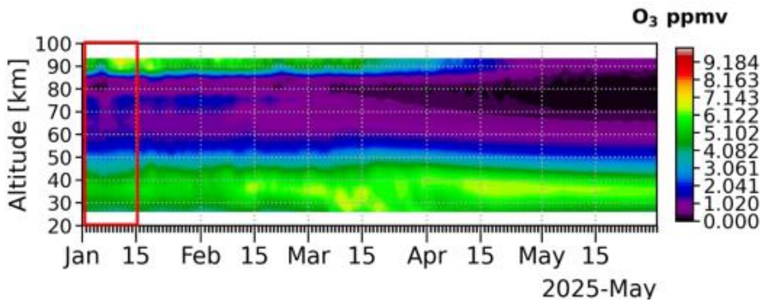

Figure 4.9: *Daily averaged ozone concentration computed from MLS/Aura observations as a function of time and altitudes in the northern polar hemisphere ([60°, 82°]).*

At Lindenberg, the mobile muon detector from PTB recorded characteristic weak Forbush decreases 1-4th of April 2025. The amplitude of these decreases was smaller than that observed in Brussels in March 2024, typically on the order of 2–5%, as illustrated in Figure 4.10. The SCR observations at Lindenberg therefore confirmed the consistency of cosmic ray modulation across different European sites.
The particle flux observations during the DWD campaign highlight the presence of both electron and proton enhancements linked to solar activity in January-May 2025 are presented in section 3.4.1, Figures 3.47 and 3.48. The DWD Lindenberg campaign thus provided a third case study, confirming and extending the findings from Brussels and Milesovka.

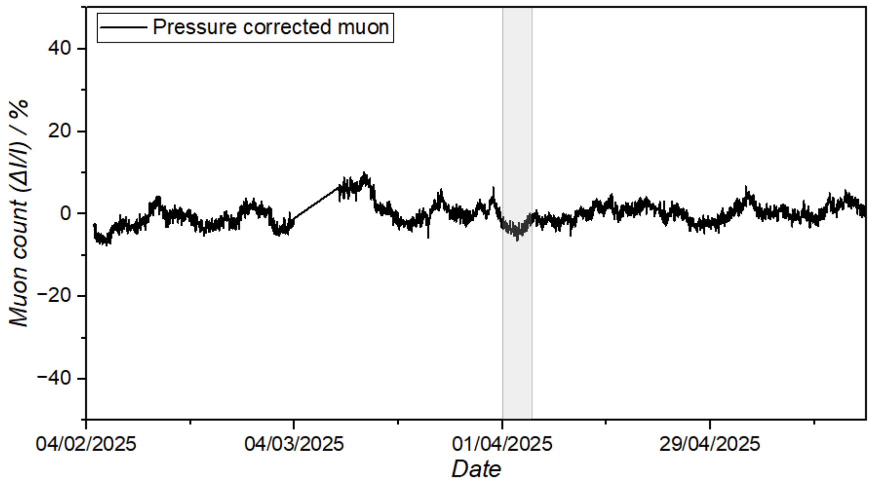

Figure 4.10: *Relative-scale pressure-corrected muon count rates from the DECOS2 detector at DWD Lindenberg during March–April. The highlighted regions indicate Forbush decreases observed between 1–4 April 2025.*

5 Quantifying Links Between Cosmic Ray Activity, Ozone, and UV Radiation

The interaction between solar radiation, atmospheric composition, and cosmic ray activity is important and plays a key role in determining the variability of surface-level UV radiation (Gray *et al.*, 2010; Georgieva and Veretenenko, 2023). In this section, we investigate the relationships between the UV index, the total ozone column, solar particle events and secondary cosmic rays (muons).

Correlation Between UV Index, Total Ozone Column, and Solar Particle Events

The solar UV irradiance at ground level is influenced by several geometrical, chemical and atmospheric parameters. The primary modulation is due to the elevation of the Sun, which depends on the time of the day, the time of the year and the site location. For a given date and location, the UV index follows a daily profile with a maximum at true solar noon under clear sky conditions. The second key factor is the cloudiness, which generally reduces the UV index with respect to clear sky days due to cloud optical depth. However, under broken cloud fields with unobstructed direct sunlight, bright cumulus may temporarily enhance the UV index by reflecting UV rays. To a lesser extent, aerosols reduce the UV Index by scattering and absorbing UV radiation. The exact effect depends on aerosol properties, such as the size, type, and optical depth (AOD). UV index amount can be reduced from 5 to 35 %. In addition, other factors such as the altitude and albedo have a contribution on the UV index. For example, the campaign in Brussels started in winter and ended in spring. At Uccle, the presence of snow and modifications of the grass cover could slightly affect the site ‘s average albedo. Finally, there is a well-defined anticorrelation between TOC (mainly from the stratospheric layer) and the UV index (Kerr and McElroy, 1993; Bernhard *et al.*, 2023). The higher the ozone, the lower the UVB radiation. This anticorrelation is well observed when looking to data of clear sky days for a fixed SZA.

The influence of TOC on the UV-Index is larger than the aerosol influence but smaller than the cloud and sun elevation influence. For clear sky (cloudless) days, regarding the UV-index at the same sun zenith angle, TOC is the main parameter of influence (see graphics of Figure 5.1).
As we can see the campaign results from Athens, Brussels, Milešovka, and DWD Lindenberg show a clear negative correlation between the UV index and TOC under clear sky conditions at fixed solar zenith angle (75°) as illustrated in Figure 5.1.
Over Brussels, variations in TOC were also evident during the campaign period. The linear correlation between the daily average TOC and the daily maximum UV Index was weak and not statistically significant during the first part of the period (2 January–15 March 2024, r = 0.0024). In contrast, a statistically significant negative correlation was found in the later period (16 March–31 May 2024, r = −0.39), indicating that episodes of reduced TOC coincided with elevated UV Index values (Pierrard et al., 2025).

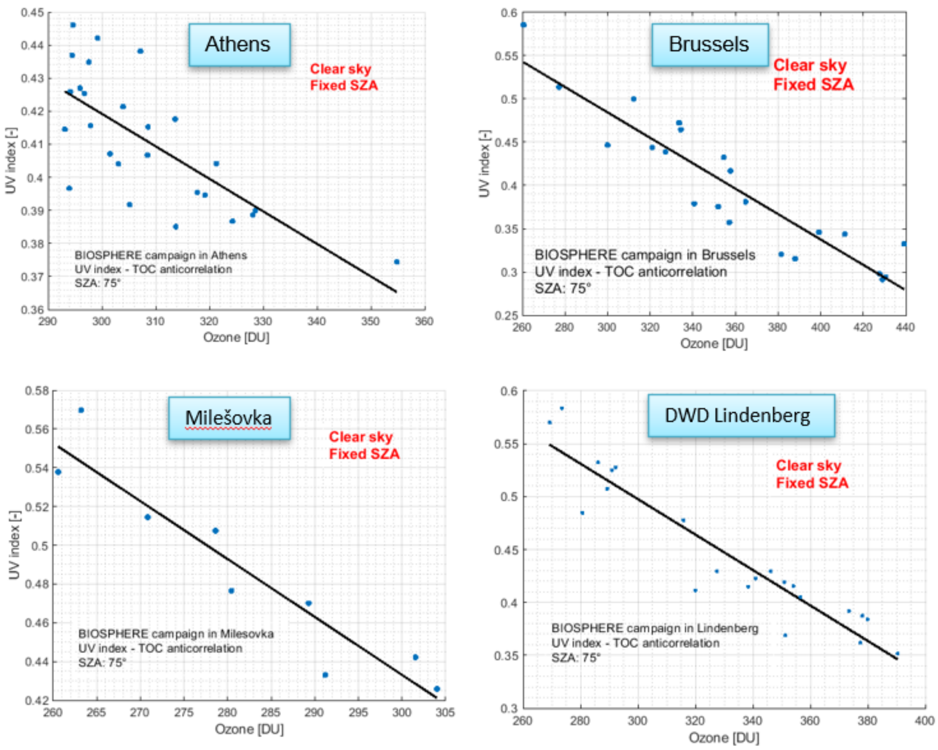

Figure 5.1: *Correlation between UV index and total ozone column (TOC) at Athens, Brussels, Milešovka, and Lindenberg during the BIOSPHERE campaigns. All sites show a clear anticorrelation under clear sky and fixed SZA (75°) conditions.*

The ideal conditions to detect UV index anomaly induced by a SPE (Solar Particle Event), which affects the ozone layer due to an increase of atmospheric ionization) would be clear sky days, constant albedo and aerosols conditions. These conditions were nearly encountered during the Mother‘s day event on May 11, 2024, the most intense event in the past 20 years. A correlation between ozone depletion in the mesosphere and SPE was observed and confirmed during the 21GRD02 BIOSPHERE campaigns (Winant et al. 2025). However, there is less evidence of depletion of the stratospheric ozone layer. During the Mother‘s day storm, the UV index increased around May 11, correlating with a decrease in TOC on the same period (Figure 5.2). After fine analysis, it appears that the sudden TOC variation was mostly influenced by the horizontal displacement of the Artic polar vortex and related atmospheric circulation patterns, which is understood as the dominant source of TOC variation. Additional research could be conducted to determine if TOC depletion could be deepened by the SPE.

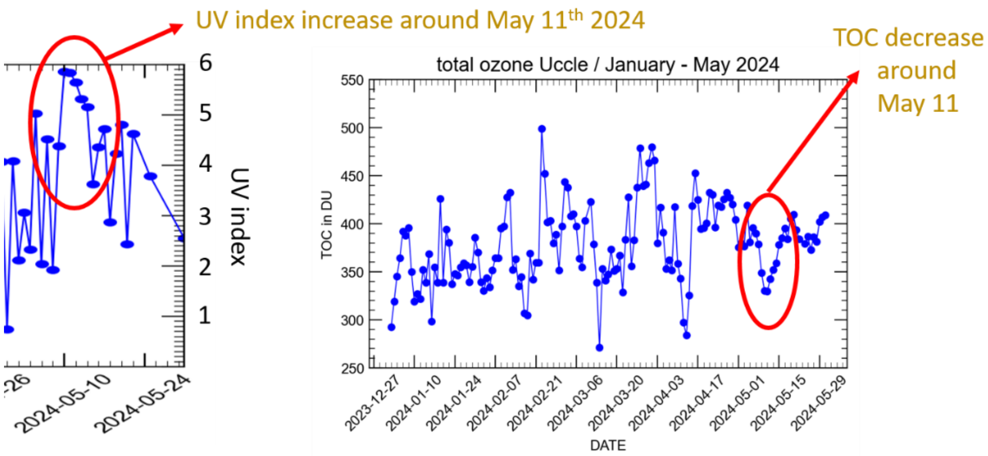

Figure 5.2: *TOC and UV index monitoring during the Brussels campaign. A UV index increase correlated to a TOC depletion was observed around the key days of the Mother’s day event in May 2024, highlighted in red.*

However, it seems confirmed from EPT data that energetic solar protons were only precipitated at high latitude, while the sites of the four BIOSPHERE campaigns are installed at mid-latitudes (see Figure 5.3). This could also explain the limited impact on stratospheric ozone observed during these campaigns.

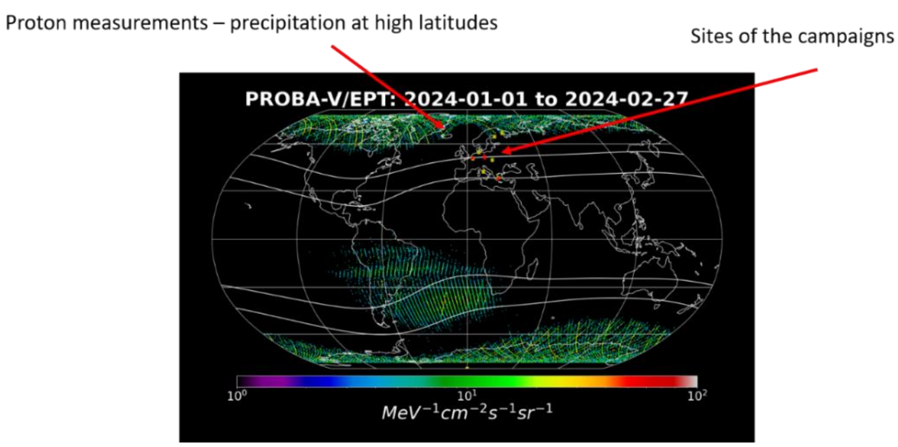

Figure 5.3: *Typical mapping of proton precipitation as measured by EPT (here in January and February 2024). The high latitudes are more affected than mid-latitudes where the sites of the campaigns are defined.*

The Carington event in 1859 was estimated to be at least 100 times more intense than the Mother‘s day storm, and an extended impact on the whole ozone vertical distribution (including the stratosphere) could be assumed. A continuous and very accurate monitoring of TOC and UV index using core and redundant instrumentation is therefore essential, not only to detect the changes of TOC and UV index in real time, but also to quantity them.

Correlation Between UV index, TOC and SCR

In this section, SCR, measured at ground level through muon detectors, are employed as scientifically recognized proxies for PCR variability. This approach is widely established in atmospheric and space physics, as SCR fluxes reflect changes in the primary galactic cosmic ray intensity modulated by solar activity and geomagnetic conditions, which cannot be directly measured at the Earth’s surface (Dorman, 2004; Grieder, 2010; Asvestari et al., 2017).

The relationship between pressure-corrected muon counts (as SCR), UV Index, and total ozone column was analyzed for the Brussels and Lindenberg campaigns under clear sky conditions at fixed solar zenith angle (SZA = 75°). As shown in Figure 5.4, no significant correlation is observed between SCR variations and either UV Index or TOC. The regression slopes remain essentially flat, and fluctuations are within statistical noise.

This result indicates that, at mid-latitudes, natural TOC variability (10–30 DU over a few weeks) dominates over any potential influence of cosmic rays. Such ozone changes are an order of magnitude larger than any depletion expected from solar or galactic cosmic ray interactions. This conclusion is consistent also with recent results from the BIOSPHERE project (Winant et al., 2025), which reported that even during the extreme May 11th 2024 solar storm, ozone depletion was restricted to the mesosphere and lower thermosphere, with no significant impact on the stratosphere. From the top panel of Figure 5.5, it is obvious that some ozone was lost during the period of interest. The vertical black dotted line indicates the day during which the daily averaged proton flux and geomagnetic activity are the highest (i.e. May 11th). The main ozone loss was observed after the event in the tertiary layer at around 75 km.

Thus, our findings confirm that SCR (muon) fluctuations during the campaigns had no measurable impact on TOC or UV Index, supporting the conclusion that short-term UV variability is controlled primarily by ozone, solar zenith angle, and clouds, rather than cosmic ray forcing.

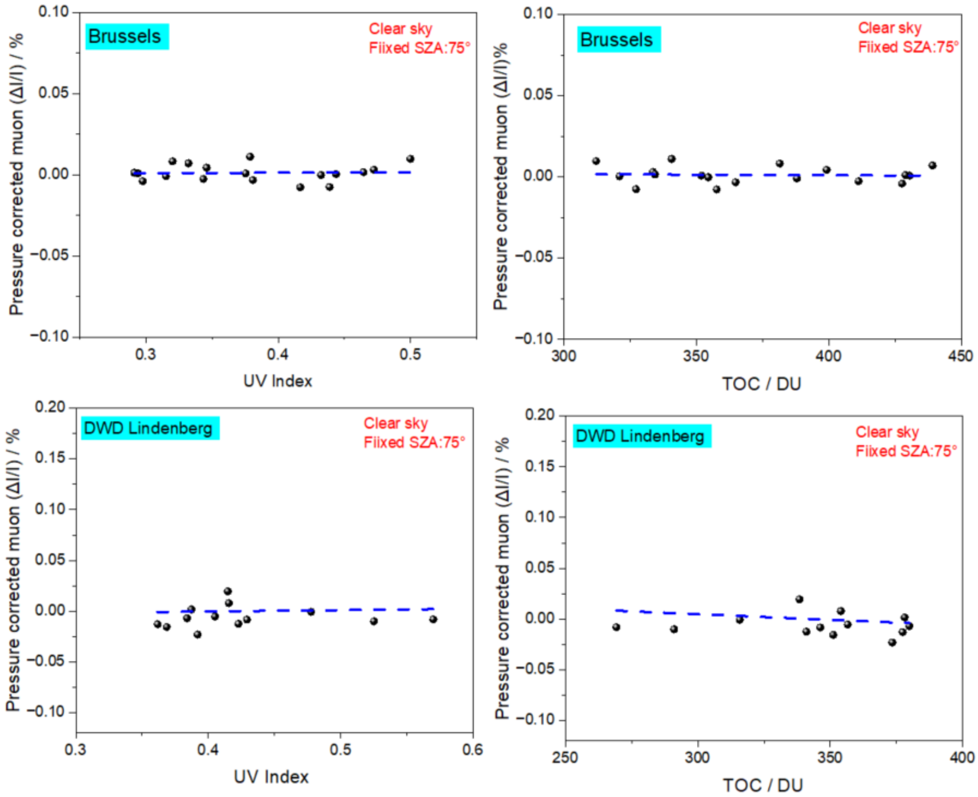

Figure 5.4: *Scatter plots of pressure-corrected muon counts versus UV Index (left) and TOC (right) for Brussels (top row) and Lindenberg (bottom row) campaigns at SZA = 75°.*

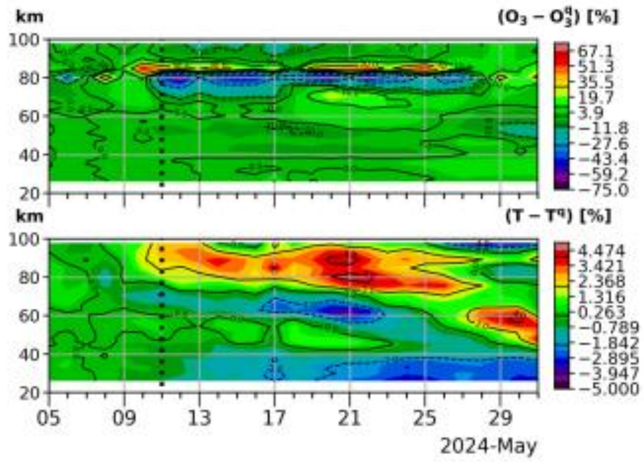

Figure 5.5: *Top panel: Relative difference in [%] between the mean quiet condition ozone profiles (O_3^q) and the daily ozone profiles from AURA/MLS, during the whole period between May 05 and May 30 (O^3). Bottom: same for temperature profiles. The vertical black line displays the day when the daily Dst index reached its minimal value, indicating the end of the main phase of the geomagnetic storm on May 11 also corresponding to the peak proton flux for the event* (Winant et al., 2025).

6 Penetration of V(UV) radiation though anthropogenic gas columns: laboratory studies

Solar particle events in the atmosphere can trigger various chemical reactions those in a combination with known photo-chemical processes can lead to a formation of reactive species above their typical background (so-called base line) levels. Thus, for example, SPE's in STRATOSPHERE can increase NO/NO_2 concentrations up to 5 times (compared to base line), while SPE's in MESOSPHERE can increase NO/NO_2 concentrations to much higher level: by 10 to 1000 times (compared to base line).

The purpose of this section was to investigate penetration of the (V)UV-VIS radiation through a gas column which consists of a mixture of the main anthropogenic gases such as CO2, CH4, N2O, O2 and NOx (NO+NO2) at variable NOx concentrations. This will simulate situation when NOx is formed in SPE's.

Experimental setup

Measurements of (V)UV-VIS absorption (optical depth, OD) at variable NO/NO_2 concentrations have been made at laboratory conditions. Three different spectrometers and three light sources have been used to cover 157-650 nm spectral range which is accessible at typical stratosphere-mesosphere conditions. The measurements have been done in a 50 cm gas cell between around 1 bar and 40 bar to cover full range of optical depths typical for stratosphere and mesosphere.

A synthetic gas mixture of CO_2 (13922ppm) + CH_4 (64ppm) + N_2O (11ppm) + O_2 (20.99%) in N_2 balance gas (Air Liquid, gas cylinder A) was used to mimic typical *relative* anthropogenic gas concentrations in stratosphere and mesosphere. In addition to that, a NO (867ppm) + NO_2 (210ppm) in N_2 balance gas (Air Liquid, gas cylinder B) gas mixture was used to generate A + B mixture by mixing two gas flows controlled by two calibrated mass-flow controllers (MFC's). By adjusting A and B flows in respective MFC's, various concentrations of NO and NO2 in the A + B mixture were obtained.

The (V)UV-VIS absorption measurements have been performed at in-flow conditions in the gas cell (i.e. continuous gas flow through the gas cell during the measurements).

Penetration of V(UV) radiation in atmosphere and NO/NO_2 spectra

Penetration of V(UV) part of the solar radiation in the atmosphere depends on the height above the ground. A depth of penetration of solar radiation is shown in Figure 6.1. (Liou, 2002).

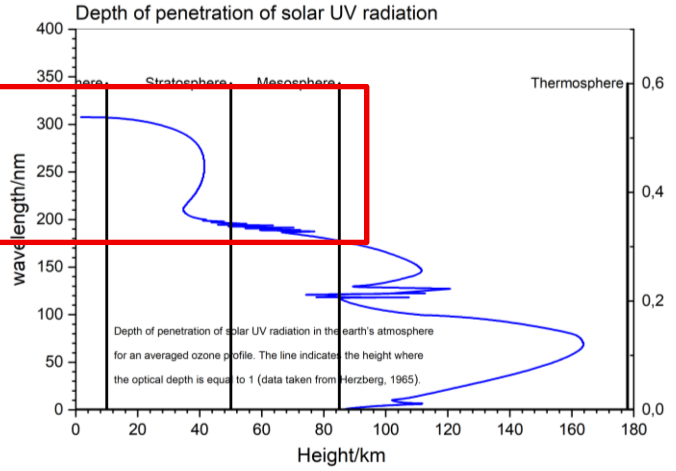

Figure 6.1: *Depth of penetration of solar UV radiation in the Earth's atmosphere for an average ozone profile. Blue line indicates the height where the OD is equal to 1, adapted from [1]. Red rectangular shows wavelengths accessible in stratosphere and up to mesopause.*

As one can see from the Figure 6.1, the solar (V)UV radiation in 160-310 nm spectral range penetrates efficiently in stratosphere-mesopause: short wavelength (V)UV radiation (< 200 nm) penetrates at high altitudes (mesosphere-thermosphere), while UV radiation (200 nm <) dominated in stratosphere.

An example of the far-UV-UV (162-230nm) absorption spectrum in the NO + NO2 + CO2 + CH4 + N2O + O2 + N2 mixture is shown in Figure 6.2 (left panel) and the same spectrum in UV-VIS (180-630 nm) spectral range is shown in Figure 6.2 (right panel).

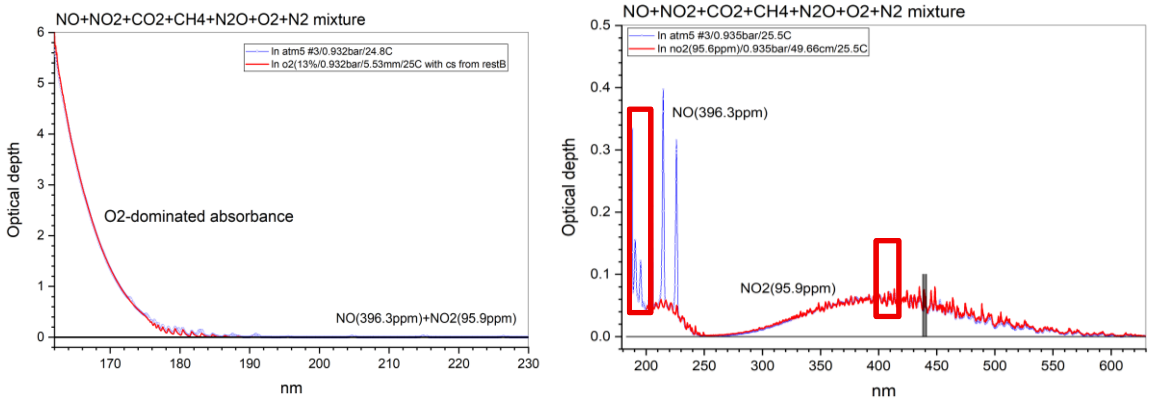

Figure 6.2: *Far-UV-UV (left) and UV-VIS (right) optical depths (absorptions) in synthetic anthropogenic gas mixture (blue). The spectrum below 180 nm is dominated by O2 absorption. NO (226nm) band and NO2 line at 439.5 nm are shown by red rectangles. Modelled O2 and NO2 absorption spectra are shown by red lines.*

The spectrum below 180 nm is dominated by oxygen absorption and has high OD values (left panel, red line fit). Far-UV light in 160-175 nm can efficiently penetrate in mesopause-thermosphere, Figure 6.1. In contrast, the spectrum above 200 nm consists of a broad NO2 absorption and very sharp NO absorption bands on the top of the NO2 continuum-like spectrum (right panel, red line fit) with low OD values. The NO2 absorption reaches about zero in 250-270 nm where atmospheric O3 has maximum in absorption.

As one can see from the Figure 6.2, the overall UV absorption by anthropogenic gases is dominated by NO and NO_2 (aerosol-free gas). NO2 line at 439.5 nm is commonly used for atmospheric NO_2 measurements. NO (226nm) band is frequently used for NO concentration measurements in industrial environments.

Change in NO and NO_2 optical depths in case of SPE's for US Standard Atmosphere

US standard atmosphere (1976) data have been used to model changes in the NO and NO2 OD in the case of SPE's. The results are shown in Figure 6.3.

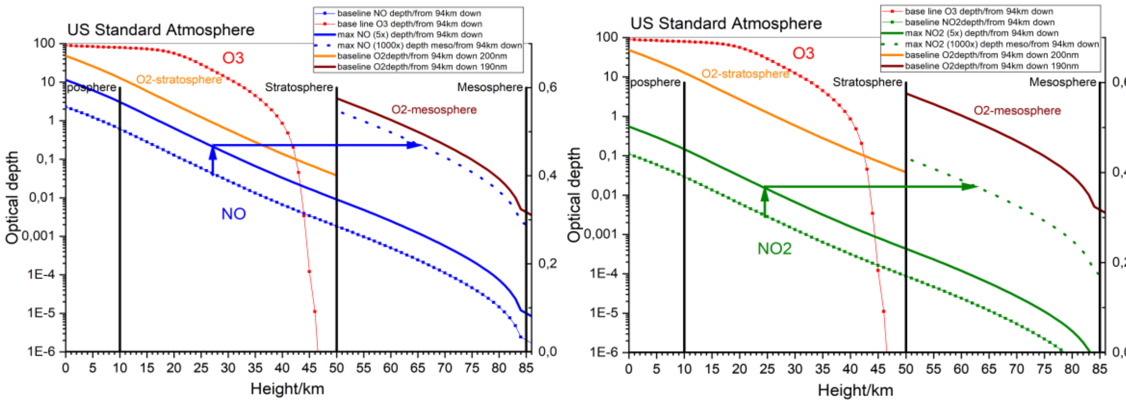

Figure 6.3: *Modelled NO (left, blue) and NO2 (right, olive) OD changes in the case of SPE's. NO/NO2 base lines are in points. Base lines for O3 (red), CO2 (orange) are given for reference. Vertical arrows show change in NO/NO2 OD in stratosphere at SPE's. OD values in mesosphere (blue and olive dot lines) will be similar to that in stratosphere (horizontal arrows).*

As one can see from the Figure 6.3 (left panel), typical NO OD variations at SPE's in stratosphere are between 0.01 and 1_(blue line). This will correspond to similar optical depths in mesosphere (horizontal blue arrow to dot blue line).

Typical NO2 OD variations in stratosphere at SPE's are from 0.001 to 0.1, Figure 6.3 (right panel, olive line) which is similar to optical depths in mesosphere (horizontal olive arrow to dot olive line)

Based on the modelling results in the Figure 6.3, the A and B mixture ratios have been chosen to cover the OD variations in NO and NO2 at SPE's.

Variations in NO and NO_2 optical depths with respective NO and NO_2 concentrations at SPE's conditions

Variations in OD for NO and NO2 are shown in Figure 6.4. OD for NO and NO2 are monotonically increasing with increase in NO and NO2 concentrations.

OD for NO was calculated as an integral over NO (226 nm) band. This allows one to eliminate influence of the spectral resolution of a spectrometer onto the OD data. OD for NO2 has been calculated at 439.5 nm. This is a maximum of the NO2 line between 438 nm and 441 nm. Because the low-resolution spectrometer (about 1 nm spectral resolution) used in the measurements, the NO2 (439.5 nm) line maximum is slightly affected by the spectrometer.

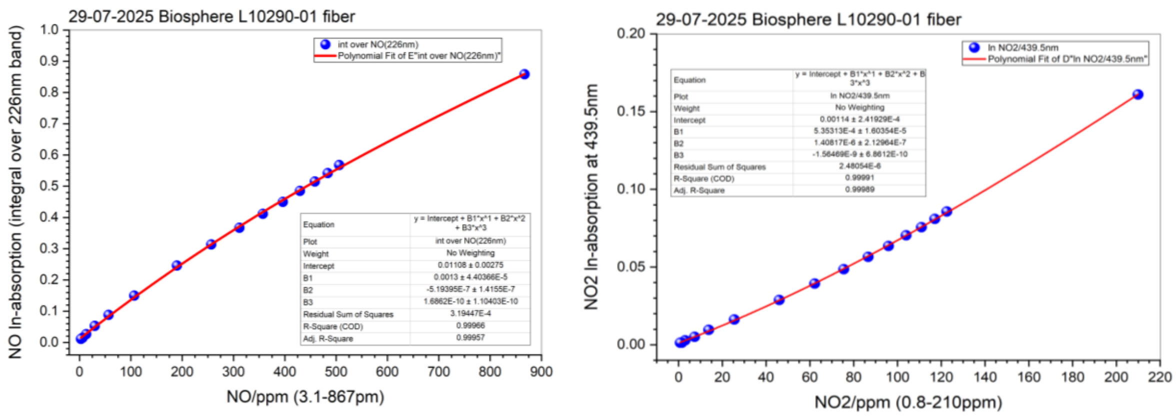

Figure 6.4: *OD for NO (as integral over NO (226nm) band), left and NO2 (439.5 nm), right (blue points). Polynomial (n=3) best fits in red lines.*

The best fit of NOx ODs' has been made by a polynomial function power three (n=3).

In general, the OD's for NO and NO2 are alike "linear"-type functions, if no accurate fit is required, Figure 6. 4. The SPE's have complicated physics and chemistry and may have non-linear effects onto NO and NO2 formation. The (V)UV-VIS light attenuation by NOx can be considered as a simple proportionality to their concentrations which will lead to decrease in (V)UV-VIS light penetration towards the Earth's surface, while the IR part of light will not be affected because very localized NOx absorption in IR. This decrease can be, to some degree, be beneficial if O3 layer variations in SPE's will happen at the same time.

7 Conclusions and Recommendations

The BIOSPHERE project successfully carried out four coordinated measurement campaigns (Athens, Brussels, Milešovka, and Lindenberg), collecting high-quality datasets on secondary cosmic rays, solar UV radiation, atmospheric parameters, and total ozone column. These campaigns represent the first multi-site effort to provide metrology grade data for assessing correlations between cosmic ray activity and solar UV radiation under varying environmental and atmospheric conditions.

Summary of key findings

- BIOSPHERE campaign observations confirmed a measurable link between cosmic ray activity and atmospheric ozone dynamics. Proton flux enhancements and geomagnetic disturbances were associated with ozone depletion in the mesosphere and lower thermosphere (around 75 km altitude), while the stratosphere remained largely unaffected.
- The influence of secondary cosmic rays on surface UV radiation appears negligible within the current measurement precision. This is primarily because natural variability in the total ozone column, typically ranging from 10–30 DU over weekly timescales, is much larger than any potential ozone modulation caused by solar or cosmic ray effects at mid-latitudes.
- The analysis confirms the dominant role of stratospheric ozone in controlling surface UV radiation levels. Clear anticorrelations between TOC and the UV Index were observed, especially under cloud-free conditions.
- Clouds together with the presence of desert dust and smoke aerosols play a crucial role in reducing UV-B levels by 30-62% at ground level.

- Laboratory experiments demonstrated that increased NO and NO_2 concentrations generated during solar particle events significantly enhance absorption in the (V)UV–VIS range, reducing the penetration of solar radiation through atmospheric gas columns.

Lessons Learned from the Measurement Campaigns

- Data continuity and redundancy are crucial: campaigns with uninterrupted SCR and UV records (e.g., Brussels) enabled the strongest analyses. Gaps in some datasets limited statistical significance.
- Meteorological variability (clouds, aerosols, albedo changes) had a stronger effect on UV than cosmic ray variations, underlining the need for integrated datasets for meaningful interpretation.
- SPE effects were more significant in high latitude sites than in the sites of the campaigns (middle Europe or even South of Europe in the case of campaign 1 - Athens).

Recommendations for Future Work

- Future studies should include longer-term monitoring campaigns (beyond seasonal scales) to better capture rare events such as strong SPEs and their atmospheric impacts.
- Expanding monitoring to higher latitude sites is recommended, as these regions are more directly impacted by energetic solar proton precipitation and may provide stronger signals in TOC–UV–SCR relationships.
- Strengthening the link between ground-based campaigns and satellite observations (e.g., EPT, OMI, TROPOMI) will improve the contextual understanding of local measurements within global-scale variability.

In conclusion, the BIOSPHERE project has successfully demonstrated the feasibility of a metrology-based framework for investigating the interactions between cosmic rays and solar UV radiation. The observations verified a detectable influence at higher altitudes in the mesosphere and lower thermosphere. Furthermore, the extensive datasets and methodologies created during this project offer a strong basis for long-term monitoring in the future. With important ramifications for climate research, environmental preservation, and public health, this framework will enable more accurate evaluations of atmospheric processes and their connections to cosmic and solar variability.

Acknowledgments

The project (21GRD02 BIOSPHERE) has received funding from the European Partnership on Metrology, co-financed by the European Union's Horizon Europe Research and Innovation Programme and by the Participating States. Funded by the European Union.

8 References

Alekseev, I. et al. (2022) 'Observation of the temperature and barometric effects on the cosmic muon flux by the DANSS detector', European Physical Journal C, 82(6), pp. 1–12. doi: 10.1140/epjc/s10052-022-10471-1.

Arunbabu, K. P. et al. (2017) 'Dependence of the muon intensity on the atmospheric temperature measured by the GRAPES-3 experiment', Astroparticle Physics, 94, pp. 22–28. doi: 10.1016/j.astropartphys.2017.07.002.

Asvestari, E., Usoskin, I. G., Kovaltsov, G. A., et al. (2017). Analysis of Ground Level Enhancements (GLEs) of Solar Energetic Particles: Updated Catalogue and Event Classification. *Solar Physics*, 292(10), 155. https://doi.org/10.1007/s11207-017-1186-0

Bernhard, G. H. et al. (2023) Stratospheric ozone, UV radiation, and climate interactions, Photochemical and Photobiological Sciences. Springer International Publishing. doi: 10.1007/s43630-023-00371-y.

BIOSPHERICAL Application Note #AN-2015-0001-Rev1: https://www.biospherical.com/wp-content/uploads/2024/03/guv_calibrations_006464ka_an2015-0001_rev1.pdf

Dobson, G. M. B. (1931) 'A photoelectric spectrophotometer for measuring the amount of atmospheric ozone', Proceedings of the Physical Society, 43(3), pp. 324–339. doi: 10.1088/0959-5309/43/3/308.

Dorman, L. I. (2004). Cosmic Rays in the Earth's Atmosphere and Underground. Springer.

GAW Report No. 284. (2020). Guidelines for the measurement of ozone and UV radiation. World Meteorological Organization, Geneva. WMO Global Atmosphere Watch Report No. 284. https://library.wmo.int/doc_num.php?explnum_id=10793

Georgieva, K. and Veretenenko, S. (2023) 'Solar influences on the Earth's atmosphere: solved and unsolved questions', Frontiers in Astronomy and Space Sciences, 10(December), pp. 1–23. doi: 10.3389/fspas.2023.1244402.

Georgoulias, A. K. et al. (2009) 'A study of the total atmospheric sulfur dioxide load using ground-based measurements and the satellite derived Sulfur Dioxide Index', Atmospheric Environment, 43(9), pp. 1693–1701. doi: 10.1016/j.atmosenv.2008.12.012.

Granja, C. et al. (2018) 'Directional detection of charged particles and cosmic rays with the miniaturized radiation camera MiniPIX Timepix', Nuclear Instruments and Methods in Physics Research, Section A: Accelerators, Spectrometers, Detectors and Associated Equipment, 911(September), pp. 142–152. doi: 10.1016/j.nima.2018.09.140.

Granja, C. et al. (2022) 'Spectral tracking of energetic charged particles in wide field-of-view with miniaturized telescope MiniPIX Timepix3 1 × 2 stack', Journal of Instrumentation, 17(3). doi: 10.1088/1748-0221/17/03/C03028.

Granja, C. et al. (2025) 'High-Resolution Mapping of Secondary Cosmic Rays With Miniaturised Stacked Pixel Telescope', Acta Polytechnica, 65(1), pp. 16–24. doi: 10.14311/AP.2025.65.0016.

Gray, L. J. et al. (2010) 'Solar influences on climate', Reviews of Geophysics, 48(4). doi: 10.1029/2009RG000282.

Grieder, P. K. F. (2010). Extensive Air Showers: High Energy Phenomena and Astrophysical Aspects –

A Tutorial, Reference Manual and Data Book. Springer.

Hülsen, G. and Gröbner, J. (2007) 'Characterization and calibration of ultraviolet broadband radiometers measuring erythemally weighted irradiance', Applied Optics, 46(23), pp. 5877–5886. doi: 10.1364/AO.46.005877.

Kalakoski, N. et al. (2023) 'Global ozone loss following extreme solar proton storms based on the July 2012 coronal mass ejection', Scientific Reports, 13(1), pp. 1–10. doi: 10.1038/s41598-023-40129-1.

Kerr, J. B. and McElroy, C. T. (1993) 'Evidence for large upward trends of ultraviolet-B radiation linked to ozone depletion', Science, 262(5136), pp. 1032–1034. doi: 10.1126/science.262.5136.1032.

Komhyr, W. D. (1980). Operations handbook – Ozone observations with a Dobson spectrophotometer. WMO Global Ozone Research and Monitoring Project Report No. 6.

Liou, K.-N. (2002) An introduction to atmospheric radiation. Elsevier.

Maurchev, E. A. et al. (2024) 'Comparison of Atmospheric Ionization for Solar Proton Events of the Last Three Solar Cycles', Atmosphere, 15(2). doi: 10.3390/atmos15020151.

Papaioannou, A. et al. (2016) ‘Solar flares, coronal mass ejections and solar energetic particle event characteristics’, Journal of Space Weather and Space Climate, 6. doi: 10.1051/swsc/2016035.

Pierrard, V. et al. (2025) ‘BIOSPHERE measurement campaign from January 2024 to March 2024 and in May 2024: Effects of the solar events on the radiation belts, UV radiation and ozone in the atmosphere’, AIMS Geosciences, 11(1), pp. 117–154. doi: 10.3934/geosci.2025007.

Pierrard V, Lopez Rosson G, Borremans K, et al. (2014) The Energetic Particle Telescope: First results. Space Sci Rev 184: 87–106. https://doi.org/10.1007/s11214-014-0097-8.

Savić, M. et al. (2021) ‘Modeling Meteorological Effects on Cosmic Ray Muons Utilizing Multivariate Analysis’, Space Weather, 19(8). doi: 10.1029/2020SW002712.

Sommer, M. (2022) Detection of Cosmic Radiation in the Atmosphere and Radiation Induced in Thunderclouds, PhD thesis. Technical University in Prague, Czech.

Steinbrecht, W., et al. (2025). The global Dobson and Brewer networks for ozone monitoring: history, current status, and future perspectives. Atmospheric Measurement Techniques. Copernicus Publications (in press).

Taricco, C. et al. (2022) ‘Exploration of the stratosphere with cosmic-ray muons detected underground’, Physical Review Research, 4(2), pp. 1–15. doi: 10.1103/PhysRevResearch.4.023226.

Tirado-Bueno, E., Mendoza-Torres, J. E. and de Mendonça, R. R. S. (2021) ‘Barometric coefficient dependence on the geomagnetic cutoff rigidity of neutron monitors’, Advances in Space Research, 68(6), pp. 2631–2642. doi: 10.1016/j.asr.2021.04.034.

Trottet, G. et al. (2015) ‘Statistical Evidence for Contributions of Flares and Coronal Mass Ejections to Major Solar Energetic Particle Events’, Solar Physics, 290(3), pp. 819–839. doi: 10.1007/s11207-014-0628-1.

Winant, A. et al. (2023) ‘The Atmospheric Influence on Cosmic-Ray-Induced Ionization and Absorbed Dose Rates’, Universe, 9(12), pp. 1–17. doi: 10.3390/universe9120502.

Winant, A., Pierrard, V. and Botek, E. (2025) ‘Ozone decrease observed in the upper atmosphere following the May 11th 2024 Mother’s day solar storm.’, (January), pp. 1–13. Available at: https://angeo.copernicus.org/preprints/angeo-2024-29/.

Wissmann, F., Dangendorf, V. and Schrewe, U. (2005) ‘Radiation exposure at ground level by secondary cosmic radiation’, Radiation Measurements, 39(1), pp. 95–104. doi: 10.1016/j.radmeas.2004.03.025.

Zuber, R., Gröbner, J., Egli, L., and Hülsen, G.: Uncertainty budget of total ozone column derived from spectral direct UV irradiance measurements, Atmos. Meas. Tech., 11, 2477–2497, 2018, https://doi.org/10.5194/amt-11-2477-2018